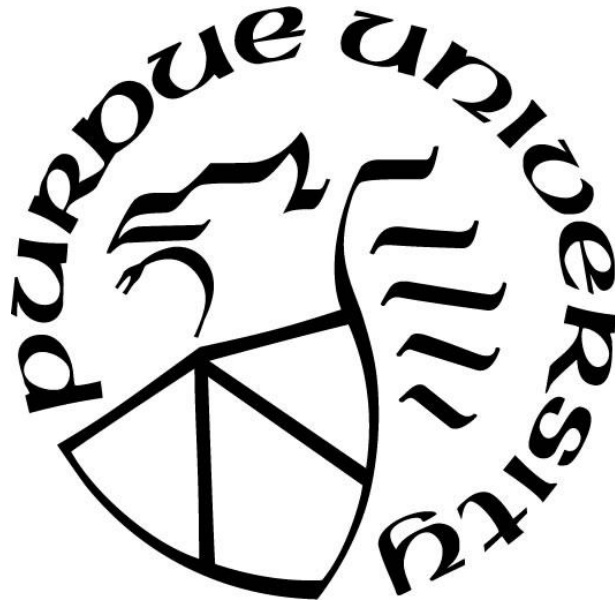# FINITE ELEMENT MODELING OF ELASTOHYDRODYNAMIC LUBRICATED ROLLING CONTACT FATIGUE

by

Neil R. Paulson

A Dissertation

Submitted to the Faculty of Purdue University

In Partial Fulfillment of the Requirements for the degree of

Doctor of Philosophy

School of Mechanical Engineering

West Lafayette, Indiana

May 2017

ProQuest Number: 10267283

ProQuest 10267283

www.manaraa.com

THE PURDUE UNIVERSITY GRADUATE SCHOOL
STATEMENT OF DISSERTATION APPROVAL

Dr. Farshid Sadeghi, Chair

    Department of Mechanical Engineering

Dr. Ganesh Subbarayan-Shashtri

    Department of Mechanical Engineering

Dr. Charles M. Krousgrill

    Department of Mechanical Engineering

Dr. Pablo D. Zavattieri

    Department of Materials Engineering

Approved by:

    Dr. Jay P. Gore

        Head of the Departmental Graduate Program

ACKNOWLEDGMENTS

TABLE OF CONTENTS

LIST OF TABLES

LIST OF FIGURES

ABSTRACT

Author: Paulson, Neil, R. Ph.D.
Institution: Purdue University
Degree Received: May 2017
Title: Finite Element Modeling of Elastohydrodynamic Lubricated Rolling Contact
   Fatigue
Major Professor: Farshid Sadeghi

Rolling contact fatigue (RCF) is a complex tribological problem due to its interdependence on multiple physical phenomena. Fluid mechanics, solid mechanics, damage mechanics are all relevant to the development of RCF failures. Due to computational requirements of modeling the multiple physical phenomena that govern RCF, typical RCF problems are simplified to only include a few physical phenomena. However, without addressing all the mechanisms at work in the system, the model is limited to particular applications and problems. Recognizing the multiple physical phenomena at play in rolling contacts, this preliminary dissertation presents several models which extend the current RCF models to include the interdependence of physical phenomena previously not considered in RCF research. The first model developed integrates a topological microstructural model with a damage mechanics model of fatigue crack growth. By including microstructural variation with the damage model, it is capable of predicting fatigue life variations in RCF. The coupled microstructure topology and damage mechanics model is based on previously developed RCF models; however, it was extended to study the effects of refurbishment on RCF failure. Using the RCF topology model, after a set number of initial fatigue cycles, refurbishing was simulated by removing a layer of surface material yet retaining the subsurface damage that accumulated from the original fatigue cycles. After refurbishment, simulated microstructures were subjected to additional fatigue cycles until failure occurred. It was observed that the increase of fatigue cycles prior to refurbishing decrease the refurbished life while increased refurbishing depth increases the life. Next, an extended microstructural model is presented which accounts for crystal anisotropy and orientation in the microstructure. The polycrystalline nature of steel components is known to create stress concentrations between crystals of incompatible orientation. The model developed

determines how crystal anisotropy and microstructure texture affect the initiation of RCF cracks. Next a model was developed which couples the elastohydrodynamic lubrication with a damage mechanics model for fatigue initiation and propagation. The model shows the interdependence of the EHL pressure profiles and fatigue damage. As fatigue damage occurs, the pressure profile is affected which in turn modifies the direction of future fatigue damage. While these two models have extended the current research in RCF, the next step was to integrate both models together in one combined model accounting for anisotropic material properties as well as elastohydrodynamic lubrication. Merging these two models allows the study of the effect of anisotropic properties on EHL contact pressure, film thicknesses as well as subsurface stresses. Results demonstrate that contact pressures are significantly affected by the anisotropic properties while film thickness profiles show minimal variation. The subsurface stresses show similar variation to those observed using the Hertzian pressure assumption with stress concentrations at the grain boundaries and significant scatter matching what is typically observed in experimental literature.

1. INTRODUCTION

Fatigue occurs when a component is subjected to repeated alternating loads over a period of time. The fatigue loads applied to the component are typically much lower than the static failure loads required to fail the component. The fatigued component may last for many thousands or millions of identical load cycles before failure occurs due to fatigue. While the component may seem to perform perfectly for the entire duration of the life prior to failure, the material within a fatigued component is actually damaged very slightly with each load cycle applied. The fatigue damage is typically concentrated at stress concentrations like scratches, cross sectional changes or sharp corners in the material. The microscopic fatigue damage in the material will eventually grow into a fatigue crack which will increase the stress concentration. Due the increased stresses from the stress concentration, the initiated fatigue crack will continue to propagate more rapidly. When the crack grows to a sufficient size, the material supporting the component reduces to the point the load can no longer be supported and a final rapid failure occurs.

1.1 Rolling Contact Fatigue

While this fatigue failure progression is typically used when describing classical fatigue failures, it shares many commonalities with the rolling contact fatigue discussed in this text. Rolling contact fatigue (RCF) is the predominant mode of failure when rolling components are properly installed, lubricated, and clean from contamination. RCF is typically categorized into surface and subsurface initiated spalling. Surface initiated spalling occurs when high friction, surface dents or other surface defects cause stress to rise to the surface of the material and lead to the formation of surface cracks. In subsurface initiated spalling (SIS), microcracks initiate and grow below the surface before eventually propagating to the surface and forming a spall. Subsurface initiated spalling is of particular interest because unlike other forms of surface damage which are caused by non-ideal operating conditions, SIS damage is predominant when bearings are operated under ideal conditions, i.e., well lubricated and free of surface defects.

1.1.1 Differences between Classical Fatigue and Rolling Contact Fatigue

While there are many similarities between classical fatigue and RCF, RCF does differentiate itself making it a difficult fatigue mode to study.

- As discussed previously, RCF is typically constrained to subsurface initiation. This is contrary to most classical fatigue which initiates on the surface of the component. Due to the subsurface initiation of RCF, it is particularly difficult to identify fatigue damage in the initiation phase and track fatigue crack propagation in situ which is possible in some classical fatigue test specimens.

- Stresses in RCF are highly localized due to the small width of the contact compared to the affected domain. In most classical fatigue testing a bulk stress is generated in the specimen which is nearly uniform across the cross section. Even within the small contact region of RCF, the non-conformal components do not have a uniform load profile but show high stresses near the center of the contact and lower stresses near the edges.

- Classical fatigue is commonly propagated in mode I crack growth (e.g. tensile fatigue). In RCF on the other hand, mode I crack growth is inhibited by the highly compressive hydrostatic stress generated below the contact. This leads to modes II and III driving the RCF fatigue cracks [1].

- The stress at a material point is non-proportional, meaning the stress components do not rise and fall in unison. In fact as a roller passes over a given material point in the domain, the shear stress τ_{xy} sees both a positive and negative shear while the normal stress components only see positive stresses. In a classical fatigue specimen the stresses typically increase together. This also affects the principal stress directions which are constant in a classical fatigue problem. In RCF the principal stresses change due to the changes in stress magnitudes throughout the loading pass. The changing principle stresses mean the critically stressed planes are changing throughout the loading pass.

1.2 Review of Rolling Contact Fatigue Life Theory

The beginning of the 20th century marks the beginning of published load capacity recommendations for rolling element bearings. Goodman [2] published a method to calculate the "safe loads" for ball and cylindrical rolling element bearings in 1912. Twelve years later Palmgren [3] extended the formulae proposed to include a prediction of the service life of bearings under different axial and radial loading conditions. The marked advantage of Palmgren's work was the identification of the stochastic nature of bearing fatigue failure data. Palmgren proposed the L_{10} factor for bearing lives which represents the point that 10% of the bearings are expected to fail for a given operating condition. While these early models form the basis of current RCF models, they lacked the generality required to apply to across all RCF problems. Since the models were mostly empirical, to determine the life of a different bearing size or type a new set of experimental tests were required.

Since the first bearing models were produced in the early 1900's, numerous mathematical models have been developed to study the fatigue lives of rolling element bearings. A recent review of the RCF [4] literature grouped the bearing fatigue models in three different categories:

- Engineering (empirical) models
- Research (analytical) models
- Computational models

Engineering models, also called probabilistic models, account for the statistical nature of rolling contact fatigue failures. By accounting for the life scatter in bearings these models are particularly useful to engineers in design applications concerned with component longevity and life cycle; however, these models rely upon calibration with full bearing fatigue test data and do not provide any insight to the physical mechanisms causing RCF in the component. Research models are focused exclusively on the physical mechanisms of RCF. These models can simulate the initiation and propagation of fatigue cracks under rolling contact but have a unique solution that does not explain nor account for the variation in RCF lives observed in reality. A newer modeling approach has emerged which attempts to bridge the gap between the two previous models by using a

physics based research model but also introducing the material microstructure and other inhomogeneities into the model. These computational models are capable of simulating crack initiation and propagation that is unique to a given material microstructure; therefore, by using the model to simulate numerous unique material microstructures, the population scatter of rolling component life can be captured. A brief history of the three different models is presented in the next three sections. A more complete treatment of the development of RCF life theory can be found in Sadeghi et al. [4].

1.2.1 Engineering Models

Due to the complications in studying rolling contact fatigue when compared to classical fatigue, the first RCF models were based on fitting results from experimental observations. The first stress based theoretical model for RCF was the seminal work by Lundberg and Palmgren [5] in 1947. In this work the fatigue crack was assumed to initiate at weak points in a critically stressed region of the material. The work proposed that the maximum orthogonal shear stress was the primary stress driving rolling contact fatigue. This was proposed because the orthogonal shear stress is one of the few stresses which has its maximum below the surface where subsurface spalling is typically originated. The theory only concerned itself with fatigue initiation, assuming propagation time was not a significant aspect to the fatigue life. It was postulated the weak points in the material were stochastically distributed therefore a smaller critically stressed region would increase fatigue life. To account for the statistical variation of RCF failure, the model introduced a Weibull statistics from experimental data to explicitly account for life variations. The Lundberg-Palmgren theory postulated the probability of survival, S, for a given bearing subjected to N stress cycles of fatigue loading follows the expression

$$\ln\left(\frac{1}{S}\right) = A\frac{N^e \tau_0^c V}{z_0^h} \tag{1.1}$$

Where τ_0 and z_0 are the maximum orthogonal shear stress magnitude and depth, respectively, e is the Weibull slope from the experimental results, and V is the volume of the critically stressed region. Variables A, c and h are material parameters which are all determined experimentally. Lundberg and Palmgren identified the critically stressed

volume, V, as the annular ring of material from the surface of the bearing to the maximum orthogonal shear stress depth

$$V = az_0(2\pi r_r) \tag{1.2}$$

where a is the width of the rolling element and r_r is the radius of the bearing ring. The proposed life equation was modified to a form more conducive to engineering design by Lundberg and Palmgren by substituting the bearing dimensions and Hertzian contact parameters into Equation (1.1):

$$L_{10} = \left(\frac{C}{P}\right)^p \tag{1.3}$$

Where C is the bearing dynamic load rating which is a purely a function of the bearing design, P is the equivalent bearing load which is a function of the load application. The exponent p depends on the contact geometry between the rolling elements and the raceway taking the value of 3 for point contact bearings, 4 for pure line contact bearings, and 10/3 for crowned rollers which operate between pure point and line contact. The advantage of the simplified equation is when used in application, the dynamic load rating can be obtained from a bearing manufacturers catalog and the equivalent bearing load can be simply calculated for a given application.

The proposed model became the basis of the first bearing life standards for industrial use (ISO 281) and is currently the basis of most life standards. Although the Lundberg-Palmgren model has been used extensively, the inability of the original model to account for surface roughness, lubrication conditions, residual stresses, surface friction among others has been identified and considered. The current ISO bearing standard [6] includes additional life modifying factors to account for the reliability, material, and operating conditions. These modifying factors are empirically developed constants which allow the extension of the Lundberg-Palmgren model to account for additional factors.

Ioannides and Harris [7] developed a model to address a few of the limitations and simplifications used in Lundberg-Palmgren theory. First the model accounts for the stress applied at each point within the material instead of assuming a single critically stressed region. The proposed model assumes the bearing is composed of discrete volumes at a given stress value. Each discrete volume has a given probability of survival

based on the volume, depth and stress applied. By multiplying all the survivabilities of the discrete volumes an overall survivability of the bearing can be calculated.

$$S_t = S_1 S_2 \ldots S_n \tag{1.4}$$

The model also proposed the idea of an infinite life for bearings similar to that proposed in classical fatigue problems. To achieve this infinite life level the proposed equation creates a threshold stress level which is required for failure to occur. If the stress at a given volume is below this threshold the probability of survival is equal to 1. Finally the model proposed a more general critical stress quantity which could represent the orthgonal shear stress, maximum shear stress or equivelent Von Mises stress. The resulting equation proposed by Ioannides and Harris is given by:

$$\ln\left(\frac{1}{S}\right) = AN^e \int_V \frac{(\sigma - \sigma_{th})^c}{z^h} dV \tag{1.5}$$

Where $z \ and \ \sigma$ are the depth and magnitude of the stress, and σ_{th} is the threshold stress below which failure does not occur. It is observed that Equation (1.5) simplifies to Equation (1.1) for a single stressed volume and a threshold stress equal to zero.

In a 2000 publication Zaretsky et al. [8] proposed a similar model to Lundberg-Palmgren theory. This method addressed two main modifications to the previous models. First the crack propagation was assumed to be insignificant to the bearing life; therefore the dependence on z_0 was eliminated. Secondly, it was observed that when rearranged to show life for a given probability of survivability Equation (1.1) is

$$N \propto \frac{z_0^{h/e}}{\tau_0^{c/e} V^{1/e}} \tag{1.6}$$

From this rearranged version an effective stress-life exponent can be defined as c/e; however, the dependence on fatigue life data, e, is not supported by literature so it was eliminated from the proposed equation [8]. This results in a probability of survivability of:

$$\ln\left(\frac{1}{S}\right) = N^e \tau^{ce} V \tag{1.7}$$

While these engineer models work well for applications of bearings to engineering problems, they do not provide any insights to the physical mechanisms causing RCF.

1.2.2 Research Models

Research models are based on physical principles and address the actual mechanisms involved in the failure process. These models typically focus on either fatigue crack initiation or fatigue crack propagation; although a few models have been proposed to study both initiation and propagation in RCF.

The crack propagation models are primarily based on fracture mechanics models. Keer and Bryant [9] developed the first of these fracture mechanics based models using Paris' law to study crack propagation. Here a surface crack in a rolling component was modeled as the crack rolled over the surface of a body. During the over rolling process the stress intensity factors were calculated at the crack tip and life was predicted by:

$$N = \frac{1}{2\beta_0} \int_{b_0}^{b} \frac{db}{(\Delta K)^m} \tag{1.8}$$

Here β_0 and m are constants, ΔK is the range of stress intensity factors over the stress cycle and b is the crack length. From this equation a stress-life equation was developed which follows the equation

$$N = \frac{1}{\beta_0} p_{max}^{-m} c^{1-\frac{m}{2}} \tag{1.9}$$

Where p_{max} is the maximum Hertzian pressure and c is the contact half-width. The proposed model predicts fatigue lives an order of magnitude shorter than experimental observations. This model has been extended to include additional effects including crack face friction due to crack closure, hydraulic fluid pressurization, and lubricant entrapment in the crack [10]. This recent extension has shown the effects of lubricate on rolling contact fatigue propagation lives.

Cheng et al. [11] studied the initiation lives through the use of Gibbs free energy associated with dislocation accumulation along slip bands based on the critical shear stress observed in the body. Vincent et al. [12] also proposed a model based on dislocation pileup theory; however, their model accounted for all stress components as well as residual stresses generated prior to the rolling pass. This model also accounted for spherical material defects which were the initiation locations for the fatigue crack.

While the above models account for either the initiation or propagation lives of RCF failure, Zhou et al [13] introduced a life model which accounted for both initiation and propagation lives. The initiation life prediction uses a similar form to the model proposed by Cheng et al [11] while the propagation life is based on fracture mechanics similar to Equation (1.8). Similarly Lormand et al. [14] extended the initiation model proposed by Vincent et al. [12] to include propagation life according to Paris law. While the research models have performed admirably in the development of physical understanding of how RCF initiates and propagates, none of the models proposed explicitly account for the variations observed in experimental results and therefore the models are unable to predict the life variations observed in RCF failures.

1.2.3 **Computational Models**

Computational models have recently been proposed which offer an attractive combination of the benefits of probabilistic experimental models and physically based research models. In computational models a physics based approach to fatigue modeling is used; however, it is coupled with a model of the subsurface material microstructure. In this way the subsurface topology and material heterogeneities modeled form sources of variability in the fatigue lives. Therefore, a purely analytical model can be used to predict the fatigue life as well as statistical variation of a bearing population.

The first proposed computation model introduced by Raje et al [15] predicted the dispersion of fatigue lives. The model used randomly generated discrete material microstructure. To generate the microstructure, discrete rigid Voronoi elements were joined by visco-elastic interfaces. The shear stresses experienced on these elastic interfaces as Hertzian load profile was passed over the domain were considered the driving force behind the fatigue process. Using the largest magnitude of shear stress and the corresponding depth an expression for the proportional initiation life was:

$$N \propto \frac{z^r}{\tau^q} \tag{1.10}$$

The differences in simulated microstructure resulted in variations in the predicted life for each simulation. By combining 33 different simulated microstructures the scatter of the fatigue lives was predicted.

To extend the above model to include both crack initiation as well as propagation, Raje et al. [16] enhanced the previous microstructure model to include damage mechanics theory. In damage mechanics an internal damage variable, D, is introduced to account for the accumulated damage due to repeated loading cycles. The damage evolution law implemented by the model is based on an isotropic damage variable for high-cycle fatigue:

$$\frac{dD}{dN} = \left[\frac{\Delta\tau}{\tau_r(1-D)}\right]^m \tag{1.11}$$

Where $\Delta\tau$ is the range of the shear stress, and τ_r and m are material parameters. The results of the proposed model showed good agreement with the experimental model proposed by Lundberg and Palmgren.

Latter work in this field by Jalalahmadi and Sadeghi [17] modified the model to use elastic deformable material grains and apply the damage directly to the grain with no visco-elastic interfaces. This elastic model was then used to study the effect of material inclusions [18] in the microstructure. Using material inclusions, the model could more closely predict experimental bearing results. Later developments of this model approach have included the addition of plastic deformation in the simulated contact region [19], [20] and extension of the model to account for 3D microstructures [21].

1.3 Limitations of Current Models

While the computational models described above have shown significant promise in bridging the gaps between experimental models which account for the stochastic nature of RCF and research models which explicitly account for the physics of RCF, there are still several inconsistencies with the actual fatigue mechanism. First, the model of material microstructures is simplistic. The proposed models only account for the microstructure topology. However, the microstructure variations are much complicated than the topology. Each material grain is actual a crystal which has an anisotropic deformation definition. Therefore the material will deform differently based on the direction of applied load. The crystal anisotropy also introduces a material texture to the microstructure properties which defines how the individual crystals are oriented in the

domain, be it random or following some other structure. Each of these microstructural variations will create additional variation in the material and therefore in the fatigue life.

Another limitation of the currently proposed model is the application of a Hertzian pressure distribution. From the original model proposed by Lundberg and Palmgren [5] it has been generally assumed that a Hertzian pressure profiles is an accurate model of the contact pressures in rolling contact fatigue. However, nearly all components that exhibit RCF are actually lubricated contacts; therefore, an elastohydrodynamic lubrication (EHL) model will generate a more accurate pressure profile. The EHL contact pressure will also be affected by the speed of the contact which is not accounted for in the proposed computational models. The contact pressure is also affected by the subsurface damage present as damage accumulates. The effect of this subsurface damage on pressure has not been fully studied using the computational models proposed. Damage effect on contact pressure was studied briefly by Bomidi and Sadeghi [20]; however, it has not been considered how this degradation will affect a lubricated contact like those observed in RCF.

1.4 Scope of the Dissertation

Identifying the current limitations of the computational models, this work is focused on extending the current model to include additional randomness associated with the microstructural model and define a more accurate contact stress in the RCF model to account for lubrication effects. Chapter 2 describes the development of the damage mechanics model described by Jalalamhadi et al. [18]. It describes in detail the topology model for microstructures, damage mechanics formulation as well as finite element model used to determine the stresses in the component. In addition to developing the previously proposed model, a unique application is described whereby bearings are refurbished after moderate use. During the refurbishing process a small amount of material is removed from the surface of the bearing and then the bearing is put back in service. Based on the number of variables associated with the refurbishing process (e.g. cycles before refurbishing and depth of refurbishing) it is infeasible to determine the remaining life through experimental methods. Therefore, this is an excellent application

of the computation model to determine the life of a refurbished bearing population. In chapter 3, the microstructural model is extended to account for crystal anisotropy and random material texture. This requires redefining the material stiffness matrix with anisotropic properties and orienting each material grain with a unique crystallographic orientation. Since crystal anisotropy is known to create stress concentrations where fatigue cracks initiate, this model was only focused on identifying initiation life. In chapter 4, a new fully coupled FEA model was developed which allows the simultaneous calculation of elastohydrodynamic pressure and subsurface stress fields. By implementing this method, the effect of lubricated contacts can be compared to the Hertzian pressure assumption. This method also allows the continual update of EHL pressure profiles due to damage accumulation in the component. Chapter 5 extends the previously described models to combine the crystal anisotropic material model of chapter 2 with the fully coupled EHL model developed in chapter 4. The development of a crystal anisotropic material model to determine EHL pressure profiles will be the focus of the future work for this thesis. Using this combined model, it is possible to understand what the effects of anisotropic material properties are on lubricated contact pressure, film thicknesses and internal stress profiles. The final chapter 6 gives a summary of the work done in this thesis and states some of the possibilities for future model development and validation.

2. ROLLING CONTACT FATIGUE OF REFURBISHED BEARINGS

2.1 Introduction

In the 1950s Palmgren [22] observed that most bearing failures are due to the damage of a single bearing component, and by replacing this component, the life of the overall bearing assembly could be significantly extended. A recommended procedure for bearing repair was created and published by NASA in the mid-1970s [23]. Since that time, bearing repair has become a common practice in commercial and military aircraft applications. However, aerospace applications are not the only industry that can benefit from bearing refurbishing. Bearing repair procedures have been implemented in off-highway and construction equipment [24] as well as industrial processing industries [25]. Bearing repair has shown significant cost savings over bearing replacement, with typical repaired bearings saving between 60% and 80% of the cost of new bearings [22], [24], [25]. Not only is the cost of repaired bearings lower, but for custom bearings, the lead times can be significantly reduced, decreasing downtime on critical machinery.

Bearing repairs are generally divided into four different categories based on the extent of the damage to be repaired. The most basic form of bearing repair as defined in the latest NASA specification [26] is a Level I repair. In this most basic form of repair, the bearings are cleaned and inspected for damage, running surfaces are buffed or polished, and the bearings are then reassembled, packaged and sent for installation. In the Level II repair, all of the Level I repairs are made with the addition of replacement of rolling elements, grinding of the mounting surfaces to return to original drawing dimensions, and honing (superfinishing) of raceways to remove superficial damage. When bearing inspection shows significant surface damage, a Level III repair is required. For this repair the surface damage is removed by grinding up to 0.015 in (~380 μm) off the inner and/or outer race [27]. The bearing is then reassembled with larger sized rollers to compensate for the removed material. When surface damage extends deeper than 0.015 in, a Level IV repair is required. In this case the damaged bearing component is replaced and reassembled with the original undamaged bearing components.

Of the four different repair levels, Level III repair shows the most promise in significantly extending the lives of rolling element bearings because it enables repair of surface damaged bearings with minimal cost. Surface damage – caused by dents, lubricant contamination and overloading, among other non-optimal operating conditions – accounts for more than 90% of bearing failures observed in industry [28]. However, subsurface-initiated rolling contact fatigue is considered the ultimate failure mode of rolling element bearings operated under ideal conditions. Unlike surface damage, subsurface spalling generally cannot be repaired with a Level III repair as the damage penetrates below the maximum allowable grinding depth. The advantage of a Level III repair, therefore, is that it can repair problems arising from non-optimal operating conditions, allowing bearings to last to the ultimate failure mode.

One of the leading problems in the widespread implementation of bearing restoration is the lack of information available on the life of bearings after grinding and rebuilding. Much less research and testing has been conducted on the life of restored bearings than the life of original bearings. The testing that has been done is limited to specific industries and applications [29]. Coy et al. [23] proposed an analytical model of bearing restoration using an extension of the Lundberg-Palmgren bearing life equation [5]. This method was further extended by Zaretsky [30] to use the maximum shear stress criteria [8] and include the inner race and rolling element fatigue failures in addition to the outer race fatigue. Kotzalas and Eckels [29] created an analytical refurbishment model using the ISO 281:2007 standard. The significant advancement of this model was to consider the entire stress field instead of the simplified fields of the Lundberg-Palmgren and Zaretsky bearing life equations.

One limitation of all the previously proposed models is that each assumes a constant Weibull distribution of the bearing failures. This creates two limitations: First, a group of bearings must be tested in order to determine the Weibull parameters applicable for the model. Second, the models assume the Weibull parameters of the refurbished bearings are based on the Weibull parameters of the original bearings. Raje et al. [15] has proposed a new model for rolling element bearing fatigue that eliminates the limitation of testing a group of bearings to determine a Weibull parameter. Instead of using set

Weibull parameters, the new model uses a microstructure topology model coupled with damage mechanics to determine analytically the life distribution of a bearing population. This model has since been extended to include the effects of plasticity [19], [20] and three-dimensional topology [20], [21], [31]. All of the proposed models have shown good agreement with experimental rolling contact fatigue data.

In the current investigation, the finite element continuum damage mechanics model is used to numerically simulate the life of restored bearings. In order to determine the remaining life of restored bearings, 33 topological domains are run to 50% and 90% of the population L_{10} life. The bearing grinding was simulated by cutting the top layer of the microstructural domain at depths of 0.125, 0.25, 0.5 and 0.75 times the half contact width. The incipient damage occurring in the microstructure before the restoration was retained to account for the initial load passes on the bearing. From these results a new approach is proposed that models the population L_{10} life of a resurfaced bearing.

2.2   Modeling Approach

2.2.1   Modeling of Material Microstructure

The steel material microstructure is modeled using a Voronoi tessellation process. In order to generate a Voronoi domain, a random set of nucleation points are placed in the desired area. Regions are constructed around the nucleation points such that all points in a given region are closer to the nucleation point for that region than to any other nucleation point. These regions are known as Voronoi polygons. This domain generation procedure can create unique, random domains for a simulation. Grain size is controlled by specifying the minimum and maximum distances between nucleation points. Grain diameter within the domains used in this study is approximately 10 µm, which is typical for bearing steels [32]. The number of sides and the orientations of the Voronoi polygons are variable, although the most probable number of sides is six [33]. This matches the number of sides suitable for maximum thermodynamic stability in actual steel grains. After the domains are generated, they are meshed with constant strain elements. Each Voronoi polygon is meshed with *n* triangles, where *n* is the number of sides in the polygon.

Figure 2.1 illustrates the original size of the microstructure domain. The size of the representative volume element (RVE), modeled with a Voronoi microstructure is -2.2b to 2.2b in width and 0b to 1.7b in depth, where b is the Hertzian half contact width. Previous research has used RVE depths of 0b to 1.55b; however, the RVE size of the original microstructure was extended for this model to provide a sufficient microstructural depth after refurbishing of the bearing. Outside the RVE region the finite element model is filled with regular triangular elements to extend the modeled domain to -5b to 5b in width and 0 to 7b in depth. The outer region of the domain is required to satisfy the semi-infinite domain assumption of the Hertzian contact. The damage within the RVE microstructure is modeled using continuum damage mechanics.

2.2.2 **Simulation of a Rolling Contact Cycle**

Figure 1 illustrates an FE plane strain semi-infinite domain subject to a Hertzian pressure. In order to simulate the rolling contact phenomenon, a line contact Hertzian pressure profile is moved across the top surface of the semi-infinite domain. Previous research [16], [20] has shown that moving the pressure profile from -2b to 2b in 21 discrete steps provides a sufficient resolution to model a rolling contact. For a line contact, the Hertzian half-width of the contact is given by:

$$b = \left(\frac{8w}{\pi l E' \left(\frac{1}{R_1} + \frac{1}{R_2} \right)} \right)^{0.5} \tag{2.1}$$

where l is the length of the contact, R_1 and R_2 are the radii of curvature of the bodies in contact, and E′ is the equivalent modulus of elasticity.

$$\frac{1}{E'} = \frac{1}{2} \left(\frac{1 - \nu_1^2}{E_1} + \frac{1 - \nu_2^2}{E_2} \right) \tag{2.2}$$

The Hertzian pressure is given by:

$$P = P_{max} \left(1 - \frac{x^2}{b^2} \right)^{0.5} \tag{2.3}$$

where

$$P_{max} = \frac{2w}{\pi b l} \tag{2.4}$$

Here, w is the load applied.

2.2.3 Fatigue Damage Modeling

In the current investigation, continuum damage mechanics is used to model crack initiation and growth due to material degradation during repeated loading [34]–[36]. Material damage depends largely on the heterogeneous nature of polycrystalline materials [37]. Using damage mechanics, crack initiation, propagation and final failure of a polycrystalline material can be investigated. In continuum damage mechanics, a damage variable, D, is introduced into the constitutive equations to represent the current state of damage in the material. Each finite element in the computational domain has an associated value of D that corresponds to the damage state in that given element. In the most general case, D is a tensor quantity; however, for this analysis isotropic damage was assumed [16], [33] simplifying D to a scalar value. Assuming plane strain conditions and neglecting the crack closure effect, an isotropic damage coupled elasticity law is given by Lemaitre [34] as:

$$\sigma_{\alpha\beta} = \frac{E(1-D)}{1+\nu}\left\{\epsilon_{\alpha\beta} + \frac{\nu}{1-2\nu}\epsilon_{yy}\delta_{\alpha\beta}\right\}, \alpha = 1,2, \beta = 1,2 \qquad (2.5)$$

where $\delta_{\alpha\beta}$ is the Kronecker delta function. The damage variable, D, can take values between 0 and 1, where 0 corresponds to an undamaged material and 1 corresponds to a completely damaged material. Constitutive equations governing the evolution of damage have been formulated to satisfy the thermodynamic laws pertaining to fatigue, ductile and creep damage [34]. A commonly used equation for the evolution of D in high cycle fatigue is given by:

$$\frac{dD}{dN} = \left[\frac{\Delta\sigma}{\sigma_r(\sigma_m)*(1-D)}\right]^m \qquad (2.6)$$

where N is the cycle number, $\Delta\sigma$ is the range of the stress that causes damage, σm is the mean stress, and σr and m are material dependent parameters that must be experimentally identified. The term σr(σm) is a material parameter that is often called the resistance stress [38] because it controls material's ability to resist damage accumulation and can be a function of the mean stress.

Several stress components, including the maximum shear stress, maximum orthogonal shear stress and Von Mises stress have been used in life models for rolling contact fatigue. These stress components are deterministic, and when used in an analysis, would result in

the same life and damage evolution characteristics for any given simulation. The model presented in this paper and discussed herein uses the orthogonal shear stress component resolved along the material microstructure grain boundary to account for the variability and randomness in the simulation [12,14,23,24]. Furthermore, observations have shown that the mean shear stress does not play a significant role in shear-driven fatigue. Thus, the damage evolution equation can be reduced to:

$$\frac{dD}{dN} = \left[\frac{\Delta\tau}{\tau_r(1-D)} \right]^m \tag{2.7}$$

where $\Delta\tau$ is the range of shear stress acting on a particular grain boundary. τ_r is the resistance stress and is analogous to the value σ_r described previously; it represents the material's ability to resist damage accumulation.

2.2.4 Numerical Modeling of the Damage Equations

In order to carry out the fatigue simulation, Equation (2.7) is applied to each finite element within the material microstructure domain. This results in a system of coupled first order differential equations, which requires knowledge of the stress range $\Delta\tau$ on each grain boundary as a function of the fatigue cycle, N. High cycle fatigue involves millions of cycles, but performing a fully coupled analysis at each cycle would be computationally impractical and time-consuming. Therefore, the "jump-in-cycles" approach outlined by Lemaitre [34] is employed to streamline the analysis.

The "jump-in-cycles" method assumes that the stress field is unchanged over a finite number of cycles, ΔN^i, where i indicates the cycle block. The damage variable D_j^i represents the damage state at a single element, where j ranges over the number of elements and i indicates the cycle block. The relation between stress amplitude and the damage evolution rate is given by:

$$\left(\frac{dD}{dN} \right)_j^i = \left[\frac{(\Delta\tau)_j^i}{\tau_r(1-D_j^i)} \right]^m \tag{2.8}$$

Because the stress field remains unchanged over a block of cycles, the change in damage, ΔD, is constant. The number of cycles in the current block of cycles, ΔN^i, must be defined. This can be written as:

$$\Delta N^i = \frac{\Delta D}{(dD/dN)^i_{crit}} \tag{2.9}$$

where

$$\left(\frac{dD}{dN}\right)^i_{crit} = Max \left| \left(\frac{dD}{dN}\right)^i_j \right| \tag{2.10}$$

is the maximum damage rate that results from calculating the rates for all elements. The number of cycles up to this point in the simulation is defined as:

$$N^{i+1} = N^i + \Delta N^i \tag{2.11}$$

and the damage at each element is calculated as:

$$D_j^{i+1} = D_j^i + \left(\frac{dD}{dN}\right)^i_j \Delta N^i \tag{2.12}$$

After the damage at each element is determined, the elastic modulus is found using:

$$E_j^i = E_0(1 - D) \tag{2.13}$$

After the new elastic modulus for each finite element is calculated, the above procedure is repeated. Selecting a reasonable value for *ΔD* requires consideration of computational time and maintaining the coupling between damage and stress. Figure 2.3 shows the piecewise linear evolution of damage that is produced as the above procedure is repeated.

2.2.5 Identification of Material Fatigue Parameters

The damage model described in Section 2.2.3 introduces two material parameters, namely τ_r and m, which are determined experimentally. Since τ_r and m are material parameters and not specific to rolling contact fatigue, alternative methods of loading can be used to determine the parameters. Previous research [32] has demonstrated that the damage resulting from torsional fatigue is similar to the shear-driven damage accumulation mechanism observed in rolling contact. Therefore, the fatigue damage parameters derived from the stress-life relationship for a material in torsional fatigue can be applied to materials in rolling contact fatigue.

For torsional fatigue testing, the equation of the stress-life curve is given by Basquin's law:

$$\frac{\Delta \tau}{2} = \tau_f (N_f)^{\frac{1}{B}} \rightarrow N_f = \left[\frac{2\tau_f}{\Delta \tau}\right]^B \tag{2.14}$$

where N_f represents the number of cycles at which failure occurs when subjected to a stress $\Delta\tau$. Both τ_f and B are material parameters determined by fitting experimental data. To determine the material parameters for this investigation, torsional bars of 8620 were tested using an MTS torsion fatigue test rig as described by Bomidi et al. [32]. Figure 2.2 depicts the torsion fatigue results for 8620 bearing steel. A power law fit is applied to the data to obtain the Basquin fitting parameters:

$$B = 13.16$$
$$\tau_f = 2.362 \tag{2.15}$$

The material parameters from the torsion fatigue results can be equated to the damage mechanics parameters by first integrating Equation (2.7) under the assumption of a constant stress range, resulting in:

$$\int_0^{N_f} dN = \int_0^1 \left\{ \frac{\tau_r(1-D)}{\Delta\tau} \right\}^m dD \rightarrow N_f = \frac{1}{m+1}\left[\frac{\tau_r}{\Delta\tau} \right]^m \tag{2.16}$$

Equating Equations (2.14) and (2.16) results in:

$$\frac{1}{m+1}\left[\frac{\tau_r}{\Delta\tau} \right]^m = \left[\frac{2\tau_f}{\Delta\tau} \right]^B \tag{2.17}$$

Solving Equation (2.17) for the damage model material parameters τ_r and m determines explicit equations for the relationship between the Basquin material parameters and damage model parameters given by:

$$m = B$$
$$\tau_r = 2\tau_f(B+1)^{\frac{1}{B}} \tag{2.18}$$

Using these relationships, the material parameters for the damage model were determined as:

$$m = 13.16$$
$$\tau_r = 5{,}778 \; MPa \tag{2.19}$$

2.2.6 Simulation of Refurbishing Operation

In order to simulate the refurbishing (resurfacing) of bearings, two different steps are taken. The first step is to find the damage associated with each element in the domain when the bearing is refurbished. To determine this quantity, 33 microstructural domains are generated and subjected to repeated cycling until a crack reaches the surface (complete failure). Figure 2.3 (dashed line) illustrates how the damage in an element is

interpolated from the damage evolution curve at a given refurbishing cycle. The jump-in-cycles method described in Section 2.2.4 produced a piecewise linear curve; therefore, any refurbishing cycle number can be predicted between 0 and the cycle of complete damage (N_{crit}). If the refurbishing cycle occurs after N_{crit} the damage variable is equal to 1, since damage cannot exceed 1. The damage values for each element are calculated and used to initialize the damage variable when the refurbished bearing fatigue simulation resumes.

Once the damage state for each element is determined, material is removed from the microstructural domain to simulate refurbishment. In order to simulate refurbishment, a line is passed through the domain at the desired depth. All of the Voronoi cells above the cutline are removed from the domain simulating grinding material from the bearing raceway. For partial Voronoi cells, nodes are created at the intersection of the Voronoi boundaries and the cutline. These new nodes form the upper boundary of the Voronoi cell as shown in Figure 2.4. With the simulated microstructure cut to the desired depth, the centroids of each Voronoi are determined using the newly defined Voronoi cell geometry. The modified Voronoi cells are then divided into triangles as described in Section 2.2.1. The accumulated damage from the original loading is retained in each element of the domain to account for the previous fatigue damage. Because material has been removed on the surface of the domain, an equal amount of material is added to the bottom of the domain to keep the domain size constant. Constant strain elements were added to the base of the domain to return the resurfaced domain to the original model size.

2.3   Results and Discussion

As described in Section 2.2.1, a Hertzian pressure field was passed over the top surface of every domain. Initiation life was defined as the cycle number in which a single element became fully damaged, causing the first crack to appear. Final life was defined as the cycle number in which a crack reached the top surface of the microstructure. Of the 33 domains generated, two experienced premature failure in which a crack initiated at the surface of the domain. These domains with surface initiated cracks were removed from the results as they do not represent subsurface rolling contact fatigue. The remaining

domains experienced subsurface crack initiation, after which cracks propagated to the surface. After the final life was determined for every domain, the L_{10} life for the population was calculated using a two-parameter Weibull distribution. The Weibull slope of the data is 7.72 and Weibull strength is 6.5. Because the current model assumes isotropic uniform material properties and ignores inclusions and other random defects in the microstructure, Weibull slopes for these domains are larger than those found experimentally. Raje et al. [15] and Jalalmadi et al. [18] showed that adding randomly placed inclusions and defects decreases the Weibull slopes of the model.

In order to investigate the effects of running time prior to refurbishing, microstructural domains were cut at 50% and 90% of the L_{10} life cycles. Damage values for each element were calculated and applied as described in Section 2.2.7. Four grinding depths (0.125, 0.25, 0.5 and 0.75b) were used at each refurbishing time to study the effects of removing various amounts of material. Once refurbishing was simulated, fatigue cycling of the domain continued until a crack reached the surface, indicating a spall formation. The lives of the refurbished bearings reported below were determined by the number of simulated cycles occurring between refurbishing and a fatigue crack reaching the surface. The simulated cycles prior to the refurbishing were not included in the calculation of refurbishing life.

Figure 2.5**:** shows the refurbished lives were lowest when 0.125b was removed from the surface. This result is best explained by studying the critical stress depth in both the pristine domain and the refurbished domain. The maximum shear stress reversal is the critical stress in these simulations, and it occurs at approximately 0.5b below the surface. Therefore, material near this depth becomes critically damaged first.

Removing 0.125b moves the previously damaged elements closer to the new surface. Examining the damage pattern from Figure 2.6A illustrates an interesting phenomenon. Most of the critical damage lies near the location of the maximum shear stress reversal in the pristine domain, not 0.5b below the refurbished surface. This indicates that the original damage created a weak region in the domain and altered the depth of crack initiation.

The damage pattern observed after removing $0.125b$ did not carry over to domains experiencing greater material removal. When $0.25b$ was removed, the initial damage was moved farther from the expected critical depth of stress in the refurbished domain, and cracks initiated near $0.5b$ below the new surface. However, much of the initial damage remained in the domains, leading to a lower L_{10} life when compared with the pristine case. Figure 2.6B depicts the damage at failure in a domain with $0.25b$ removed.

Removing $0.5b$ brought the formerly damaged material close to the surface, or in some cases, removed it altogether. This explains the increase in L_{10} life compared to the previous two refurbishing cases. Domains experiencing a removal depth of $0.75b$ were essentially restored to pristine condition, as shown by the resulting refurbished life distribution. Figure 2.6C and D, respectively, illustrate the damage in domains experiencing $0.5b$ and $0.75b$ refurbishment.

Table 2.1 contains the Weibull slope and L_{10} life for the domains in each of the four cutting depth scenarios. The table shows that Weibull slopes below the critical depth of $0.5b$ are lower than the pristine Weibull slopes, while removing more than the critical depth does not significantly change the Weibull slope. Therefore, for lightly refurbished bearings, there will be more scatter observed in the population, and heavily refurbished bearings will have nearly the same scatter as observed in the original bearing population. The results also show that refurbishing at 50% of the L_{10} life provides significant refurbishing lives with all lives greater than 50% of the original L_{10} life. The deeper refurbishing depths produce longer refurbishing lives; the refurbished life of a $0.75b$ refurbished bearing population is nearly twice the life of a $0.125b$ refurbished population.

Life distributions resulting from refurbishing at 90% of the pristine L_{10} life showed similar patterns to those already presented. Four different material removal depths were again studied, with L_{10} life increasing with greater removal. Figure 2.8 shows the damage in the failed, refurbished domains, and illustrates the Weibull slopes and L_{10} lives for the 90% L_{10} refurbishing populations. For this refurbishing time, it is clear that the depth of refurbishing is very important to the remaining refurbishing life as the bearings refurbished to $0.75b$ have nearly 8 times the L_{10} life of those bearings only refurbished to

0.125b. Comparing refurbishing at 50% vs. 90% of the L_{10} life displays that for light grinding depths, the refurbishing time makes a significant difference. However, bearing life does not increase significantly when grinding depth increases beyond 0.5b. Using this data, the ideal refurbishing approach would be to refurbish as late as possible with a grinding depth of at least 0.5b.

Coy et al. [23] extended the bearing model proposed by Lundberg and Palmgren to study the remaining life in rolling element bearings. They proposed an equation that can be used to calculate the bearing life distribution for a given refurbishing time and depth.

$$\ln(S_r) = \left(ln\left(\frac{1}{0.9}\right) \\ * \left((x-1) * \left(\left(\frac{\eta_{orig} + \eta_{refurb}}{L_{10,orig}}\right)^e - \left(\frac{\eta_{orig}}{L_{10,orig}}\right)^e \right) - x \\ * \left(\frac{\eta_{refirb}}{L_{10,orig}}\right)^e \right) \right) \tag{2.20}$$

Where S_r is the probability of survivability, x is the refurbishing depth, e is the Weibull slope, $L_{10,orig}$ is the original L_{10} life, and η_{orig} and η_{refirb} are the original and refurbished cycles, respectively. To compare the extended Lundberg-Palmgren approach to the damage mechanics approach developed for this investigation, Equation (2.20) was used to generate Weibull plots for each of the resurfacing conditions applied in the current study. The bearing Weibull slope, was assumed to be equal to 7.72, the Weibull slope found for pristine domains in the numerical model. Figure 2.9 and Figure 2.10 illustrate the extended Lundberg-Palmgren approach Weibull results combined with the damage mechanics results for the 50% and 90% L_{10} resurfacing times, respectively. The Lundberg-Palmgren modeling approach matches the trends of the damage mechanics model developed for this investigation for resurfacing depths of 0.125b and 0.25b. However, the more complete accounting of the stress fields by the damage mechanics model results in more conservative life estimates. It should also be noted that the Lundberg-Palmgren model results vary from a standard 2-parameter Weibull distribution with more scatter occurring in the early failures. This behavior is also observed in the

results of the proposed damage mechanics method, indicating refurbished bearings may not follow a standard 2-parameter Weibull distribution. For refurbishing depths of $0.5b$ and greater, the Lundberg-Palmgren approach gives the same results regardless of the resurfacing depth, which is not consistent with the currently proposed model that shows higher lives for bearings resurfaced to $0.75b$ than those resurfaced to $0.5b$. Harris and Yu [25] have previously showed that damage is significant below $0.5b$, contradictory to the Lundberg-Palmgren assumption. Although more investigation is required to show the effect of damage below $0.5b$ in refurbished bearings, the difference between the current model and modified Lundberg-Palmgren further supports Harris and Yu's work.

2.4   Conclusion

The focus of the present investigation is to study how refurbishing can extend the useful life of bearings. The model employs a topological microstructure of Voronoi elements to represent the microstructural randomness of rolling element bearings. Rolling contact was simulated by passing a Hertzian stress across the simulated microstructure in a series of load passes. To model refurbishing of the bearings, first the original microstructure domain had a load passed over to simulate the original passes on the bearing (50% and 90% of the L_{10} life). The amount of fatigue damage from these original passes was modeled using the continuum damage mechanics approach. Refurbishing was then simulated by removing a layer of the microstructural domain to create a new bearing microstructure with a fixed amount of surface material removed (0.125, 0.25, 0.5 and $0.75b$), but the damage below the removed layers is retained. Simulated loading cycles are then passed over the refurbished microstructure until a fatigue crack reaches the surface, simulating bearing failure.

The results of the model show that increased depths of refurbishing add to the bearing life up to 0.75 of the half contact width, where the refurbished bearing lives are nearly identical to the original bearing lives. This suggests all fatigue damage occurs from the surface of the bearing to slightly below the critical shear stress reversal depth. A comparison of simulations refurbished at 50% vs. 90% of the L_{10} life shows that the earlier refurbishing results in higher remaining lives than refurbishing later; this is

consistent with previously proposed refurbishing models. It should also be noted that the current model does not take into account the additional residual stresses which are induced during the refurbishing process. Choi [40] and Warhadpande et al. [41] have shown that compressive residual stresses created from work hardening the bearing race can increase bearing lives. This could further increase the refurbished lives predicted in this model. The current approach was also compared to the Lundberg-Palmgren bearing model that has been extended to account for bearing refurbishment. The proposed damage mechanics model shows good correlation with the Lundberg-Palmgren model and both models indicate that refurbished bearings may not follow a 2-parameter Weibull curve. The results obtained from the model demonstrate significant additional life after refurbishing bearings and indicate the ideal refurbishing approach would use a long refurbishing interval with a grinding depth greater than 0.5b.

Table 2.1: Refurbishing at 50% of original expected L_{10} life.

Scenario	L_{10} Life After Refurbishing, Cycles	$\dfrac{L_{10,refirb}}{L_{10,orig}}$	Total L_{10} Life, Cycles	$\dfrac{L_{10,tot}}{L_{10,orig}}$	Weibull Slope of Lives
Pristine	$1.58 * 10^9$	-	$1.58 * 10^9$	1	7.72
0.125b removed at 50% L_{10}	$7.78 * 10^8$	0.49	$1.57 * 10^9$	0.99	3.05
0.25b removed at 50% L_{10}	$8.91 * 10^8$	0.56	$1.68 * 10^9$	1.06	3.19
0.5b removed at 50% L_{10}	$1.43 * 10^9$	0.91	$2.22 * 10^9$	1.41	6.22
0.75b removed at 50% L_{10}	$1.49 * 10^9$	0.94	$2.28 * 10^9$	1.44	6.70

Table 2.2: Refurbishing at 90% of original expected L_{10} life.

Scenario	L_{10} Life After Refurbishing, Cycles	$\dfrac{L_{10,refirb}}{L_{10,orig}}$	Total L_{10} Life, Cycles	$\dfrac{L_{10,tot}}{L_{10,orig}}$	Weibull Slope of Lives
Pristine	$1.58 * 10^9$	-	$1.58 * 10^9$	1	7.72
0.125b removed at 90% L_{10}	$3.21 * 10^8$	0.20	$1.74 * 10^9$	1.103	3.05
0.25b removed at 90% L_{10}	$4.55 * 10^8$	0.29	$1.88 * 10^9$	1.188	3.19
0.5b removed at 90% L_{10}	$1.13 * 10^9$	0.72	$2.55 * 10^9$	1.615	6.22
0.75b removed at 90% L_{10}	$1.47 * 10^9$	0.93	$2.89 * 10^9$	1.830	6.70
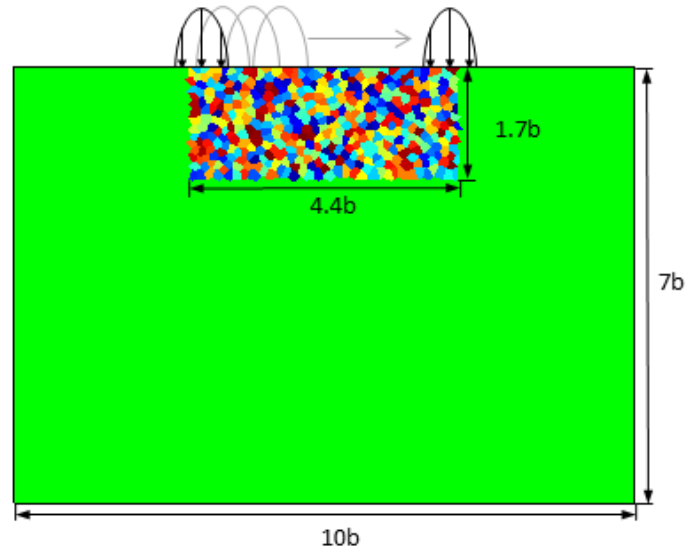
Figure 2.1: Microstructural model with static load passing over the surface. Inner region shows the extents of the random Voronoi microstructure model. Outer green region is filled with structured triangular FEA elements.
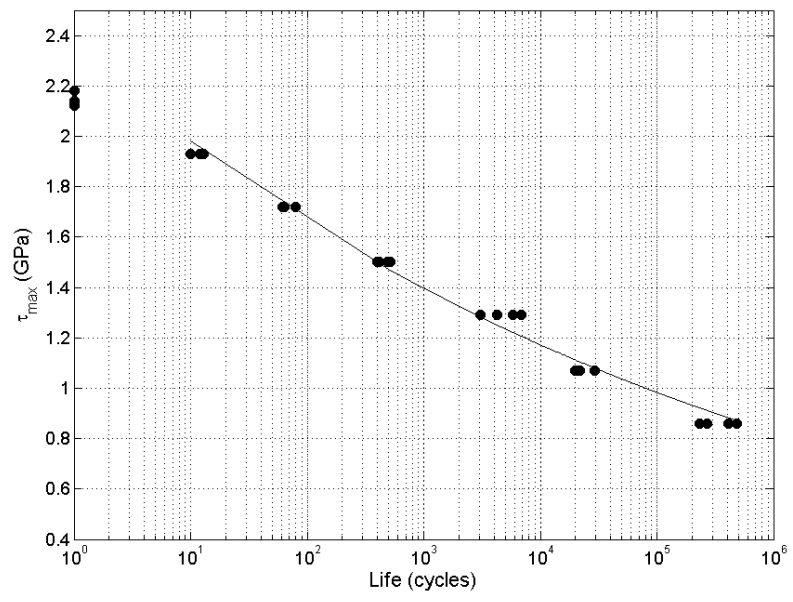
Figure 2.2: AISI 8620 case carburized steel torsion fatigue stress-life curve.
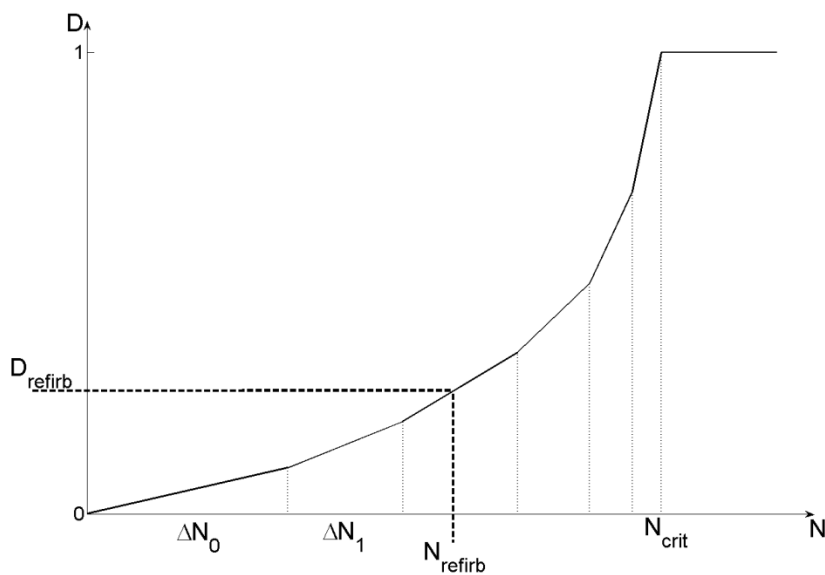
Figure 2.3: Piecewise linear damage evolution with refurbishing damage interpolation.
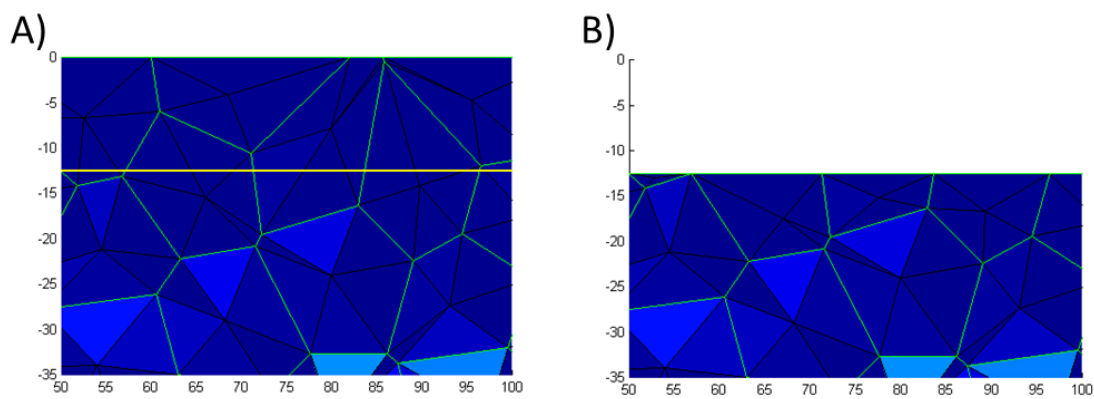
Figure 2.4: A) Original microstructure domain before resurface. B) Microstructure domain after resurfacing.
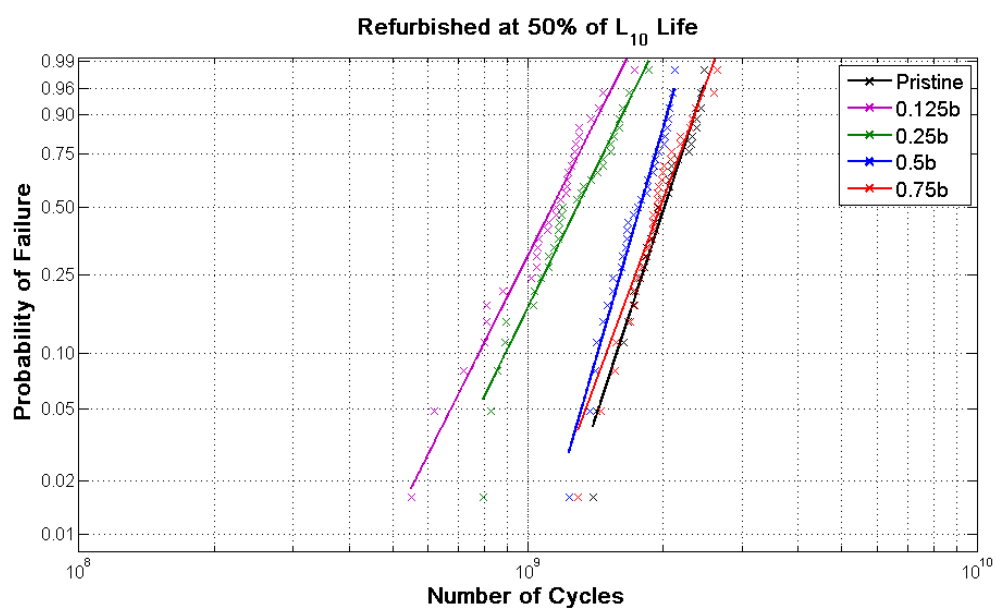
Figure 2.5: Refurbished bearing life distribution for bearings refurbished at 50% of the original L$_{10}$ life.
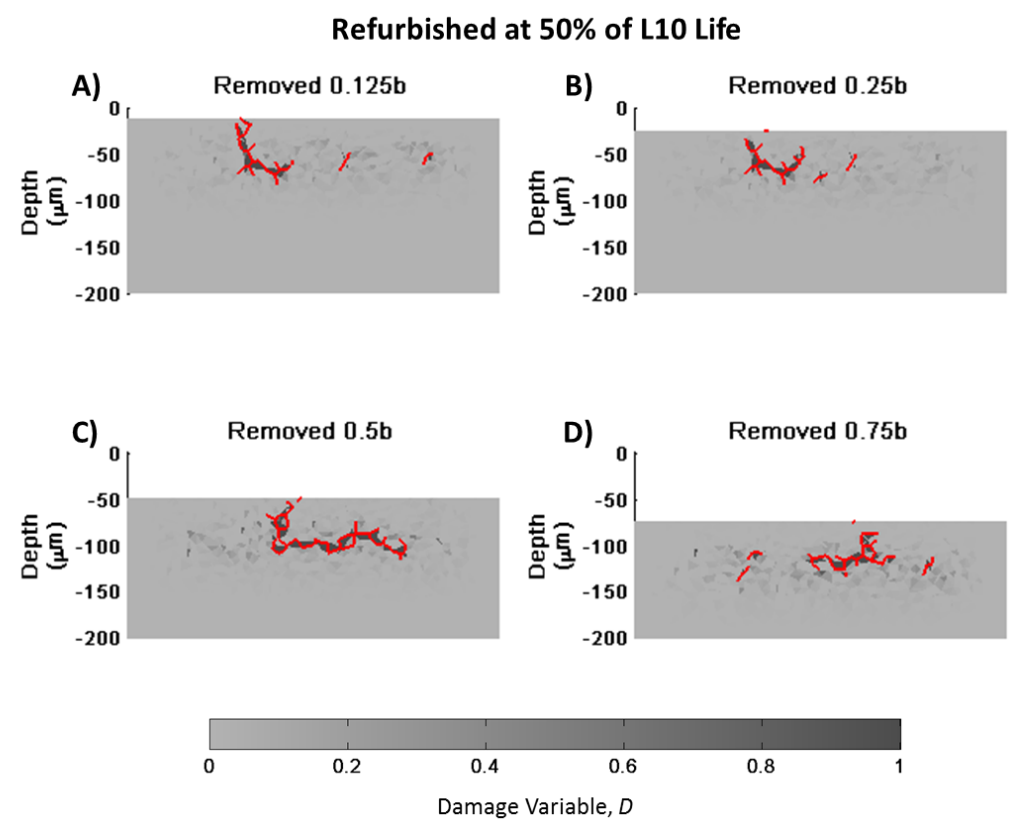
Figure 2.6: Final damage and crack profile of refurbished bearings refurbished at 50% of the original L$_{10}$ life.
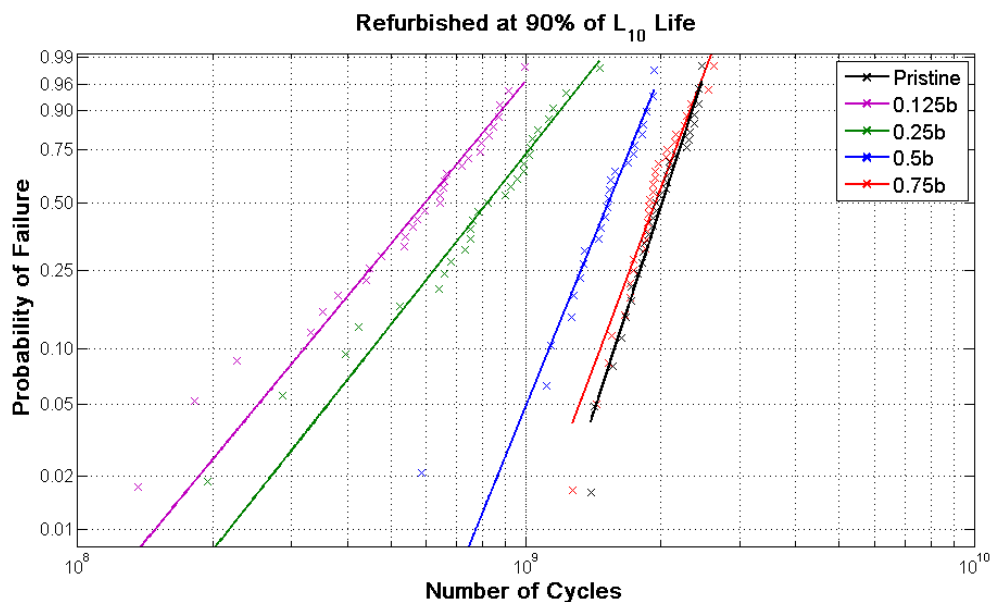
Figure 2.7: Refurbished bearing life distribution for bearings refurbished at 90% of the original L_{10} life.
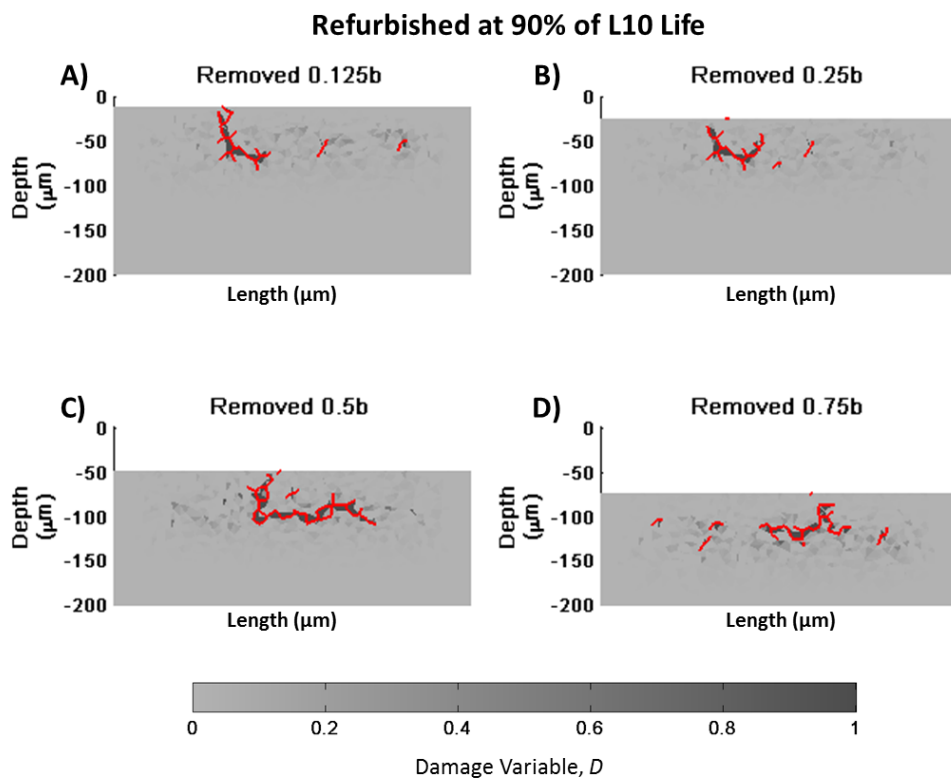
Figure 2.8: Final damage and crack profile of refurbished bearings refurbished at 90% of the original L_{10} life.
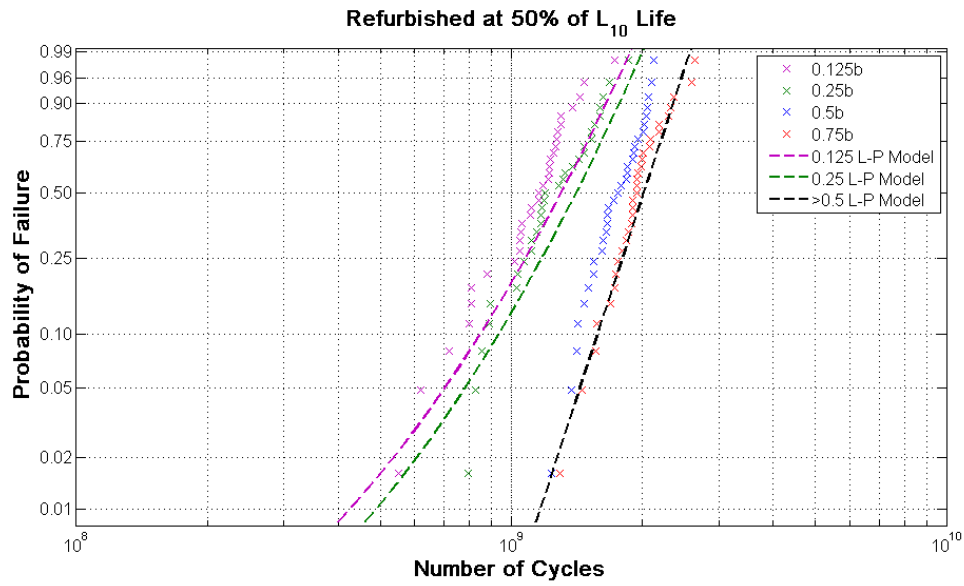
Figure 2.9: Comparison of current refurbishing model and the extended Lundberg-Palmgren (L-P) model for refurbishing at 50% of original L_{10} life.
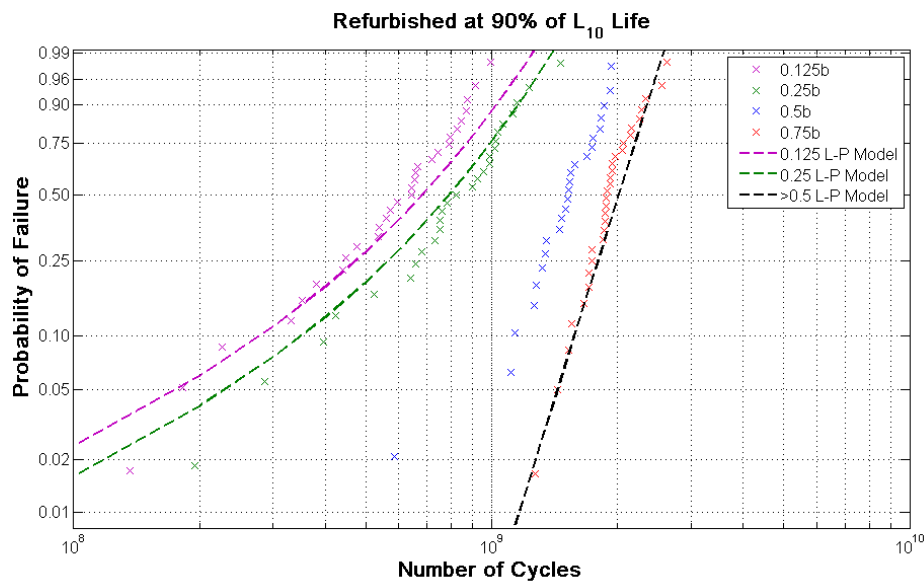
Figure 2.10: Comparison of current refurbishing model and the extended Lundberg-Palmgren (L-P) model for refurbishing at 90% of original L_{10} life.

3. EFFECT OF CRYSTAL ELASTICITY ON ROLLING CONTACT FATIGUE

3.1 Introduction

Similar to classical fatigue, RCF has been divided into stages [42]. The initial stage consists of crack initiation when the first cracks occur under the surface of the material. In the latter stages, the subsurface initiated cracks propagate growing towards the surface to form a subsurface spall. Fatigue cracks are thought to nucleate along grain slip bands in well oriented grains making the crack initiation strongly dependent on the microstructure [43]. However, not all well oriented grains initiate cracks, recent research [44] has pointed to the elastic anisotropy as the driving force that initiates cracks in the well oriented grains. In the current study, the effect of elastic anisotropy in stress is considered on initiation of rolling contact fatigue cracks.

Experimental bearing life tests for SIS, similar to most fatigue failure data, have shown a stochastic distribution of lives for identical loading conditions and bearing geometry [45]. The experimental life data closely follows a Weibull distribution [46], which is the basis of the empirical life formula proposed by Lundberg and Palmgren [5]. They postulated that the driving force behind the formation of microcracks and eventual surface spalling damage must be a critical stress in the bearing, which led them to include a critical stress in the bearing life equation. Given that microcracks initiate at the critical stress, the cracks in Hertzian contacts must then travel to the surface before a spall is formed, therefore the depth of the critical stress is related to the life of the bearing as deeper initiation cracks will lead to longer crack propagation lives before material removal by surface spalling. Finally, the volume of material in the critically stressed region is taken into account since the microcracks are assumed to initiate at weak points of the material. Combining these factors, Lundberg-Palmgren proposed the bearing life equation as:

$$\ln\left(\frac{1}{S}\right) \propto \frac{\tau_0^c V}{z_0^k} N^e \tag{3.1}$$

where τ_0, z_0, and V are the critical shear stress, the depth of the critical shear stress below the surface, and the volume of the critically stressed material. N and S are the number of

bearing stress cycles and the probability of survivability, respectively. c, k, and e are experimentally obtained exponents for a given bearing material. From the seminal work of Lundberg and Palmgren [5], RCF research has proceeded in two general directions. In the first, probabilistic engineering life models were created using the experimental measurements of life scatter [4]. Lundberg and Palmgren's work would fall into this category as well as the ISO standard for rolling bearing life [47]. The second direction of research developed deterministic life models based on mechanics of fatigue failure [9]; however, these models do not capture the stochastic nature of rolling contact fatigue. Recently a new approach to bearing models was proposed by Raje et al. [15] in which the stochastic nature of rolling contact fatigue is characterized as a function of the random microstructure in the bearing. Using this approach, a given microstructure has a deterministic life; however, when a large set of random microstructures are considered the stochastic nature of RCF life is captured. Further developments of this model have addressed 3D microstructural definitions [21], [31], [48], carbide inclusions [18], and plasticity effects in RCF [19], [41].

Previous studies investigating the microstructure of bearing steels assumed the grains were isotropic and grain boundaries were weak planes in the material where cracks could form [15]–[17], [21]. However, bearing steels are polycrystalline materials consisting of a large number of crystalline grains each randomly orientated in the domain. When many grains form an aggregate with random orientation, such as in steel, the macroscopic properties of the material become isotropic which has been shown by Bohlke and Bertram [49] and Nygårds [50]. The Hertzian contact in a rolling element bearing acts on an extremely small volume of material on a similar order to the grain size. Therefore, in order to conduct detailed stress evaluations at the roller contact, the material should not be classified as an isotropic material and an explicit representation of the grains is required [51].

In the current study, a fatigue life model with explicit definition of microstructural elements was developed to determine RCF life of rolling element bearings. Unlike previous research that focused on the microstructural topology and failure along grain boundaries as the primary cause of RCF, in this investigation, the effects of topology,

anisotropy and crystal orientation are incorporated to gain a more complete understanding of the effects of microstructure on RCF. Differences in the crystal orientations cause stress concentrations at the grain boundaries increasing the stresses in the material. The results obtained using the fatigue life model, which incorporates the life equation shown in Equation (3.1), are found to be in excellent agreement with experimental life scatter results published by Lundberg and Palmgren [3] for rolling element bearings.

3.2 Modeling Approach

3.2.1 Microstructure Topology Model

Steel is a complex microstructure consisting of a multiple phases of variable size and shape grains. Previous research [15]–[17], [52] has simplified the complex microstructure into a polycrystalline aggregate of individual grains and grain boundaries, reminiscent of an austenitic microstructure prior to any quenching. This simplified microstructure retains the effects of topological randomness which can be computationally represented using Voronoi tessellations [53]–[56]. A Voronoi tessellation divides a Euclidean space into regions with the criterion that all points in a particular region are closer to the generating point of that region than any other member of the generating set. This is similar to metal solidification where grains grow from a nucleation site until they impinge on neighboring grains. The topological randomness of a microstructure is captured by Voronoi tessellations. Voronoi microstructures are created by a randomly generated set of seed points in a domain. The regions resulting from the tessellations, known as Voronoi cells, are associated with generating points or seed points representing the grains in a material. Based on the density of the randomly generated seed points, the average size of a Voronoi cell can be determined and therefore a certain grain size can be simulated. The minimum Voronoi cell size is also set by specifying a minimum distance between seed points assuring a more uniform grain size. For this analysis, the spacing between the generating points was maintained such that the average size of the Voronoi cell was 10 μm which corresponds to the grain size of bearing steel [32].

Previous studies employing Voronoi tessellations to represent polycrystalline materials used a Voronoi centroid method to discretize the Voronoi polygons for finite element analysis [17]. Figure 3.1A depicts the Voronoi centroid discretization method wherein, finite element triangles are defined by joining each Voronoi edge to the Voronoi centroid; therefore, an N sided Voronoi polygon is discretized into N finite element triangles. The advantage of this method is a minimum number of finite elements. However, with very few elements inside each grain, it is best suited for homogeneous, isotropic material models which do not experience strong stress gradients inside the grain. The anisotropy of a material, however, causes significant stress gradients on the interior of the individual grains; therefore, an alternative method allowing for a finer discretization of the Voronoi polygons was developed for this investigation. Figure 3.1B illustrates the new method wherein, the Voronoi cell boundaries are discretized into several triangles with a meshing program (Triangle [57]). Note that area constraints are specified to ensure a sufficient number of elements inside each grain. The area constraints were tested in the material model validation described in section 3.2.2 and that same area constraint was used for all the RCF models. The quality of the elements was also ensured by limiting the minimum angle of the elements to above 20 degrees. The new meshing procedure thereby eliminates the problems created by short sided Voronoi polygons [52] in addition to addressing the stress gradients inside the Voronoi polygons. Each triangle was represented as a linear strain triangle and all the elements contained in a Voronoi cell were grouped to allow specific material properties for each grain to be assigned.

3.2.2   **Polycrystalline Elasticity Model**

On the microstructural scale, steel is a composition of anisotropic crystal grains which are randomly oriented with respect to one another. On the macroscale, where stresses are evaluated over millions of grains, the individual random grain orientations become insignificant to the global stiffness of the material resulting in isotropic material behavior. However, since critical bearing stresses operate on the microstructural scale in rolling contact fatigue, it is important to take into account how the anisotropy of the grains affects the stresses in the material. In this investigation, in order to account for grain

orientations, a cubic anisotropy model was employed similar to the approach adopted by Alley and Neu [51].

In a cubic anisotropy model, a constant crystal structure is assumed, and therefore the crystallographic elastic values that constitute the material stiffness of each crystal will be the same in the local orientation of the crystal. However, the response of a polycrystalline aggregate to loading is evaluated on the global Cartesian reference frame. This requires that the individual crystal material stiffness matrices be rotated to the global reference frame. The anisotropy of the material, i.e., the unique crystal orientation definition of each crystal, ensures that the elastic constants will change with respect to the global reference frame. The stiffness of each crystal relative to the global reference frame is obtained by the rotation from local crystal orientation to the global orientation of the model according to:

$$C_{global} = R^{-1}(\theta_3)R^{-1}(\theta_2)R^{-1}(\theta_1)C_{local}R(\theta_1)R(\theta_2)R(\theta_3) \tag{3.2}$$

where θ_i are Euler angles, R is the rotation matrix and C_{local} is the local crystal stiffness matrix. The Euler angles are randomly assigned to generate a crystallographic orientation for each grain. Even though the model simplifies the problem to a 2D plane strain problem, the grains full 3D stiffness matrix was rotated to allow all possible grain orientations; after the rotation, plane strain simplifications were applied.

Bearing steel is a complex microstructure consisting of several constituents (Ferrite, Austenite, Martensite, etc.) each having unique crystallographic properties; however, for this investigation a single-phase polycrystalline material was assumed. Although multiple constituents can be modeled with this approach, the current study focused on the effect of anisotropy without the confounding effects of multiple material definitions. The stiffness matrix used in this model was taken from the cubic material properties published in Vitos et al. [58] for steel as shown in Table 3.1. The level of anisotropy is quantified by the parameter A defined as:

$$A = \frac{2C_{44}}{C_{11}-C_{12}} \tag{3.3}$$

where C_{ij} is the value of the anisotropic stiffness matrix at a specified location defined using Voight notation. Using Equation (3.3), the anisotropy value for this material model

is calculated to be 3.78. Typical anisotropy values range from 1.2 to 8.9, which makes the current elasticity model a moderately anisotropic material [50].

In order to verify that the proposed microstructural model represents steel properties as a polycrystalline aggregate, a simple tensile study was conducted. The finite element model for this comparison was developed similar to the work of Toonder et al. [59] and Mullen et al. [60] for plain strain elements showing that polycrystalline aggregates with anisotropic grains can reproduce bulk isotropic material properties. Figure 3.2 depicts a 100 μm square polycrystalline aggregate domain with the boundary conditions for finite element analysis. Thirty microstructure domains were generated and loaded in pure tension. From these tensile results, the macroscale material properties were calculated and compared to the isotropic properties measured experimentally for steels. The bounds of the isotropic elasticity constants were calculated a priori to the finite element investigation using the Voigt and Reuss bounds for cubic materials [61]. The domain was displaced by a fixed amount and the resultant stresses were evaluated. From these stresses and the applied strain the global Young's modulus and Poisson's ratio were calculated [59]:

$$E_{FEA} = \frac{(\bar{\sigma}_{11} + 2\bar{\sigma}_{22})(\bar{\sigma}_{11} - \bar{\sigma}_{22})}{\epsilon_{11}(\bar{\sigma}_{11} + \bar{\sigma}_{22})} \tag{3.4}$$

$$\nu_{FEA} = \frac{\bar{\sigma}_{22}}{\bar{\sigma}_{11} + \bar{\sigma}_{22}} \tag{3.5}$$

where $\bar{\sigma}_{11}$ and $\bar{\sigma}_{22}$ are the average resultant stresses on the right and bottom boundaries respectively and ϵ_{11} is the specified strain in the x direction. Figure 3.3 illustrates the results of the thirty microstructures with a calculated average Young's modulus of 199 GPa and a Poisson's ratio of 0.29 which are both in good agreement with experimental measurements of steel properties.

3.2.3 Simulation of Rolling Line Contact

In typical rolling element bearings the contact pressure is nearly uniform along the axis of the roller. This contact stress is described by Hertzian contact theory as a line contact and allows a simplification to a 2D model. The loading and resulting Hertzian contact pressure in a bearing during operation is a dynamic phenomenon. However, many

studies have simplified this dynamic loading into a series of static loads moving across the surface of a small portion of the bearing raceway which constitutes the finite element domain [15]–[18], [33]. Here the same approach was adopted with the load being passed across a half space representation of bearing raceway in 21 steps. **Error! Reference ource not found.** depicts the loading condition applied to a half space microstructure model of bearing steel. To satisfy the assumptions of the Hertzian contact equations the domain was modeled using plane strain elements. Hertzian pressure distributions were applied as non-uniform, general surface traction vectors in Abaqus/Standard with the user subroutine UTRACLOAD [62]. The normal traction component was calculated using the Hertzian contact equation for a cylinder on a flat plane. The tangential component corresponds to the friction of the roller as it rolls across the surface and was modeled as a constant proportion of the normal component. In this study the coefficient of friction was set to 0.05 along the lines of previous investigations [19], [63]. **Error! Reference source ot found.** illustrates the polycrystalline microstructure within a domain 10*b* wide and 7*b* deep (b representing the Hertzian half contact width) which is a sufficient size of the half space to calculate Hertzian subsurface stresses [18], [33], [63]. The microstructure region was modeled as a cubic anisotropic material with Linear Strain Triangles (LST) while a surrounding region of isotropic LST elements was used to maintain stress accuracy at the boundaries of the microstructure. A large outer region was meshed using Constant Strain Triangles (CST) with an isotropic material representation to minimize computational effort. A tie constraint was imposed between the CST and LST regions for continuity of the stress solution [31].

3.2.4 **Fatigue Life Estimation**

The bearing life model proposed by Lundberg and Palmgren for rolling element bearing life assumes a Weibull distribution to determine the probability of spall formation at any given cycle number as shown in Equation (3.1). Raje et al. [15] proposed a new method of determining a bearing stress by setting the probability of survival and the bearing geometry terms constant; the bearing life can then be rewritten as:

$$N \propto \frac{z^c}{\Delta\tau_{xy}^k} \tag{3.6}$$

Where the life of a bearing is a function of the critical stress quantity ($\Delta\tau_{xy}$) and the critical depth (z) representing the location of the critical stress below the surface. It is important to note that this equation does not depend on a Weibull distribution. The maximum reversal of the orthogonal shear stress was selected as the critical stress quantity for the model which is the same stress proposed by Lundberg and Palmgren. Unlike many stresses occurring in Hertzian contact the orthogonal shear stress is completely reversed as the contact passes over the domain creating, thus being critical to fatigue crack initiation. In addition the maximum reversed orthogonal stress locations are in better agreement with experimental results [64] than the maximum shear stress which occurs below the experimentally observed initiation locations. Lundberg and Palmgren proposed the maximum reversal of the orthogonal shear stress as the critical stress quantity, which is also used in this investigation. The exponents (c=2.33 and k=10.33) are the same as those proposed by Lundberg and Palmgren. Using Equation (3.6) the life of a given microstructure can be determined. As illustrated in Figure 3.5, the maximum range or reversal of the shear stress among all points in a microstructural model is calculated for a rolling pass. The critical stress magnitude and depth results vary according to the modeled microstructure and therefore a unique relative life prediction is obtained for each microstructure.

3.3   Results and Discussion

In order to determine the effects of crystal elasticity or anisotropy on rolling contact fatigue it is of fundamental importance to understand how the subsurface stresses are affected by the modifications to the material model. Figure 3.6A illustrates that for an isotropic material, the subsurface shear stress due to Hertzian contact is maximum at 0.5b below the surface and the stress solution is independent of grain boundaries. Figure 3.6B illustrates the subsurface shear stress for an anisotropic material. As described in Section 3.2, the elastic stiffness of each grain is different based on its crystallographic orientation and therefore the mismatch between the stiffness matrices creates discontinuities in the stress solution. These discontinuities create stress concentrations on the grain boundaries where stresses rise above the subsurface stresses found in isotropic materials. Figure 3.7 depicts the stresses on the centerline of the contact to further illustrate the differences in

stress solution due to isotropic and anisotropic material definitions. Showing more definitively, the stresses are not continuously varying through the depth of the anisotropic material but have significant changes at locations corresponding to the grain boundaries. Below 1.25b depth, where the material definition in the model switches to isotropic, the centerline stresses follow isotropic Hertzian stress predictions very closely. However, even with the stress concentrations on the grain boundaries, the stress solution with anisotropic material definition still follows the general shape and magnitude of the isotropic stress solution.

To study the effect of different distributions of crystallographic orientations on the life of a bearing, 33 different distributions of random crystal orientations with the same microstructure topology were evaluated in rolling contact. Figure 3.8 shows the maximum shear stress reversal for all of the orientation distributions. The average critical stress is $0.85P_{max}$ in magnitude; this is higher than the critical stress of $0.5P_{max}$ predicted for an isotropic material definition. The increase in critical stress is attributed to the mismatch in orientation of the grains similar to what was shown in Figure 3.7 for the static case. The results of the 33 random orientations also show variation in the critical shear stress with a range of .75 to .95 P_{max}. The variation in the crystal orientations also influences the location of the critical shear stress as shown in Figure 3.9. The critical shear stress locations are approximately equal to the theoretical depth of 0.5b; however, the locations are scattered from 0.3b to 0.7b. In experiments conducted by Chen et al. [64], the locations of crack initiation varied from 0.35 to 0.624, which is similar to the scatter of depths found in the anisotropic model results. Also note that the critical shear stresses all occur near a grain boundary and more specifically near vertices where multiple grains meet. This further supports the view that mismatch between grain orientations causes stress concentrations.

In order to understand the influence of microstructure on fatigue life dispersion, variation in both the crystal orientation as well as the microstructure topology should be considered. To capture the full capabilities of the proposed rolling contact fatigue model, thirty-three different microstructure topologies were generated as described in section 3.2.1. For each topology, thirty-three different crystal orientation distributions were assigned,

resulting in a total of 1089 unique simulated microstructures to be evaluated. Figure 3.10 illustrates the distribution of the critical shear stress in the domains. Similar to the previous results, the magnitude of $\Delta\tau$ for all the microstructures evaluated with the anisotropic material definition is higher than the isotropic maximum shear stress reversal. The distribution of the critical stresses also shows a positive skew towards higher critical stresses with an average critical stress of $0.830P_{max}$. Table 3.2 provides a comparison between the results of the current anisotropic model to previous models for rolling contact fatigue that employed isotropic material definitions. The critical stresses in this anisotropic model are approximately 50% higher than any of the isotropic models, and the range of the data is also significantly increased by adding crystal orientation influences. Figure 3.11 shows the distribution of the critical depths. The maximum shear stress depths are centered near the isotropic maximum $\Delta\tau_{xy}$ location, 0.5b, and slightly skewed in the negative direction. The distribution is also well characterized by the experimental bounds of crack initiations observed by Chen et al. [64], with the majority of the simulation points falling inside the experimental bounds. It is valuable to note the experimental bounds of Chen et al. [64] are obtained from thirteen experimental initiation locations published, whereas the current study examines nearly 1100 critical stress locations obtained analytically. The difference in the sample sizes explains the analytical results that are outside of the experimental bounds. Compared to models using isotropic material definitions as presented in Table 3.2, the critical depth is significantly more varied with over three times the range of previously presented models, and the average depth of the critical location is slightly lower.

In order to determine a relative bearing life for each modeled microstructure, Equation (3.6) was evaluated with the critical stress magnitude and depth from the various simulations. A Weibull plot of the resulting lives is shown in Figure 3.12. A Weibull plot displays the fraction of the population that fail before a given number of loading cycles. Weibull plots are a standard tool used in the bearing industry to capture the fatigue life distribution of rolling element bearings. Initial analysis of the analytical results shows a nearly vertical distribution of Weibull points at the beginning of the curve shown in green in Figure 3.12, followed by a linear slope from that point. The vertical

distribution of points is an indication of a minimum life in the analytical results. Typically a 2-parameter Weibull distribution is used to create a continuous function from the Weibull plot data. The two parameters are the Weibull strength, representing the characteristic life of the population, and the Weibull slope, representing the scatter of the life data. An alternative method of fitting the experimental data is a 3-parameter Weibull curve, which introduces a third parameter for the minimum life of a distribution. Because of the minimum life observed in the current analytical results, the 3-parameter Weibull curve, with a Weibull slope of 1.11 and a minimum life parameter of 3.24, produced a superior curve fit than the standard 2-parameter Weibull curve. However, in order to compare to previously published results, a 2-parameter Weibull curve was also fit to the data producing a Weibull slope of 1.18. Table 3.3 provides previous Weibull slopes obtained from analytical and empirical models of rolling contact fatigue, which clearly shows the proposed model matches the empirical model results of Lundberg and Palmgren much better than the previous models, which did not take into account the anisotropy of the grains. The previous analytical models all show significantly higher Weibull slopes correlating to less life scatter in the results when compared to experimental results. These higher Weibull slopes are logical since these models only capture the variation in microstructure topology and ignore the variation due to grain orientations inside the microstructure as has been proposed in the current RCF model.

3.4 Conclusion

The main focus of the present paper is to present a model for RCF which explicitly accounts for the effects of grain topology and crystal orientation of a sample microstructure. The new model employs a topological microstructure of Voronoi elements representing the material grains wherein each grain is assigned a cubic material definition and a set of random orientation angles. Rolling contact was simulated by passing a Hertzian stress across the simulated microstructure in a series of load passes. Similar to the approach proposed in Lundberg-Palmgren theory, the maximum shear stress reversal was considered the critical fatigue stress leading to spall formation in bearings. The relative fatigue life was therefore calculated according to Lundberg-Palmgren theory. By generating microstructural models with different grain geometry

and crystal orientation thereby resulting in variation of the shear stress reversal and its location, a distribution of the fatigue lives was obtained and then compared to the experimental bearing tests life distributions.

The analysis of the current modeling results provided several insights that were not previously observed in models assuming isotropic material properties. The model displayed critical shear stresses on the grain boundaries where mismatch between the crystal orientations create stress concentrations. This supports previous work which assumed the grain boundaries as weak planes along which cracks initiate [16], [18], [19], [31], [63]. Due to the stress concentrations at the grain boundaries, the critical shear stresses in this model are significantly higher than the values predicted by isotropic Hertzian theory. The analysis of the critical shear stress depth also showed increased variation in depth from previously proposed analytical models, while the variation from the current model was in good agreement with experimentally observed crack initiation bounds. Finally, the Lundberg-Palmgren theory was applied to the model results and the dispersion in predicted fatigue lives are in excellent agreement with experimental Weibull slopes found in rolling element bearing tests.

Table 3.1: Crystal Elasticity Constants [58].

Elastic Constant	Stress (GPa)
C11	204.6
C12	137.7
C44	126.2

Table 3.2: Depth and magnitude of critical shear stress comparison to published rolling contact fatigue models.

Source	Model Type	z/a		$\Delta\tau/P_{max}$	
		Range	Average	Range	Average
Hertzian Theory	Continuum Theory	~	0.50	~	0.5
Raje et al. [15]	2D Discrete Element	0.36-0.66	0.50	0.49-0.52	0.50
Jalalahmadi and Sadeghi [17]	2D Finite Element	0.38-0.65	0.49	0.50-0.56	0.54
Weinzapfel et al. [21]	3D Finite Element	0.37-0.61	0.50	0.49-0.50	0.50
Current Model	2D Finite Element with Anisotropy	0.19-1.13	0.54	0.73-1.08	0.83

Table 3.3: Weibull slope comparison to published rolling contact fatigue models.

Source	Model Type	Weibull Slope
Lundberg-Palmgren [5]	Experimental Measurements	1.125
Harris and Kotzalas [65]	Experimental	0.7-3.5
Raje et al.[15]	2D Discrete Element	3.36
Jalalahmadi and Sadeghi [17]	2D Finite Element	2.65
Weinzapfel et al.[21]	3D Finite Element	4.55
Current Model	2D Finite Element with Anisotropy	1.18
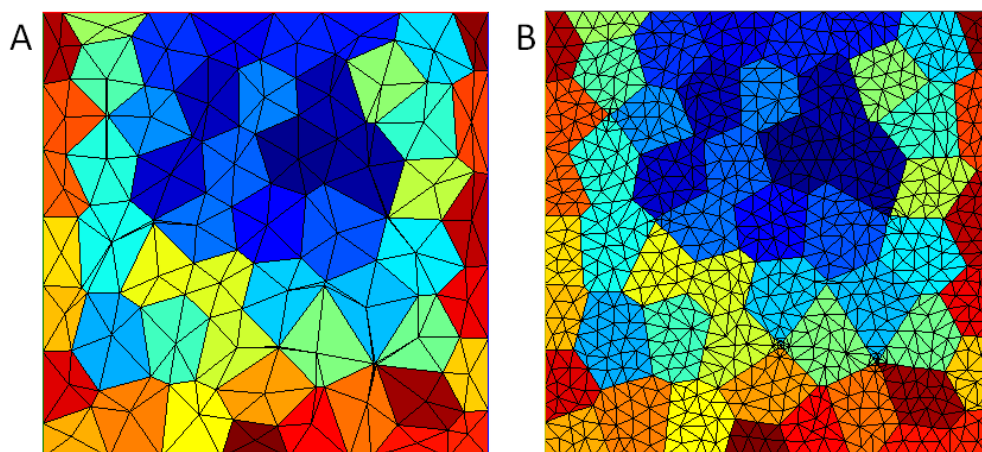
Figure 3.1: A) Voronoi Centroid meshing method. B) Meshing method used in this analysis.
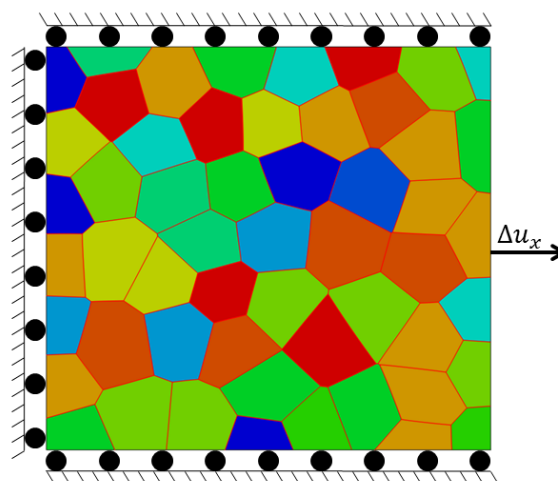
Figure 3.2: Finite element model boundary conditions for estimating the bulk material properties of a polycrystalline material adopted from Toonder et al [59] plane strain model.
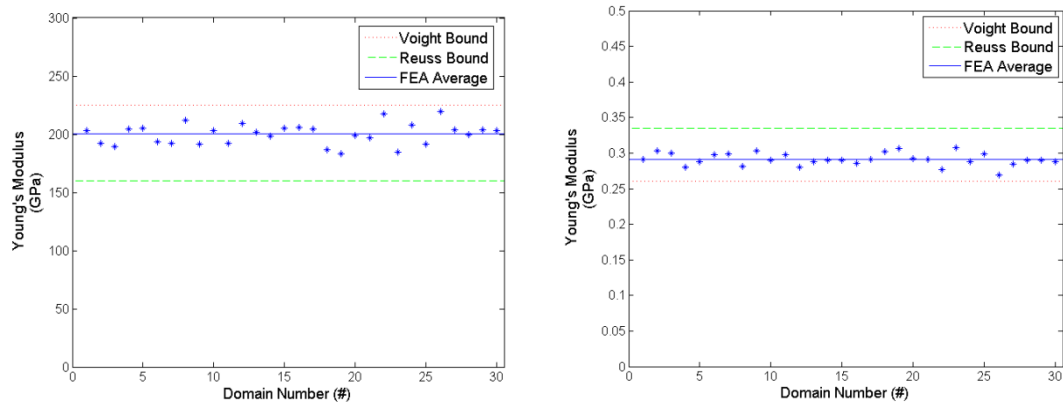
Figure 3.3: Estimate of bulk modulus properties using finite element solution for pure tension.
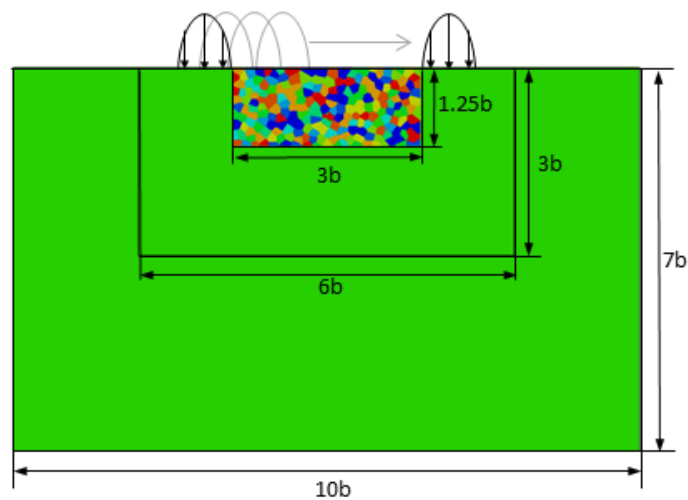
Figure 3.4: Microstructural model with static load passing across the surface. The outermost section shows the CST elements used in the domain and the inner section shows LST elements.
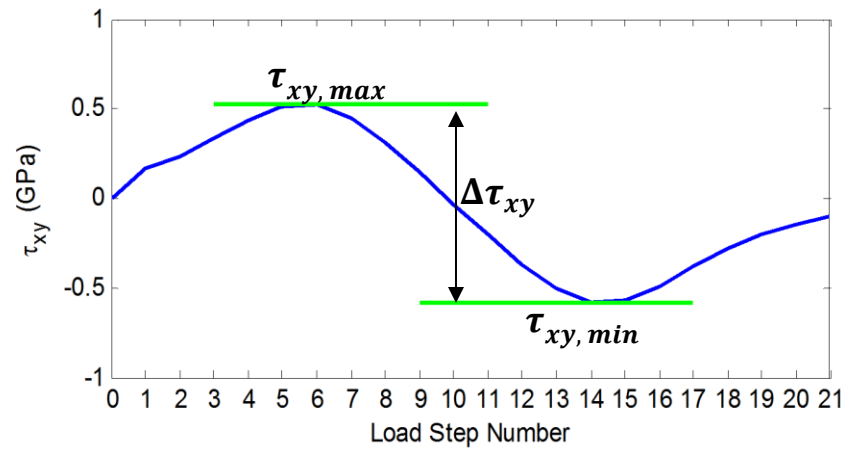
Figure 3.5: Orthogonal Shear stress is evaluated at each load step in an element and the range of the stresses is the shear stress reversal of that element.
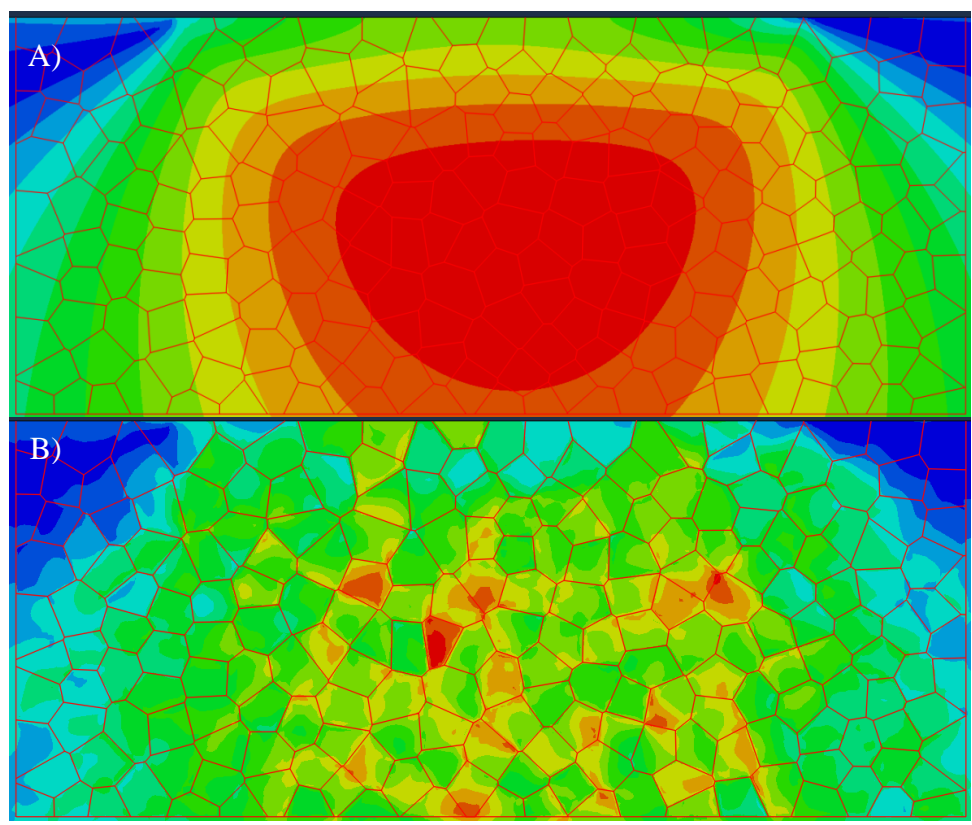
Figure 3.6: A) Maximum shear stress for a Hertzian stress in the center of the microstructure domain with an isotropic material definition B.) Maximum shear stress for a Hertzian stress in the center of the microstructure domain with the anisotropic material definition.
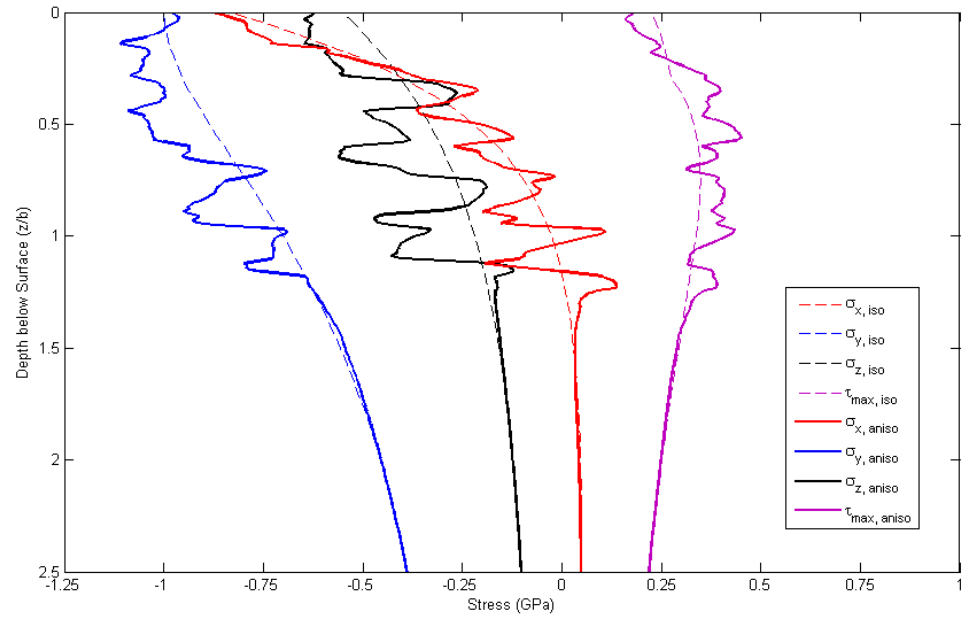
Figure 3.7: Centerline stresses for isotropic and anisotropic material definitions.
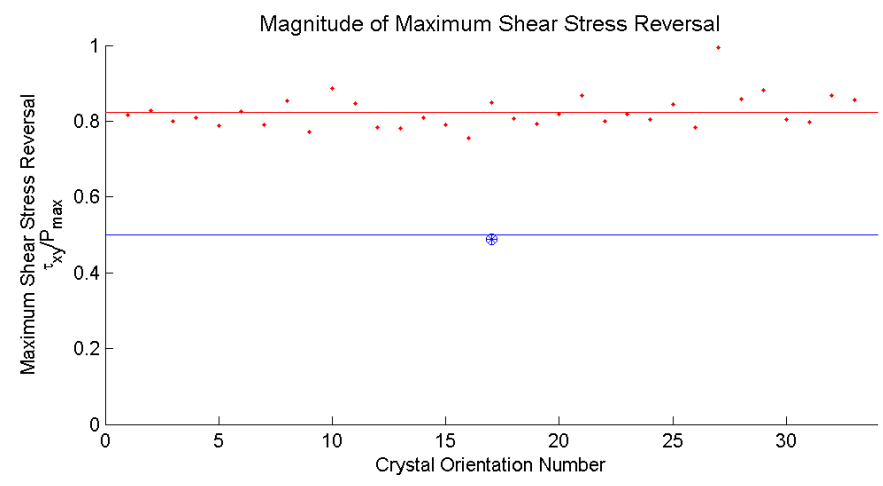
Figure 3.8: Effect of crystal orientation on the maximum shear stress reversal in Hertzian contact for a constant grain topology. The theoretical maximum shear stress reversal (blue line) and the maximum shear stress reversal from the proposed model with isotropic properties (blue point) are shown to compare with the calculated shear stress reversal from the anisotropic microstructure model (red points).

Location of Maximum Shear Stress Reversal
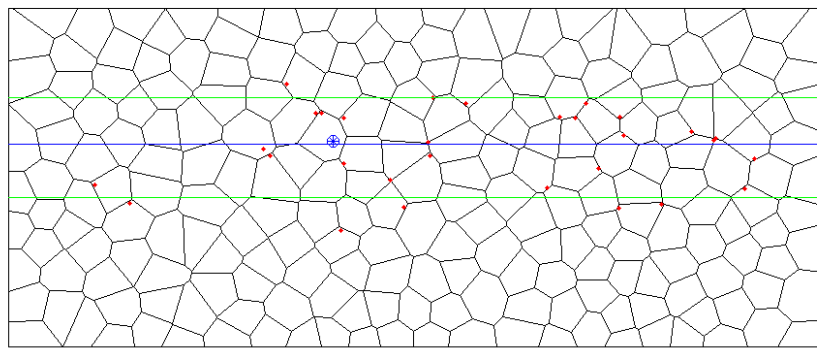
Figure 3.9: Location of maximum shear stress reversal for thirty-three crystal orientation distributions and a constant grain topology definition. The theoretical critical location (blue line) and the critical location from the proposed model with isotropic properties (blue point) are shown to compare with the critical locations from the anisotropic microstructure model (red points).
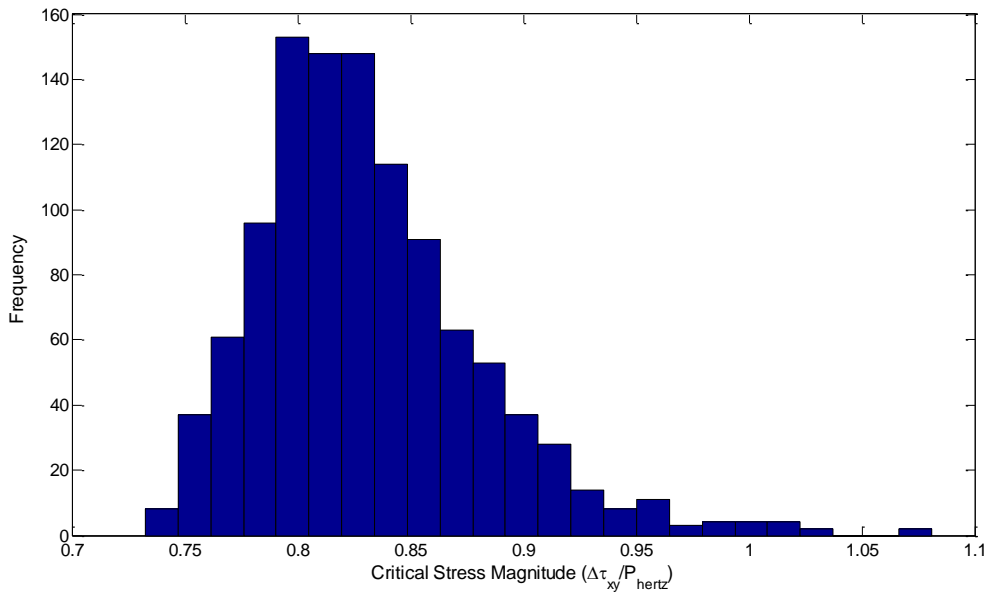
Figure 3.10: Distribution of the critical stresses for varied crystal orientations and microstructure topology.
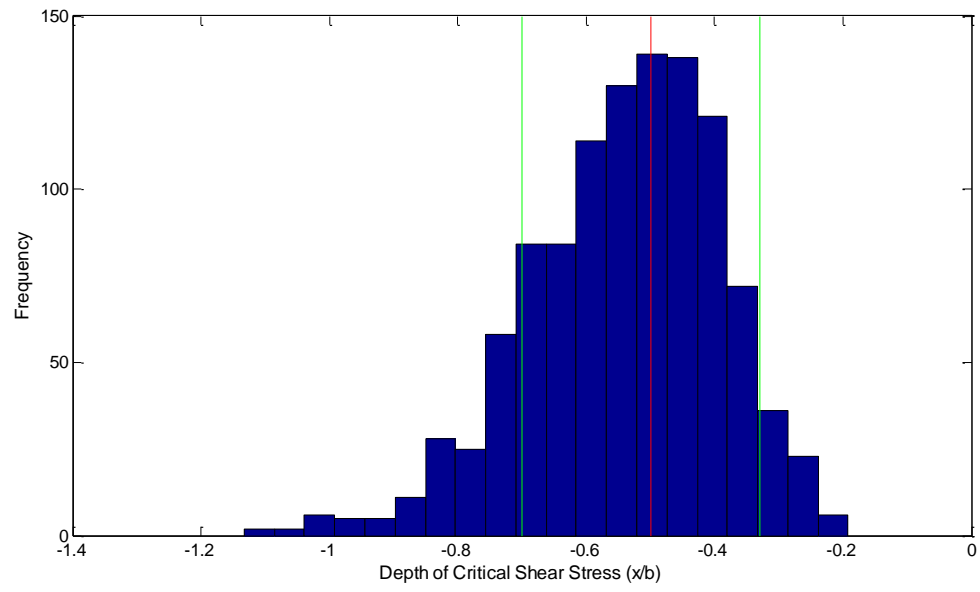
Figure 3.11: Distribution of the critical depths for varied crystal orientations and microstructure topology. Chen et al. bounds (green lines) and the theoretical critical depth (red line) show agreement with the distribution of critical stresses.
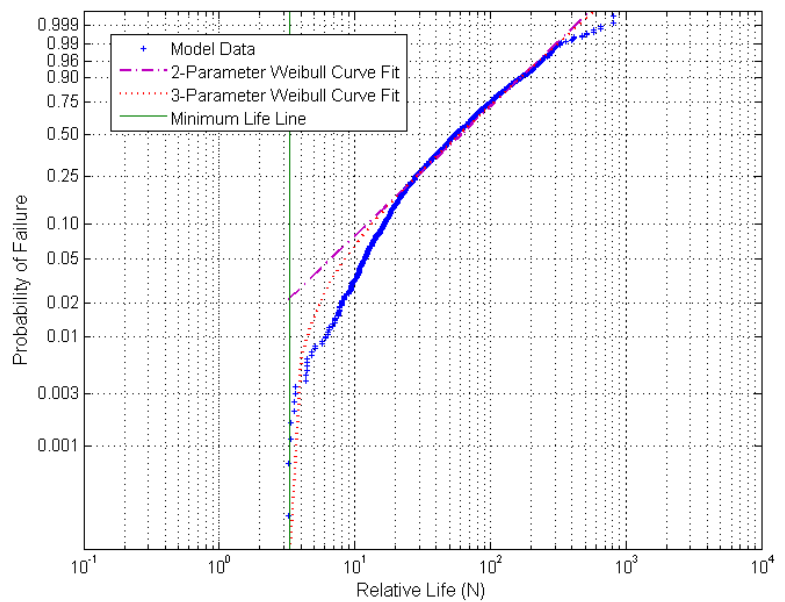
Figure 3.12: Weibull Plot of relative life results with a two and three parameter Weibull curve fit applied.

4. A COUPLED FINITE ELEMENT EHL AND CONTINUUM DAMAGE MECHANICS MODEL FOR ROLLING CONTACT FATIGUE

4.1 Introduction

Rolling contact fatigue (RCF) is the predominant mode of failure in properly lubricated, maintained and installed rolling element bearings (REB) [4]. There are two main modes of RCF failures, surface and subsurface initiated. In surface initiated RCF failure, a fatigue crack initiates on the surface and then propagates along a shallow path below the surface. This type of RCF failure is known to occur due to high friction [13] on the surface from dents, poor surface finishes, or insufficient lubrication conditions. In contrast to surface initiated RCF failures which usually can be controlled through proper lubrication and operation, subsurface initiated fatigue has not been shown to be preventable by design or operating conditions [7]. In the subsurface initiated RCF, the fatigue cracks occur below the surface of the component and are driven by the shear stress reversal. It is commonly believed that once a crack initiates it will continue to propagate until it reaches the surface and forms an RCF spall, leading to increased vibration and failure of the component.

Subsurface initiated RCF has garnered a significant amount of interest in the tribology community over the past few decades. Lundberg and Palmgren [5] published the first significant paper in the prediction of subsurface RCF, where they identified the alternating component of the shear stress to be the critical stress that initiates fatigue damage. Lundberg and Palmgren's [1] landmark publication is still significant today as both the ISO and ASME standards are derived from their work. Lundberg and Palmgren's model relies on experimental results to fit the model parameters for the fatigue life equation [4]. The need for fitting experimental results is due in a significant part to the variation seen in rolling contact fatigue spall formation. In the past few decades, RCF models have been primarily empirical, stress based and included probability and scatter through an assumed Weibull distribution function. A few researchers have also proposed deterministic stress based models that predict life and do

not incorporate the scatter in life [48]. Raje et al. [15] proposed an alternative approach which accounted for the microstructural variation in material and thus introduced statistical nature of rolling contact fatigue through modeling. Using this model, a given microstructure has a deterministic fatigue life; however, Raje and others [17], [21], [33] have shown that by agglomerating many different microstructures fatigue lives for a given set of contact conditions, the stochastic nature of the experimental results can be observed using a purely analytical model. Since its first publication this modeling approach has been extended to address 3D microstructural models [6, 9, 10], plasticity effects [19], residual stresses [41] and anisotropy of material [66].

Microstructural models have been used extensively and shown great potential for RCF modeling by demonstrating the ability to predict RCF life and scatter. While many of the limitations of original bearing models have been eliminated by this approach, one assumption that remains is nearly all RCF models use a constant Hertzian pressure to approximate the applied load. However, invariably all machine elements subject to rolling contact fatigue are lubricated and therefore the pressure distribution in these contacts is significantly different than that of Hertzian and governed by the elastohydrodynamic lubrication (EHL). In EHL, the variation of the pressure is more gradual in the inlet of the contact due to the wedge effect created by the contact geometry. Near the outlet of the contact the pressure displays a spike and steep drop in pressure as the contact geometry diverges. EHL has been investigated extensively in over the last sixty years or so. In the standard formulation of EHL models, the elastic deformation is calculated using the influence coefficient method [14, 15]. Xu et al. [69] incorporated the standard finite difference EHL equations with finite element method to determine plastic deformation in the contact region. Habchi et al. [70] developed a FEA approach that fully couples the finite element model solving the elasticity and Reynolds equations simultaneously. By incorporating the elasticity through finite elements, the stress distributions below the contact surface can be determined which is critical for calculating RCF crack formation. Cerullo [71] recently investigated the differences between RCF life predictions using EHL and Hertzian pressure profiles. This work used the Dang van fatigue criterion to predict RCF lives showing that in a pristine contact, with no inclusions or surface roughness, the EHL pressure doubled the RCF life. Using EHL

models to generate the pressure profiles also allows for the velocity effects on pressure distribution to be considered. As contact velocities increase, the EHL pressure profile deviates significantly from the Hertzian contact prediction [67].

In this paper a finite element EHL model was developed and combined with continuum damage mechanics (CDM) to investigate the effects of EHL on RCF. By coupling EHL and CDM the effects of speed and lubricant properties on pressure and consequently RCF can be critically examined. It is also to be noted because the EHL pressure is reevaluated throughout the fatigue process, the evolution of the pressure during the fatigue damage process can be investigated. The evolution of pressure for a variety of critical damage values were investigated, demonstrating the importance of this parameter in RCF.

4.2 Modeling Approach

In order to determine the effects of lubrication on rolling contact fatigue, a model was developed that couples the hydrodynamic lubrication, elastic deformation and continuum damage mechanics of the contacting surfaces. A fully coupled FE model which includes the Reynolds and elasticity equations was used to determine the internal stresses acting in the contacting bodies. The CDM model was then used to assess the degradation of the materials during the fatigue process. Voronoi tessellation was used to generate a refined computational mesh to accurately calculate the EHL pressure and damage within the contact. Figure 4.1 depicts the flowchart for the coupled DMEHL model developed for this investigation. The modeling begins with the discretization of the domain using the Voronoi tessellation. The discretized domain is then used by the FE EHL model to determine the pressure, film thickness and stresses which are passed to the CDM model. The damage variable for each element is updated by the CDM model and returned to the FE EHL model. The process continues until a damage element occurs on the surface and the process is then stopped.

4.2.1 **EHL Finite Element Model**

An FE EHL model similar to Habchi et al. [70] was developed and coupled with CDM to account for RCF damage. A basic description of the model is described below for a more complete description please refer to [70] and [72].

4.2.2 **Reynolds Equation**

The line contact steady state Reynolds equation including the modification for free boundary condition is given by [73]

$$\frac{\partial}{\partial X}\left(\epsilon \frac{\partial P}{\partial X}\right) - \frac{\partial(\bar{\rho}H)}{\partial X} - \xi \min(P, 0) = 0 \tag{4.1}$$

where

$$\epsilon = \frac{\bar{\rho}H^3}{\bar{\mu}\lambda}, \lambda = \frac{12v\mu_0 r^2}{b^3 p_h}$$

The Reynolds equation is solved along the upper contact surface of the domain Ω_c, and forms the boundary condition for the elastic deformation equation. The last term in the Reynolds equation $\xi \min(P, 0)$, is a penalty term used to drive negative pressures to zero. The outlet of the contact creates a free boundary problem where the pressure will go to zero. Unlike the finite difference approach negative pressures cannot be simply set to zero since all of the unknowns update simultaneously. ξ in Equation (4.1) is set to an arbitrarily large constant to drive the penalty term to zero.

The Reynolds Equation (4.1) requires knowledge of the film thickness (H) for the bounding surfaces. For two cylindrical bodies in contact the non-dimensional film thickness equation is given as;

$$H = H_0 + \frac{X^2}{2} - U_y \tag{4.2}$$

Where H_0 is the non-dimensional rigid body separation between the rolling elements, X is the non-dimensional distance from the contact centerline, and U_y is the non-dimensional displacement at the desired location calculated from the elastic equation.

The non-dimensionalized density [74] and viscosity [75] variation with respect to pressure are given by;

$$\bar{\rho} = 1 + \frac{0.6 * 10^{-9}P}{P_h + 1.7 * 10^{-9}P} \tag{4.3}$$

$$\bar{\mu} = e^{(\ln(\mu_0)+9.67)\left(-1+\left(1+5.1*10^{-9}P*P_h\right)^{Z_0}\right)} \tag{4.4}$$

Where,

$$Z_0 = \frac{\alpha}{5.1 * 10^{-9}(\ln(\mu_r) + 9.67)}$$

4.2.3 Elasticity Equation

In order to determine the deformation (U_y) as well as the stresses throughout the domain the elasticity equations must be solved:

$$\nabla \cdot C\nabla U = 0 \tag{4.5}$$

With the boundary conditions

$$U = 0 \text{ on the bottom surface}$$

$$\sigma_y \text{ govered by Reynolds equation (4.1) in the contact area}$$

The compliance matrix (C) is a function of the Young's modulus and Poisson's ratio. In this study, the equivalent materials properties were used to reduce the computational requirement to a single deformable body. These parameters in nondimensional form are:

$$E_{eq} = \frac{E_1 E_2}{E_1 + E_2}\frac{b}{rp_h}$$
$$\tag{4.6}$$
$$v_{eq} = \frac{v_1 E_2 + v_2 E_1}{E_1 + E_2}$$

4.2.4 Load Balance Equation

The final equation to be solved is the global load balance equation:

$$\int_{\Omega_c} Pd\Omega = \frac{\pi}{2} \tag{4.7}$$

This equation imposes that the correct load is applied and is the final equation to allow the adjustment of rigid body separation, H_0, of the contacting bodies.

4.2.5 Coupling

Equations (4.1), (4.5) and (4.7) were formulated using the Galerkin method by multiplying them by the appropriate weighting function, integrating by parts and removing null boundary conditions. The systems of equations thus become;

$$\begin{cases} \int_{\Omega_c} -\epsilon \frac{\partial P}{\partial X} \cdot \frac{\partial W_P}{\partial X} d\Omega + \int_{\Omega_c} \bar{\rho} H \frac{\partial W_P}{\partial X} - \int_{\Omega_c} \xi \cdot \min(P, 0) \, W_P d\Omega = 0 \\ \qquad \int_{\Omega} -C \, \nabla U \cdot \nabla W_U d\Omega + \int_{\Omega_c} -P \cdot W_{U_y} = 0 \\ \qquad \int_{\Omega_c} P W_{H_0} d\Omega - \frac{\pi}{2} W_{H_0} = 0 \end{cases} \qquad (4.8)$$

The Galerkin form is then solved by discretizing the problem into linear strain triangles and second order 1D elements. To solve the nonlinear Reynolds equation a modified Newton-Raphson procedure was used. Equation (4.8) is linearized with respect to each of the independent variables. The Reynolds equation is dependent on P, U and H_0 while the elasticity equation is dependent on P and U and the load balance is only dependent on the pressure P. The Newton-Raphson system of equations thus becomes:

$$\begin{bmatrix} J_{11} & J_{12} & J_{13} \\ J_{21} & J_{22} & 0 \\ J_{31} & 0 & 0 \end{bmatrix} \begin{Bmatrix} \delta P \\ \delta U \\ \delta H_0 \end{Bmatrix} = \begin{bmatrix} -R \\ -J_{21}P - J_{22}U \\ \frac{\pi}{2} - J_{31}P \end{bmatrix} \qquad (4.9)$$

Where J_{11} is the partial derivative of the Reynolds equation with respect to P; J_{12} is the partial derivative of the Reynolds equation with respect to U, etc. The Reynolds equation is stabilized using the Streamline Upwind Petrov Galerkin (SUPG) method [76]. This derivation is omitted from the current paper for brevity and the reader is referred to Habchi [72] for a complete description of the stabilization procedure.

While the above FE model is sufficient to determine the stress distribution at a fixed point in the model, the stresses within the body must be calculated over the entire rolling pass to determine how the stresses change due to the fatigue process. In order to determine this stress condition, the elastohydrodynamic pressure was traversed across the surface of a representative volume element in 21 steps moving from the right to left of the domain as shown in Figure 4.2. To approximate a semi-infinite domain the extents of the computational domain was chosen to be 60b by 60b; however, to limit the computational effort, the continuum damage mechanics model calculations were limited to a sub-region as described by Bomidi et al [31]. This sub-region is limited to -2b to 2b across and -1.5b deep.

4.2.6 **Continuum Damage Mechanics Model**

Continuum damage mechanics is used to determine the deterioration of material due to the initiation and growth of microvoids in the material [34]. Damage mechanics theory attempts to simplify the microscopic mechanism (i.e. slip planes and dislocation movement) into an empirical relationship applied on the mesoscale. The effects of the microscale failure are captured by the introduction of a damage variable, D, which affects the constitutive relationship of the modeled material. In general the damage variable is a tensor; however, for the case of isotropic damage [7, 10, 25] D becomes a scalar. For a plane strain homogenous isotropic material the stress strain including damage is given by (Lemaitre [34]);

$$\sigma_{ij} = \frac{E(1-D)}{1+\nu}\left(\epsilon_{ij} + \frac{\nu}{1-2\nu}\epsilon_{kk}\delta_{ij}\right) \tag{4.10}$$

where δ_{ij} is the Kronecker delta function. The damage variable, D, is initially zero for an undamaged material; using this value, Equation (4.10) simplifies to the standard elastic plane strain equation. As the material deteriorates the damage variable increases and the material becomes increasingly compliant until at the limiting value of 1 the material has no resistance to deformation. While Equation (4.10) describes the stress-strain and damage state in the material; an additional equation is required to determine how the damage evolves due to the continuous stress cycles. Raje et al. [6] modified the damage evolution model proposed by Lemaitre [24] to account for shear stress reversal as the critical stress. The damage evolution equation is given by;

$$\frac{dD}{dN} = \left[\frac{\Delta\tau}{\tau_r(1-D)}\right]^m \tag{4.11}$$

where $\Delta\tau$ is the shear stress reversal at the grain boundary, τ_r is the shear resistance stress representing the material's ability to resist fatigue damage, N is the number of cycles, $\Delta\sigma$ is the range of the fatigue stress, and m is the damage exponent. Both σ_r and m are experimentally determined material dependent parameters.

The two material damage parameters used in this study were determined using the approach described by Slack et al. [33]. These results were calculated using torsion fatigue results for ANSI-52100 bearing steel [77]. Using this approach the damage parameters were determined as:

$$m_1 = 10.1$$

$$\tau_{r,1} = 6.113 \, MPa$$

These values were calculated using a maximum value of damage, D_{crit}, equal to 1; however, Warhatpande et al. [78] estimated that the D_{crit} for ANSI 4142 steel is 0.12. Therefore, this research considered alternative D_{crit} values. To determine the corresponding material parameters the equation presented by Walveker et al. [79] described below was used in this investigation:

$$\tau_r = A \left[\frac{1}{m+1} - \frac{(1 - D_{crit})^{m+1}}{m+1} \right]^{-\frac{1}{m}} \tag{4.12}$$

Where A is a constant that can be calculated from m_1 and $\tau_{r,1}$. From Equation (4.12) the material parameters can be derived for different critical damage values from the same fatigue results.

Because RCF lives are typically in the millions of cycles, it is computationally infeasible to simulate every cycle. Thus, Lemaitre [34] developed an approach to extrapolate the fatigue damage calculated in one computational load pass. The method assumes piecewise periodic loading that is constant over a block cycles. The number of cycles in a given block is calculated by selecting a damage increment ΔD_{lim} and calculating the number of cycles required to reach this damage value by:

$$\Delta N = \frac{\Delta D_{lim}}{\left(dD / dN \right)_{crit}} \tag{4.13}$$

Where ΔD_{lim} is the specified change in damage, and $\left(dD / dN \right)_{crit}$ is the maximum damage rate calculated in the given load pass.

4.2.7 Voronoi Tessellation

Voronoi tessellations have been extensively used to model microstructure of polycrystalline materials [29, 30]. In order to generate a Voronoi space, nucleation points are randomly placed throughout the domain. The Voronoi polygons are then constructed by forming regions of material closest to a given seed point [82]. To insure that the generated microstructure matches the measurements of a typical bearing steel, the distribution of Voronoi seed points is set to a given mean grain size of 10μm [32].

While previous investigators [7–9, 12] have used the centroid of an N-sided Voronoi to divide into N finite elements, this approach is insufficient when the EHL pressure profiles must be solved. Due to the high gradients associated with the EHL pressure profile some areas within the domain need to be finely discretized particularly in the pressure spike region where high resolution is required for convergence of the Reynolds equation. Figure 4.3 illustrates how the finite element sizes are varied while maintaining the Voronoi boundaries. The meshing software Triange [57] allows each Voronoi polygon to be defined in the domain. A maximum finite element size is then specified in each Voronoi polygon based on the requirements of the EHL problem. In addition since the discretization requirements change as the pressure passes across the domain a different maximum finite element size is set for each load step resulting in a unique finite element domain for each load step. Once the computational domains were generated, each finite element was assigned to a Voronoi element and the damage was assigned based on the corresponding Voronoi element damage.

4.3 Results & Discussions

In order to determine the applicability and capability of the current model for RCF investigation, an initial study was performed using the operating conditions as presented by Pan and Hamrock [67] and material damage parameters as described by Slack et al [33]. Table 4.1 contains the parameters used for this evaluation and study. For this test the critical damage was set to 0.99 as described in Slack et al [33]. Figure 4.4 depicts the results from the different load passes for the proposed case. Each one of the figures displays the damage field and contact pressure for various load passes. Figure 4.4a depicts the damage state within the domain (body) for the load pass 10. For this load pass two elements have been critically damaged. Figure 4.4b illustrates that after 10 more load passes (computational cycles), three more elements have reached the critical damage level. At this point all of the critically damaged elements are separate from each other in the RVE and have initiated near the critical shear stress reversal depth of 0.5b. After 50 load passes, Figure 4.4c, no new initiation points of damage are observed instead the previous initiation points begin to grow as additional elements fail near the original initiation sites. The transition from individual damaged elements to growth of

extended damaged regions demarcates the transition from fatigue initiation to stable propagation [42]. At load pass 10 shown in Figure 4.4d, the damaged elements have coalesced to form a long dominant fatigue crack. As the load passes increase, this dominant fatigue crack continues to grow and extend across the domain as is illustrated in Figure 4.4d and e. While the fatigue damage grows, significant changes are observed in the EHL pressure profile. The decreased stiffness of the coalesced damaged region causes the pressure to decrease directly above the failed elements. This leads to both an increase in the width of the pressure profile and an increase in pressure over the undamaged material. Both of these are required to maintain the load support required by the EHL problem. It is to be noted that the change in pressure profiles is not observed in the initiation phase of the fatigue growth as Figure 4.4a and b illustrate no noticeable differences from the original EHL pressure profile. During propagation, the decrease in pressure over the damaged region will contribute to the crack growth by increasing pressure on the two edges of the damaged region. This phenomenon is seen in the progression of damage from load pass 100 to 500 (please see Figure 4.4d thorough f) as the damaged region extends steadily outward towards the maximum pressure regions.

Figure 4.4 illustrates the damage and pressure distribution at the center of the RVE (load step 11) for different load passes. However, each load pass consists of 21 load steps, thus it is important to examine the load steps across the domain for a particular damage state as shown in Figure 4.5. The first and last load steps (Figure 4.5a and f) demonstrate pressure profiles at the extreme edges of the loading region are negligibly affected by the damage state in the RVE region. This demonstrates that the contact must be directly over the damaged region for the decrease in stiffness to have an effect on the EHL pressure. Load step 5 through 17 shows a perturbation in the pressure when the contact is directly over the damaged region. In load step 5 as shown in Figure 4.5b, the damage region is located in the inlet zone of the contact leading to an extension of the inlet pressure. Figure 4.5c through e depict the load steps 9 through 17, which demonstrate a decrease in the pressure directly above the critically damage region. All of these perturbations in pressure will cause an increase in load supported by the undamaged material directly adjacent to the critically damaged region contributing to the crack propagation described by Figure 4.4.

As noted earlier, the EHL pressure is distinctly different than that of the Hertzian pressure. Most previously published work on RCF used a constant Hertzian pressure to obtain probability of failure and life. Thus in order to determine the effects of the EHL pressure on rolling contact fatigue, it was compared to a constant Hertzian pressure. The same conditions as described in Table 4.1 were used in this comparison. Before comparing the damage profiles and predicted fatigue lives it is warranted to examine the differences between a Hertzian and EHL pressure profile when no damage is present. The Hertzian pressure profile, the dotted line in Figure 4.6, has a steep pressure gradient at $X = -1$; by contrast the EHL pressure profile, solid line has a more gradual and gentle gradient into the contact zone $X \geq -1$ on the inlet side of the contact. The differences between the two pressure profiles are more prominent on the outlet side $X \leq 1$ of the contact. The Hertzian pressure is perfectly symmetric with respect to the center of the contact showing a steep pressure gradient at $X = 1$. The EHL pressure is not symmetric about the center of the contact ($X = 0$). Near the outlet region ($X \approx 1$), the EHL pressure exhibits a pressure spike immediately followed by a sharp drop in pressure and then a smooth transition to zero pressure at $X > 1$. These differences in pressure profiles will result in EHL having an asymmetric shear stress profile as opposed to the symmetric Hertzian shear stress profile. Also the smoother transition on the inlet side of the contact will decrease the shear stress observed while the steep pressure spike will increase the shear stress observed in the contact outlet. Figure 4.7 provides a comparison between the internal damage distributions of the Hertzian and DMEHL models. The damage distributions for both 50 and 100 load passes are nearly identical; however, the damage distributions deviate at the 200th load pass. The damage distribution for the EHL pressure displays a gradual growth to the surface while the Hertzian pressure has a much steeper, nearly vertical path to the surface (Figure 4.7e and f). The difference in fatigue growth between the two approaches is explained by the fixed pressure profile of the Hertzian model. Since the Hertzian pressure remains constant regardless of the damage, this high pressure forms high stresses resulting in damage propagating from the middle of the damaged region to the surface. As described previously, the fatigue damage growth in the EHL model is propagated from the edges of the damaged region due to decreased stresses directly over the critically damaged elements.

The current DMEHL and previously proposed Hertzian damage model were also used to determine the initiation and final fatigue lives. It is of interest to include a third case for comparison which uses an EHL pressure profile but does not update the pressure due to damage accumulation. Using this constant pressure profile allows the differentiation between the effect of the EHL pressure profile and the effect of dynamically updating pressure during the simulation. As noted earlier, initiation occurs when the first element reaches the critical level of damage and final life is reached when a critically damaged element reaches the surface [16], [33].

Table 4.2 contains the results for the initiation and final life for all three cases studied. Comparing the two constant pressure models, the EHL pressure predicts longer lives than the Hertzian pressure for both initiation and final life. The 3.7% increase in initiation life and the 7.1% in final life are attributed solely to the difference in the pressure distributions shown in Figure 4.6. The constant EHL pressure was next compared to the dynamically updated EHL pressure. The initiation lives of these two cases show a negligible difference since the damage accumulation has a minimal effect on the pressure distribution in the initiation stage. However, the final life is significantly affected by the dynamic pressure update increasing the final life by 7.0% compared to the constant EHL pressure. This extension of fatigue life is attributed to a long, gradual growth of fatigue damage shown in Figure 4.4. A similar increase in final life was observed by Bromidi et al. [20] when damage updated contact pressure model was compared to a constant Hertzian stress model. By combining both the EHL pressure profile and the dynamic pressure update, the DMEHL model extends the final life prediction by 16.7% compared to the Hertzian model proposed by Slack and Sadeghi [33][16] and others.

The results described previously were obtained for the same rolling velocity; however, the EHL model allows the speed to be adjusted. Speed has a significant effect on the pressure and thus will affect the calculated RCF lives. Three different non-dimensional speeds ranging from $U = 10^{-12}$ to 10^{-10} were investigated using DMEHL. Figure 4.8 depicts the pressure distributions and damage profiles for these speed cases. In the higher speed EHL case, the pressure builds more gradually in the inlet region while the pressure spike at the outlet is more pronounced. The pressure profiles show marked differences,

however the damage profiles are nearly identical for the three different speeds as observed. This indicates that the shear stress for the three different cases has a similar profile.

Table 4.3 contains the initiation and propagation lives of the three different speed cases. The results indicate that higher the speeds increase the RCF life. The difference in lives between the lowest speed 10^{-12} and highest speed 10^{-10} are 7% for the initiation life and 23% for the final fatigue lives. The increase of fatigue life as speed increases is in agreement with the results from Cerullo [71] as well as the ISO and ASME [47] speed adjustment factors. It is observed that while the final life (stress cycles) increases this does not mean the component will last a longer time as the increased speed will also increase the stress cycling rate. While the life differences shown are significant, the speed differences are large (100 times faster) between the three cases and would likely correlate to different rolling element applications in service.

In the previous sections, the effects critical damage level = 0.99 were investigated. However, the critical damage value can be significantly lower [24, 27, 28] than 0.99. Thus, to understand what role the critical damage value plays in the DMEHL model, four different critical damage values (0.125 to 0.99) were studied. Because the only difference between the four cases was the critical damage value; each test case has an identical stress distribution to begin the simulation. Figure 4.9 shows the pressure profiles and damage after 100 load passes. The pressure profiles for the critical damage value of 0.125 and 0.25, Figure 4.9a and b, show a negligible difference between the pressure profile. Figure 4.9c with a critical damage value of 0.5 shows a slight flattening of the pressure profile at the center of the contact due to damage accumulation in the middle of the domain. Figure 4.9d illustrates a clear decrease in pressure over the critically damaged region. This demonstrates that the damage model proposed is dependent on the critical damage. While it is clear from previous results that the damage affects the pressure profile, significant analysis must be undertaken to assure the critical damage is set to an appropriate level

4.4 Summary and Conclusion

In this investigation a finite element EHL model was combined with continuum damage mechanics (CDM) to determine the effects of EHL on RCF. By coupling EHL and CDM the effects of speed and lubricant properties on pressure and consequently RCF was examined. Results from the DMEHL model were compared to the previous Hertzian pressure damage model. The comparison indicates there is a significant difference in fatigue lives between the DMEHL and Hertzian models due to both the EHL pressure profile as well as the pressure changes due to the damage accumulation. The 3.7% increase in initiation life and 7.1% increase in final life were attributed solely to the differences between the constant EHL and Hertzian pressure distributions. However, the pressure update due to damage accumulation of the DMEHL model contributed to a 7.0% increase in the final life over a constant EHL pressure. When both effects were combined a 16.7% increase in final life was observed. This variation indicates an under prediction of the fatigue lives when not accounting for the EHL pressure profile and pressure changes due to damage accumulation.

The model was also used to determine the effects of speed on the fatigue lives and damage accumulation. Results demonstrate that increased speed has a positive effect on the fatigue lives. An increase in final lives of 23% was observed when the lowest and highest speeds were compared. However, the speed showed little effect on the shape or size of the fatigue damage generated in the domain. Finally the effect of the critical damage value was evaluated for the coupled DMEHL. The results illustrate that the variations in the pressure profiles are significantly affected by the level of critical damage. If the critical damage value is decreased below 0.5, the damage showed a negligible effect on the pressure profiles while higher damage values showed significant changes in the pressure profile. This illustrates the importance of setting the critical damage level for a given material when using the DMEHL model.

Table 4.1: Material and Operating Conditions.

Parameter	Value
U	10^{-11}
W	$1.3*10^{-4}$
G	5000
E_1 and E_2	212 GPa
v_1 and v_2	0.30
P_{Hz}	1GPa
b	100μm

Table 4.2: Pressure distribution effect on fatigue life predictions.

Model	Initiation Life	Final Life
Constant Hertzian Stress	$6.05*10^9$	$7.86*10^9$
Constant EHL Stress	$6.27*10^9$	$8.46*10^9$
Coupled DMEHL Stess	$6.27*10^9$	$9.13*10^9$

Table 4.3: Speed effects on fatigue life prediction obtained from DMEHL

Nondimensional Speed	Initiation Life	Final Life
10^{-12}	$6.05*10^9$	$8.49*10^9$
10^{-11}	$6.27*10^9$	$9.13*10^9$
10^{-10}	$6.52*10^9$	$1.05*10^{10}$
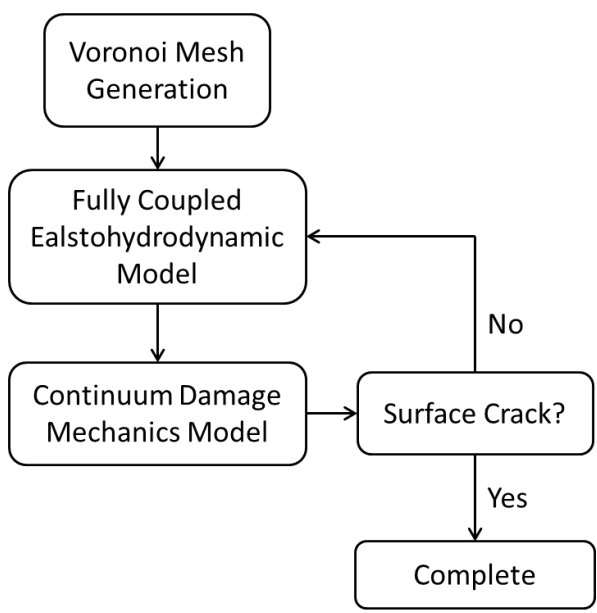
Figure 4.1: Diagram of DMEHL Model.
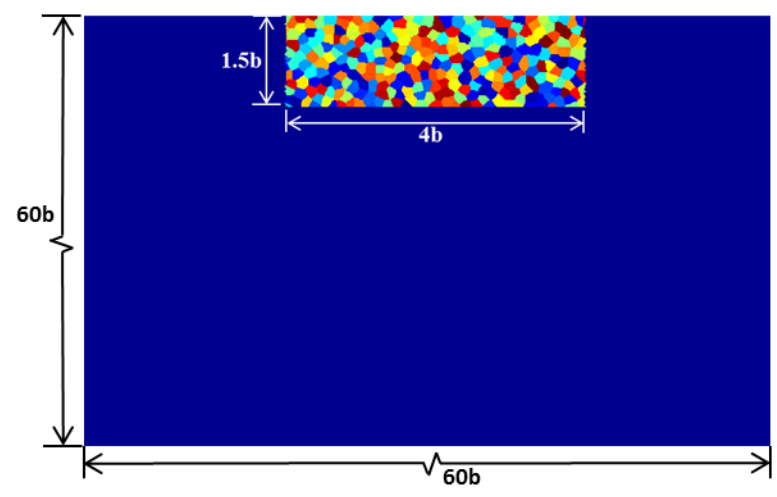
Figure 4.2: The entire computation domain is 60X60b while the representative volume of Voronoi elements is 1.5X4b. The pressure profiles are passed from right to left across the domain.
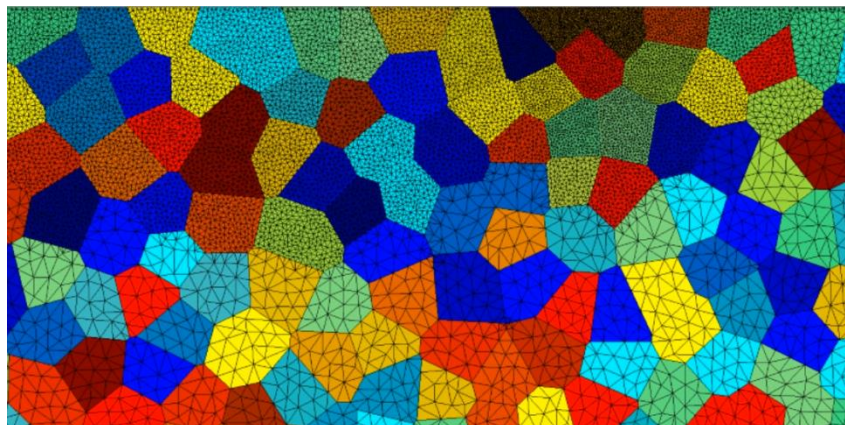
Figure 4.3: Size variation in FE domain.

a) Load Pass 10

b) Load Pass 20

c) Load Pass 50

d) Load Pass 100

e) Load Pass 200
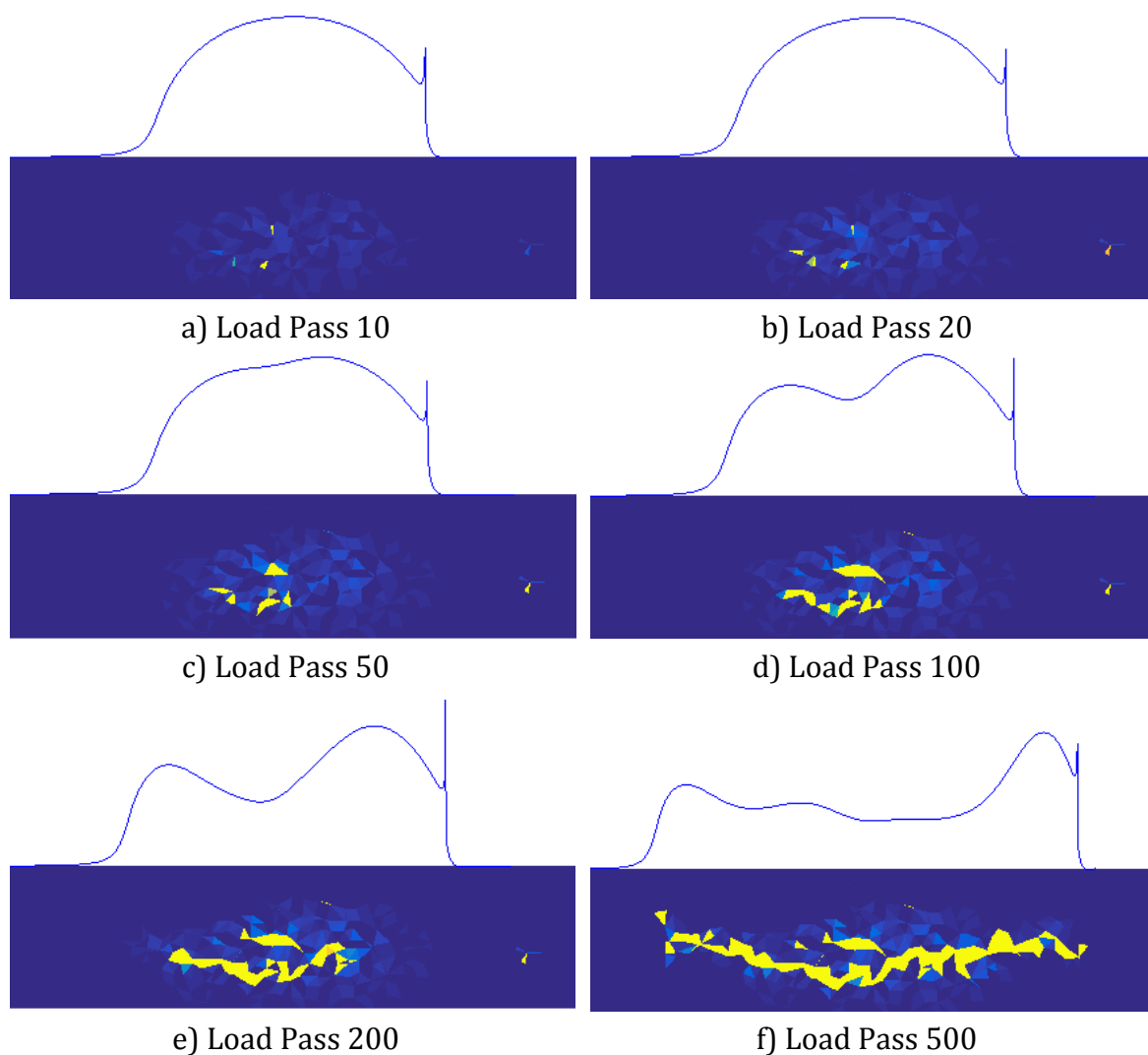
f) Load Pass 500

Figure 4.4: Damage and pressure profiles for the EHL pressure model showing the change in pressure with accumulated damage.

a)   Load Step 1

b)   Load Step 5

c)   Load Step 9

d)   Load Step 13

e)   Load Step 17
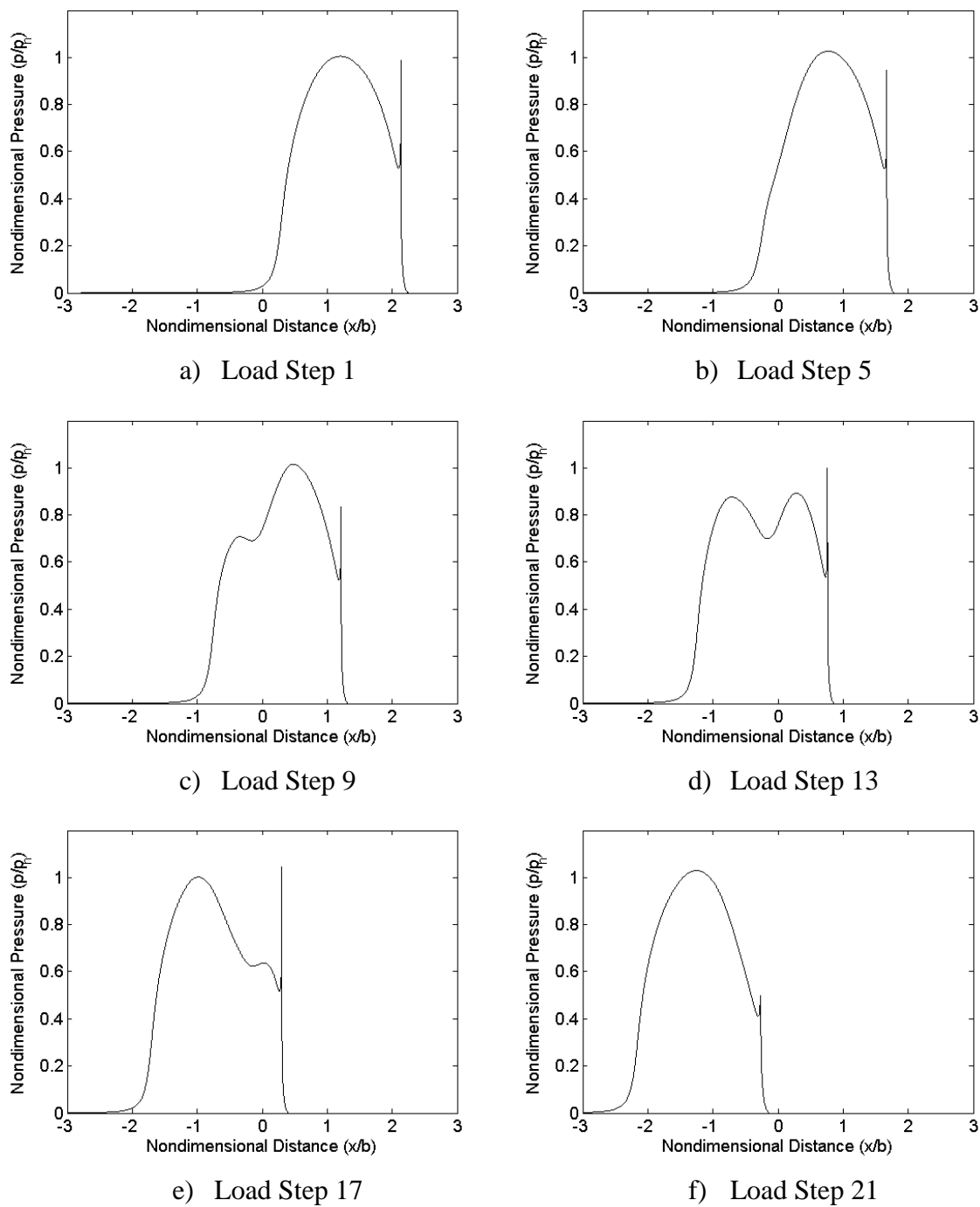
f)   Load Step 21

Figure 4.5: Progression of load steps in load pass 100.
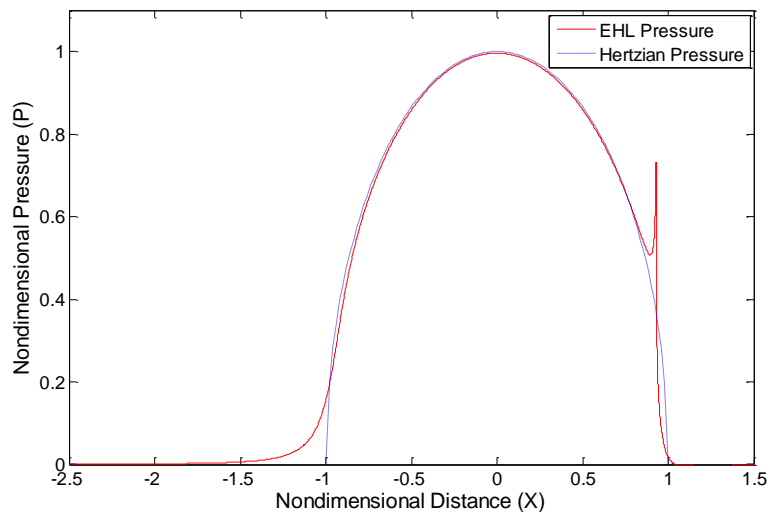
Figure 4.6: Comparison of Hertzian pressure to EHL pressure profiles.
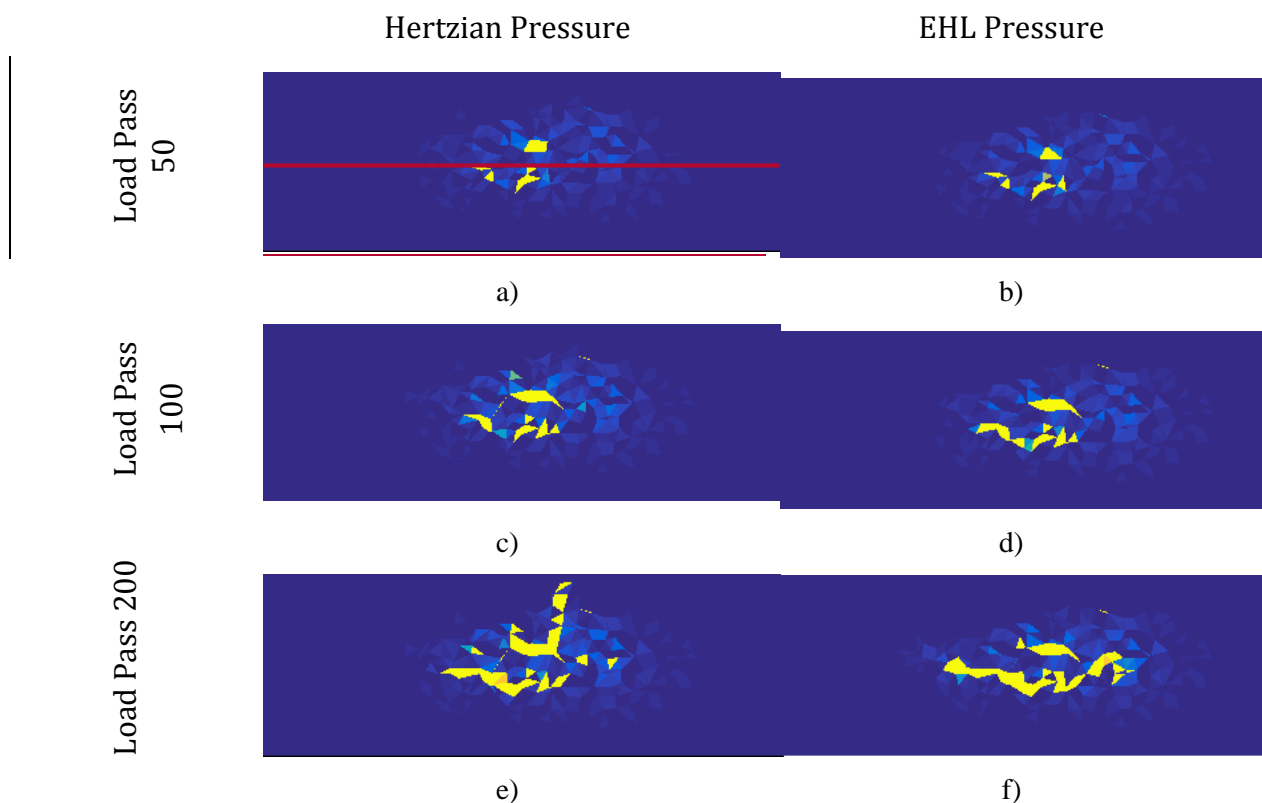
Figure 4.7: Comparison of Hertzian and dynamic EHL pressure profiles at different load passes**.**
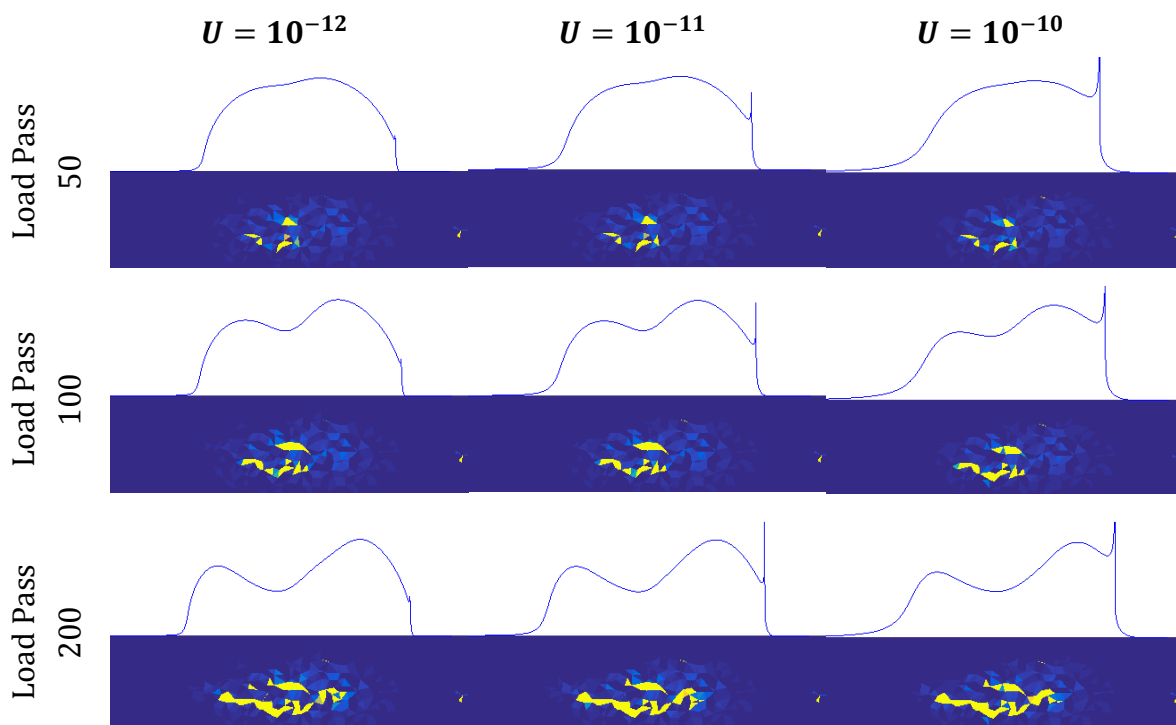
Figure 4.8: Effect of roller speed on the fatigue damage using the proposed EHL model.

a) $D_{crit} = 0.125$

b) $D_{crit} = 0.25$

c) $D_{crit} = 0.50$

d) $D_{crit} = 0.99$
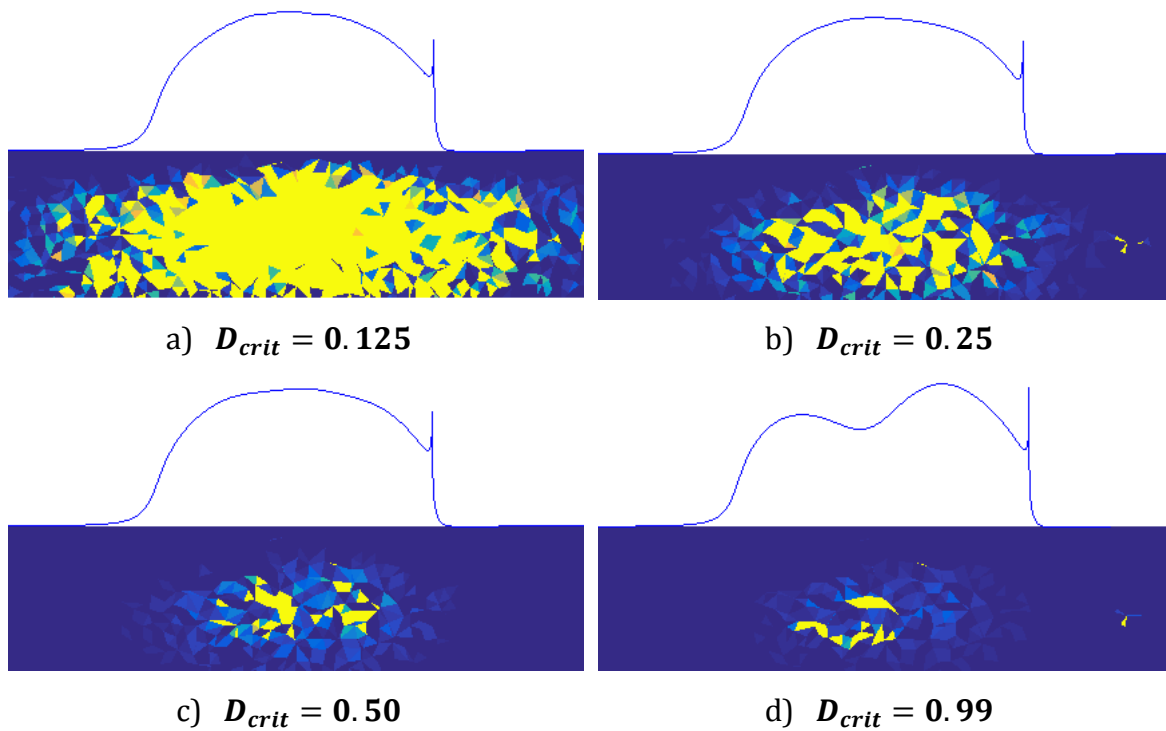
Figure 4.9: Critical damage value effect on damage development under rolling contact fatigue. All test shown after 100 computation load passes.

5. EHL MODEL OF NONHOMOGENEOUS MATERIALS: THE EFFECTS OF PHYCRYSTALLINE ANISOTROPY ON RCF

5.1 Introduction

Subsurface spalling occurs in bearing materials when rolling contact fatigue cracks initiated in the bulk of the material propagate to the surface removing a flake of material. The initiation of subsurface fatigue cracks is known to be influenced by material inhomogeneities contained in the materials [1, 2]. While nonmetallic inclusions have received the most focus of all inhomogeneities, alternative sources of material variation also affect rolling contact fatigue (RCF). Nonmetallic inclusions in bearing materials have decreased significantly by vacuum degassing and other manufacturing processes [84]; however, one source of inhomogeneity that is intrinsic to bearing steels is polycrystalline anisotropy. Bearing steels are formed by an aggregate of individual crystalline grains each with a unique grain orientation. When a sufficiently large aggregate of grains is considered the steel will behave as a homogenous, isotropic material [4, 5]. However, because EHL contacts act on a volume of material comparable to the size of few a hundred microns or grains, the homogeneous, isotropic assumption is not realistic and the polycrystalline grain structure needs to be considered to determine the stresses and pressures generated in the contact.

Recent research in rolling contact fatigue has focused on the effects of grain microstructures on the fatigue process. The effect of microstructure topology has been investigated at length as a method of introducing microstructural variation into previously explicit fatigue models [11], [15], [20], [48], [85]. Topology variations have been shown to predict the stochastic variation observed in rolling contact fatigue. While some life variations are captured using microstructural topology modeling it typically under predicts the scatter observed in experimental RCF lives [7, 11]. To address the under prediction of life variation, additional forms of microstructural variation have been incorporated into RCF models. One of the most promising additions to the microstructural model has been the addition of anisotropic material properties and crystallographic orientation to the individual material grains. Results from chapter 3

have shown that the addition of anisotropy material creates a Weibull slope much closer to experimental results than models considering only microstructure topology. A similar anisotropic model has also been proposed which incorporated cohesive elements between the grains and evaluated the effect of anisotropic properties on crack propagation in rolling contact fatigue [86]. Alley and Neu [51] recently investigated microstructure sensitivity of models that included both elastic and plastic anisotropic material models around inclusions.

While research using microstructural sensitivity has shown great promise in analytically modeling the variations observed in RCF, nearly all of the models proposed assume the rolling contact pressure is Hertzian. This assumption is accurate for unlubricated contacts; however, this is not the general operating condition for lubricated rolling contact machine elements [87]. The difference between EHL and Hertzian pressure profiles on RCF stresses has shown that EHL pressure profiles causes lower stresses and therefore predict longer lives [71]. Material inhomogeneity effects on EHL pressure and subsurface stress profiles was first studies by Slack et al. [88] using a discrete element model with inclusions coupled with an elastohydrodynamic solver. This work was extended to address multiple inclusion shapes and sizes [89], [90]. Chapter 4 developed a fully coupled finite element EHL model to determine the effect of subsurface damage accumulation on EHL pressure profiles and RCF damage propagation. Material inhomogeneities in all of the models described here have shown significant alterations to the EHL pressure and subsurface stress profiles causing a significant effect on RCF lives.

The current work develops a fully coupled polycrystalline anisotropic EHL model to investigate rolling contact fatigue of heavily loaded lubricated machine components. The approach developed within uses a 1D finite element method to discretize the Reynolds equation and a 2D FE method to resolve deformations and stresses in the polycrystalline domain. By combining these elements into a fully coupled linearize FE model the line contact EHL problem is solved for anisotropic material definitions. The contacting bodies' computational domain was discretized using Voronoi polygons of unique crystallographic orientation in order to simulate polycrystalline structured material. The coupled anisotropic EHL model was used to determine the contact pressure profiles, film

thickness profiles as well as subsurface stress distributions within the material. The contact pressures show significant variation due to the crystallographic orientations of the material which lead to stress concentrations along the Voronoi boundaries. Similarly subsurface stresses show increased magnitudes at the intersection of Voronoi elements. Due to the variable nature of the microstructure topology and crystallographic orientations significant variations are observed in the internal stress distributions. Applying the relative life prediction model to a collection of microstructural domains predicts life scatter which is consistent with experimental results.

5.2 Modeling Approach

In order to determine the effects of anisotropic polycrystalline microstructures on elastohydrodynamic lubrication, a model was developed that couples the hydrodynamic lubrication, elastic deformation and anisotropic material properties of contacting surfaces. The model was developed by coupling the finite element formulation of the Reynolds and elasticity equations of a polycrystalline material model including the microstructure of the material. Voronoi tessellations were used to simulate the anisotropic polycrystalline microstructure of the material. The Voronoi tessellation allows for unique orientation angle of each individual grain in the microstructure of the polycrystalline material being modeled. The discretized Voronoi domain is then input into the FE EHL model with the appropriate anisotropic material definition to calculate the contact pressure, film thickness and internal stresses.

5.2.1 EHL Finite Element Model

The FE EHL model implemented is an extension of the formulation proposed by Habchi et al. [70]. In the extended formulation anisotropic material properties can be specified by using an anisotropic stiffness matrix in the elastic element definitions. The fundamental equations used in the EHL model are provided below however for more details the reader is referred to [70], [72].

5.2.2 **Reynolds Equation**

Solving the EHL problem requires solving three equations simultaneously. The first of these is the line contact Reynolds equation [73].

$$\frac{\partial}{\partial \mathrm{X}}\left(\epsilon \frac{\partial P}{\partial X}\right) - \frac{\partial(\bar{\rho}H)}{\partial X} = 0 \tag{5.1}$$

where

$$\epsilon = \frac{\bar{\rho}H^3}{\bar{\mu}\lambda}, \lambda = \frac{12 v \mu_0 r^2}{b^3 p_h}$$

In the current investigation, the fluid is assumed to behave Newtonian and thermal effects are neglected. These assumptions have been shown to be accurate for low slide to roll ratios [91] like those experienced in rolling contact fatigue machine components. While Equation (4.1) is the standard form of the Reynolds equation, an additional term must be added to address the free boundary condition at the outlet of the contact. Wu [92] proposed that a penalty term can be used to drive the negative pressures to zero in the outlet region solving this free boundary problem. This results in a Reynolds equation of:

$$\frac{\partial}{\partial \mathrm{X}}\left(\epsilon \frac{\partial P}{\partial X}\right) - \frac{\partial(\bar{\rho}H)}{\partial X} - \xi \min(P, 0) = 0 \tag{5.2}$$

ξ in Equation (5.2) is set to an arbitrarily large constant to drive the pressure to zero in negative pressure regions. The Reynolds equation is solved along the contacting surfaces of the upper and lower bodies and the resulting pressure distribution is used to define the boundary conditions for the anisotropic elastic deformation. The film thickness H is defined by:

$$H = H_0 + \frac{X^2}{2} - U_{y,1} + U_{y,2} \tag{5.3}$$

Here the film thickness is a combination of the rigid body separation of the two surfaces (H_0), the geometric separation of the two bodies, approximated by a quadratic profile and the deformation of the upper and lower body surfaces ($U_{y,1}$ & $U_{y,2}$). The signs of the displacements are opposite as negative displacements of the top surface decrease the film thickness while negative displacements of the bottom surface increase the film thickness for a fixed reference frame.

The non-dimensional Dowson and Higginson [74] density pressure relationship used in this analysis is given by;.

$$\bar{\rho} = 1 + \frac{0.6 * 10^{-9} P}{P_h + 1.7 * 10^{-9} P} \tag{5.4}$$

The non-dimensional Roelands equation [75] viscosity pressure relationship used in this analysis is given by;

$$\bar{\mu} = e^{(\ln(\mu_0) + 9.67)\left(-1 + \left(1 + 5.1 * 10^{-9} P * P_h\right)^{Z_0}\right)} \tag{5.5}$$

Where,

$$Z_0 = \frac{\alpha}{5.1 * 10^{-9}(\ln(\mu_r) + 9.67)}$$

5.2.3 Elasticity Equation

Unlike most EHL models which combine two isotropic contacting bodies into a single deformable body to conserve computation resources, the current model uses independent realizations of the upper and lower bodies. This allows for a true anisotropic contact where upper and lower body crystal structures are completely independent of each other. The computational requirements to solve the problem increase due to the separate realizations; however, this required for an accurate understanding of the stresses in polycrystalline anisotropic contacts. To determine the surface deformation, the elasticity equations are solved on both the upper and lower bodies:

$$\nabla \cdot (C \nabla U) = 0 \tag{5.6}$$

With the boundary conditions

$$U = 0 \ on \ the \ non \ contacting \ surfaces$$
$$F_y = \pm P \ on \ the \ contacting \ surface$$

Care must be taken when applying the contact pressure such that the force is normal to the contacting surface. Thus, the force is positive on the upper surface and negative on the lower surface.

In this case, finding the compliance matrix is more complicated than for an isotropic material. In the proposed model a cubic anisotropic model was implemented similar to that proposed by Alley and Neu [51]. A cubic anisotropic model requires three unique

parameters to determine the compliance. These properties where obtained from Vitos et al. [58] and are presented in Table 5.1. Using a cubic anisotropic model the crystal structure of each grain is assumed constant, therefore each grain has an identical local compliance matrix. However, each grain also receives a unique global orientation represented by three random Euler angles. Since each grain has a unique orientation, the global compliance of each grain will vary based on the equation:

$$C_{global} = R^{-1}(\theta_3)R^{-1}(\theta_2)R^{-1}(\theta_1)C_{local}R(\theta_1)R(\theta_2)R(\theta_3)$$

Where θ_i is the ith Euler angle, R is the rotation matrix, and C_{local} is the crystal stiffness matrix when the primary axes are aligned with the crystal matrix. Figure 4.3 shows an example of a crystal stiffness matrix in the local and global coordinate system. After the rotations are performed the compliance matrix is condensed using the plane strain assumption [66]. Before the compliance matrix is inputted into the EHL problem the values are nondimensionalized according to the following equation

$$C = C_{global} \times \frac{b}{rp_h}$$

Where b is the Hertzian half width, r is the contact radius and p_h is the maximum Hertzian stress for an equivalent isotropic material. This nondimensionalization is useful in maintaining numerical accuracy of the problem over various operating conditions. The nondimensionalized compliance matrix is then applied to all finite elements that make up the selected microstructural grain.

5.2.4 Load Balance Equation

The global load balance is the final equations that must be solved to determine the EHL pressures and film thicknesses:

$$\int_{\Omega_c} Pd\Omega = \frac{\pi}{2} \tag{5.7}$$

This equation stipulates that the correct level of load is supported by the contact. This load level is adjusted by changes to the rigid body separation, H_0, of the contacting bodies.

5.2.5 **Finite Element Formulation**

Equations (4.1), (4.5) and (4.7) are converted to the Galerkin formulation by multiplying each equation by the appropriate weighting functions, integrating the equations by parts and removing null boundary conditions. The system of equations thus becomes;

$$\begin{cases} \int_{\Omega_c} -\epsilon \frac{\partial P}{\partial X} \cdot \frac{\partial W_P}{\partial X} d\Omega + \int_{\Omega_c} \bar{\rho} H \frac{\partial W_P}{\partial X} - \int_{\Omega_c} \xi \cdot \min(P, 0) W_P d\Omega = 0 \\ \int_{\Omega} -C \, \nabla U_1 \cdot \nabla W_{U_1} d\Omega + \int_{\Omega_c} -P \cdot W_{U_{1,y}} = 0 \\ \int_{\Omega} -C \, \nabla U_2 \cdot \nabla W_{U_2} d\Omega + \int_{\Omega_c} P \cdot W_{U_{2,y}} = 0 \\ \int_{\Omega_c} P W_{H_0} d\Omega - \frac{\pi}{2} W_{H_0} = 0 \end{cases} \tag{5.8}$$

The Galerkin form is then solved by discretizing the upper and lower elasticity problem into quadratic order triangles as well as discretizing the contact surface into quadratic 1D elements to solve the hydrodynamic problem. A modified Newton-Raphson procedure was used to solve the nonlinear Reynolds equation. All equations in Equation (4.8**)** are linearized with respect to the independent variables. The Reynolds equation is dependent on P, U_1, U_2 and H_0 while the upper and lower elasticity equations are dependent on P and $U_{1 \, or \, 2}$ and the load balance is only dependent on the pressure P. The Newton-Raphson system of equations solved at every iteration i thus become:

$$\begin{bmatrix} J_{11} & J_{12} & J_{13} & J_{14} \\ J_{21} & J_{22} & 0 & 0 \\ J_{31} & 0 & J_{33} & 0 \\ J_{41} & 0 & 0 & 0 \end{bmatrix}^{i-1} \begin{Bmatrix} \delta P \\ \delta U_1 \\ \delta U_2 \\ \delta H_0 \end{Bmatrix}^i = \begin{bmatrix} -R \\ 0 \\ 0 \\ \frac{\pi}{2} - J_{41} P \end{bmatrix}^{i-1} \tag{5.9}$$

Where J_{11} is the partial derivative of the Reynolds equation with respect to P; J_{12} is the partial derivative of the Reynolds equation with respect to U_1, etc. R is the residual of Reynolds equation. The Reynolds equation is stabilized using the Streamline Upwind Petrov Galerkin (SUPG) method [76] for a complete description of the stabilizing procedure the reader is referred to Habchi [93].

5.2.6 **Voronoi Tessellation**

Voronoi tessellation was used to generate the polycrystalline material microstructure observed in bearing steels. Previous research has shown Voronoi tessellation is an

effective method of generating polycrystalline microstructures [82]. To generate the Voronoi space, a Poisson distribution of nucleation points is randomly generated in the domain as shown by the blue points in Figure 5.2a. By mirroring the nucleation points on the flat surfaces, a flat boundary is created. With the nucleation points determined, a Voronoi cell is then generated that contain the region of material closest to a given nucleation point forming the polygons observed in Figure 5.2a. To insure the generated microstructure represents typical bearing steel, the number of generated seed points was set to generate a mean grain size of 10 μm. Once the lower contacting bodies' microstructure is generated the same process is repeated for the upper surface.

With the Voronoi tessellations completed the Voronoi cells must be discretized into a finite element domain. Previous research [94] has shown that fine discretization is needed for solving the displacement field for elastohydrodynamic lubrication particularly in the pressure spike region. Furthermore fine discretization is required to resolve the discontinuities at the intersection of anisotropic grains [66]. To achieve the appropriate level of discretization, the meshing software Triangle [95] was used which allows a maximum discretization size to be designated for each Voronoi polygon. Figure 5.2b shows the finite element discretization of a sample Voronoi domain. Since the upper and lower body surfaces are joined by 1D Reynolds elements a further stipulation is created, as each upper surface element must have a direct lower surface element counterpart. The surface nodes are then used to create 1D Reynolds elements between the two bodies. Once the finite element tessellation is completed, each element is assigned a stiffness matrix based on the Voronoi polygon to which it belongs.

5.3 Results & Discussions

In order to understand the effects of anisotropic material properties on rolling contacts operating under elastohydrodynamic lubrication, the EHL model results were compared for isotropic and anisotropic material definitions. The operating conditions used for the comparison are provided in Table 5.2. Figure 5.3 shows the contact pressure of an anisotropic and an isotropic EHL contact. The general trends for both profiles show similarities: rising gradually from near -1.5b, reaching a maximum value near the center

of the contact, then showing a pressure spike near 1b and falling rapidly to zero. However, there is significantly more variation in the contact stress in the case of the anisotropic material. This variation is due to the discontinuities in the stiffness at the grain boundaries. Due to the random orientations of the crystal microstructure, some grains will have higher stiffnesses and therefore support more load for similar deflection when compared to an adjacent differently oriented grain. The maximum observed contact pressure varies significantly between the two material models considered with the isotropic pressure having a maximum pressure of $0.98P_{Hertz}$ compared to the anisotropic maximum contact pressure of $1.16P_{Hertz}$. This 18% increase in maximum contact pressure for the anisotropic model can have a significant effect on the rolling contact fatigue life of machine elements. While there is significant pressure variation between the two material definitions, the total area under the contact pressure curve is identical due to Equation (4.7) requirements on the load supporting capacity. Therefore, at every location where the contact pressure increases in the anisotropic model, an equivalent decrease must be observed in another location. Additionally the outlet pressure spike is slightly different between the two models with a location of 0.83b vs 0.81b for the anisotropic model.

In addition to the contact pressure it is also of interest to understand the differences in the film thickness profiles between an anisotropic and isotropic material model. The variation in the film thickness between the two material models is much less significant as can be observed in Figure 5.3. While the maximum contact pressure was increased by 18%, the minimum film thickness variation was only 2% between the two material models. The isotropic material model showed a slightly smaller minimum nondimensional film thickness of 0.92 while the anisotropic material model had a minimum nondimensional film thickness of 0.94. The slight decrease in the apparent contact width observed in contact pressure profiles can also be observed in the film thickness profiles. While the film thickness shows more similarity between the anisotropic and isotropic profiles, there are clear fluctuations of the anisotropic film thickness around the isotropic film profile.

While the variation of a given anisotropic microstructure from the isotropic model is interesting, the exact microstructure of a contact is generally not known and different microstructures will produce different stress distributions. Therefore, it is useful to understand the general variations caused by anisotropic material definitions on the contact pressures and film thicknesses. To understand these variations, a group of 33 different microstructures were generated and the standard deviation of the population was calculated for the film thickness and contact pressure parameters. Figure 5.4a shows the mean and standard deviation of the anisotropic models contact pressure as compared to an isotropic profile. As can be seen in the figure, the mean closely follows the isotropic contact stress profile. The standard deviation provides a useful estimate for how much anisotropic pressures will deviated from the isotropic contact pressure estimates. For the given anisotropic properties, the deviation is between 5 and 10% near the center of the contact. Furthermore, the location of the pressure spike is only slightly affected. The film thickness profiles obtained from the same 33 simulated microstructure domains illustrate minimal difference between the results. As demonstrated in the film thickness profiles in Figure 5.4, there are negligible variations between the microstructural domains and the mean anisotropic profile closely follows the isotropic prediction.

The film thickness and contact pressure profiles are used to investigate the effects of anisotropic material on elastohydrodynamic contacts; however, to understand how these effects are manifested in rolling contact fatigue, the subsurface stresses must be examined. To study the effects of anisotropic properties on the stress profiles, Figure 5.5 demonstrates a comparison between the normal stress components of anisotropic and isotropic materials along the centerline of the contact for the same microstructural domain used to generate Figure 5.3. The stresses are shown from the surface to a depth of 1.2b. This is a sufficient depth to capture any stress variations that would affect the rolling contact fatigue behavior [31]. The results demonstrate that there are clear differences between the subsurface stress profiles for anisotropic and isotropic material definitions. For all normal stresses, the stress at the surface for the anisotropic material is significantly higher than the stress predicted using an isotropic model. This is expected since the contact stress from Figure 5.3 is also higher at the centerline of the contact. Further into the depth of the material significant fluctuations in the normal stresses are

observed in the anisotropic materials. These fluctuations correspond to the locations of grain boundaries where crystal orientations change, leading to stress concentrations on the grain boundaries. While the stresses in the anisotropic model show significant deviation from the isotropic material model, it should be noted, both material definitions show the same general trends for the stress profiles. Figure 5.6 depicts the centerline subsurface shear stresses for the anisotropic material. The isotropic stress profiles are not shown in this figure since the out-of-plane shear stresses are zero for the plane strain isotropic material conditions. It is also to be noted that the centerline in-plane shear stress is nearly zero along the centerline for isotropic EHL material. Unlike the isotropic model, the anisotropic material model shows significant shear stresses at the centerline of the contact. The observed stresses show similar trends to the normal components in that there are significant fluctuations at grain boundaries. The maximum shear stress magnitudes for the anisotropic material reach $0.2p_{Hertz}$ for in plane shear and $0.1p_{Hertz}$ MPa for out of plane shear stress.

Figure 5.5 and Figure 5.6 show the variations of individual stress components, however, an orientation independent stress that combines all of the stress components is required to evaluate the effect of anisotropy on fatigue lives. Ioannides and Harris [7] have proposed the von Mises equivalent stress as the best method of combining the effects of all stresses generated in rolling contact fatigue, while Zaretsky [8] has proposed maximum shear stress as the critical stress in rolling contact fatigue. This analysis has considered both stress quantities as the critical stress for rolling contact fatigue crack initiation. Figure 5.7 shows the von Mises stress profiles for an isotropic and anisotropic material model respectively. The isotropic von Mises stress profile has a maximum value near the contact centerline at a depth of approximately 0.55b below the surface. From that maximum point, the von Mises stress decreases in approximately elliptical isolines radiating from the maximum point. The stresses skew slightly towards the contact outlet where the sharp gradient at the pressure spike increases the subsurface shear stresses. The anisotropic von Mises stress profile observed in Figure 5.7b shows the effects of the grain dependent crystal orientations on the stress profiles. While the largest stress magnitudes are still observed near the center of the contact and below the surface between 0.45 and 0.85b, the stress peaks are isolated along the grain boundaries and do

not show the smooth transition observed in the isotropic stress profile. Furthermore, the maximum stresses are significantly higher than those observed in isotropic stress profiles with the maximum stress equal to $0.91p_{Hertz}$ whereas the maximum von Mises stress for the isotropic model was $0.56p_{Hertz}$. This $0.35p_{Hertz}$ increase is directly related to the stress concentrations generated at the grain boundaries. Another important distinction between the two material models is the distribution of the von Mises stress values in the domain. Instead of a single global maximum stress location, anisotropic materials show several local stress maxima in isolated regions of the domain. For example three local stress maxima are observed in Figure 5.7b at (0.10,-1.23), (0.62,-0.35), and (0.53,-0.92). These stress maxima form hot spots for fatigue crack initiation and can form multiple initiation locations as observed in typical rolling contact fatigue spall formation. Figure 5.8 shows the comparison of the maximum shear stress observed for the isotropic and anisotropic materials considered in this investigation. The results are similar to the equivalent von Mises stress profiles in that the isotropic material shows a smooth stress distribution while the anisotropic stress has stress risers at the grain boundaries. The maximum shear stress observed for the isotropic profiles is $0.3P_{Hertz}$ while the maximum shear stress for the anisotropic stress is $0.495p_{Hertz}$.

Using the analytical modeling extension of the Lundberg and Palmgren [5] proposed by Raje et al. [15], the effects of microstructural stress variation can be analytically studied using the equation:

$$Life \propto \frac{y^{2.33}}{\sigma_{max}^{10.33}} \tag{5.10}$$

Both the maximum von Mises stress and maximum shear stress are used as the critical stresses, σ_{max} and y corresponds to the depth of the maximum stress of interest. Using this equation a relative life can be determined for each microstructural domain.

Figure 5.9 shows the maximum von Mises and maximum shear stresses for the 33 microstructural domains studied in this investigation. For the von Mises stress, the stress magnitudes for the anisotropic materials average $0.92p_{Hertz}$ which is significantly higher than the stresses predicted for isotropic material of $0.55p_{Hertz}$. The von Mises stresses also show significant variation between different microstructural domains with a standard deviation of approximately 10% of the mean. This variation is responsible for the scatter

in the relative life equation (10). The maximum shear stress results have a similar variation to the von Mises stress; however, the stress magnitudes are lower. The mean shear stress for the anisotropic domains is $0.49p_{Hertz}$ as compared to $0.3p_{Hertz}$ for the isotropic material.

Unlike the stress magnitudes which average significantly higher than the isotropic model predictions, the locations of the critical stresses are centered near the isotropic material model prediction of -0.55b. Figure 10 depict the locations of maximum von Mises and the maximum shear stresses. The figure shows there is significant scatter in the locations of the maximum stresses between the different microstructural domains. The minimum depth near 0.3b for both stress criterion correlates well with experimental investigation conducted by Chen et al [64] observing subsurface fatigue cracks originate at a depth of 0.3b below the surface. The maximum stress locations skew towards deeper locations with most depths congregated between 0.3b and 0.9b. The deepest stress for the von Mises and maximum shear stress are 1.23b and 1.33b respectively, significantly lower than that predicted by the isotropic model.

Using the stress magnitudes and locations described in Figure 5.9 and Figure 5.10 in Equation (5.10), a relative life can be predicted for each microstructural domain. Figure 5.11 depicts the Weibull plots using the von Mises and maximum shear stresses as the critical stress criterion, respectively. The scatter in the results was then fitted with a two parameter Weibull curve as shown by the solid lines. Extracting the slopes of the Weibull curves is a measure of the life scatter for the given model. For the proposed model the Weibull slope for the von Mises critical stress is 1.06 and 0.96 for the maximum shear stress criterion. The Weibull results obtained represent significantly more scatter that is observed in isotropic microstructural models as shown in

Table 4.2. While the results show more scatter than has previously been observed in analytical models, the calculated Weibull slopes are similar to the experimental results observed by Lundberg and Palmgren of 1.125 as well as the range proposed by Harris and Kotzalas [65] of 0.7 to 3.5. The Weibull curves show that using the anisotropic material definition for EHL contacts will increase the scatter observed for analytical

studies and estimates the Weibull life scatter similar to those observed in experimental investigations.

5.4   Summary and Conclusion

In this investigation a fully coupled finite element elastohydrodynamic lubrication (EHL) model was developed to study the effects of crystal anisotropic material properties on EHL line contacts and corresponding RCF of machine elements. The model developed allows for the investigation of isotropic and anisotropic material effects on film thickness, contact pressures as well as internal stresses generated within the contacting surfaces. The computational effort for the fully coupled finite element EHL model for anisotropic material is slightly more than that of the homogenous isotropic material assumption. Voronoi tessellated polygons were used to simulate steel microstructure grains and random orientations were assigned to each individual grain. These changes produced an EHL solution method which can solve anisotropic material models.

Using the EHL model the effects of anisotropy material was investigated with a primary focus on how anisotropic material would affect rolling contact fatigue life of heavily loaded lubricated contacts. The contact stresses observed using anisotropic material properties show significant variations due to the discontinuous stiffness along the grain boundaries.   These stress variations affect the stresses for rolling contact fatigue modeling.   Conversely, the film thickness profiles are minimally affected by the anisotropic material model with minimal variation observed between anisotropic and isotropic material models. Observing the subsurface stresses which are the driving force behind rolling contact fatigue, all stress components show significant variations with the anisotropic material model. The results show stress hot spots on the grain boundaries which will lead to the formation of rolling contact fatigue cracks. By agglomerating the subsurface stresses of numerous microstructural domains using RCF relative life equation calculations, a population scatter was obtained for the model. The resulting Weibull slope is 1.04 and 0.99 for the von Mises and maximum shear stress respectively. Both of these values show significantly more scatter than is observed with similar isotropic

material models and the resulting slopes compare well to experimentally observed Weibull slopes.

Table 5.1: Crystal Elasticity Contacts.

Elastic Constant	Stress (GPa)
C11	204.6
C12	137.7
C44	126.2

Table 5.2: EHL Operating Conditions.

Parameter	Value
U	10^{-11}
W	$1.3*10^{-4}$
G	5000
P_{Hz}	1.0 GPa
b	100μm

Table 5.3: Weibull Distribution Slopes.

Source	Model Type	Weibull Slope
Lundberg-Palmgren [5]	Experimental	1.125
Harris and Kotzalas [65]	Experimental	0.7-3.5
Raje et al. [15]	2D Isotropic Hertzian	3.36
Jalalahmadi and Sadeghi [17]	2D Isotropic Hertzian	2.65
Weinzapfel et al. [21]	3D Isotropic Hertzian	4.55
Current Model	Von Mises Stress	1.06
Current Model	Maximum Shear Stress	0.96

Local Stiffness Matrix

$$\begin{bmatrix} 205 & 138 & 138 & 0 & 0 & 0 \\ 138 & 205 & 138 & 0 & 0 & 0 \\ 138 & 138 & 205 & 0 & 0 & 0 \\ 0 & 0 & 0 & 126 & 0 & 0 \\ 0 & 0 & 0 & 0 & 126 & 0 \\ 0 & 0 & 0 & 0 & 0 & 126 \end{bmatrix}$$

Global Stiffness Matrix

$$\begin{bmatrix} 295 & 125 & 60 & 4 & 24 & 25 \\ 125 & 250 & 105 & -14 & -16 & -46 \\ 60 & 105 & 315 & 10 & -8 & 21 \\ 4 & -14 & 010 & 113 & 25 & -16 \\ 24 & -16 & -8 & 25 & 49 & 10 \\ 25 & -46 & 21 & -16 & 10 & 94 \end{bmatrix}$$
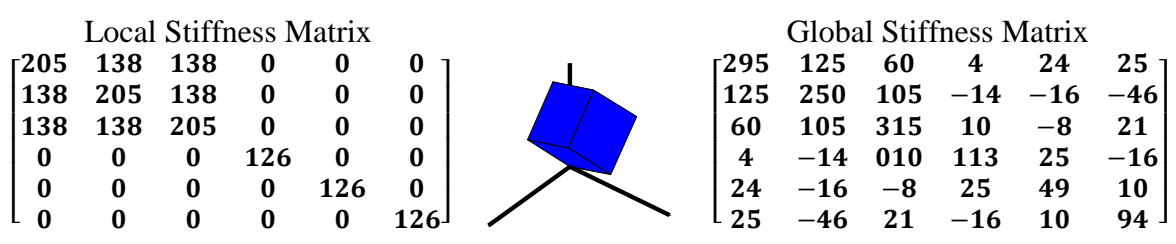
Figure 5.1: Stiffness matrix for global and local orientation.

a)

b)
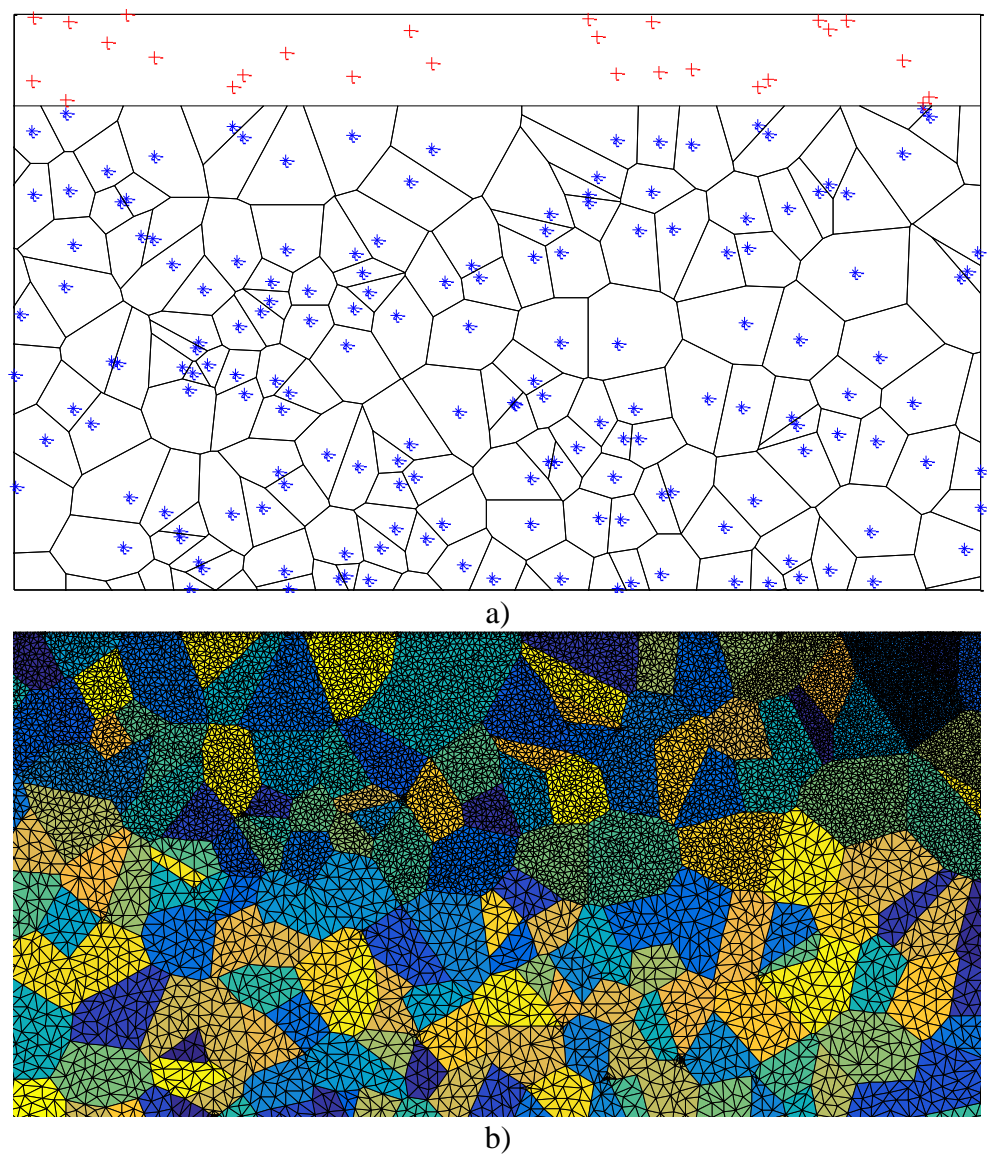
Figure 5.2: Voronoi diagram construction showing a) Voronoi polygons formed from seed points which are shown as blue dots. Red points are the mirrored points used to generate a flat upper surface. b) Finite element filled Voronoi elements showing element size varies within the domain.
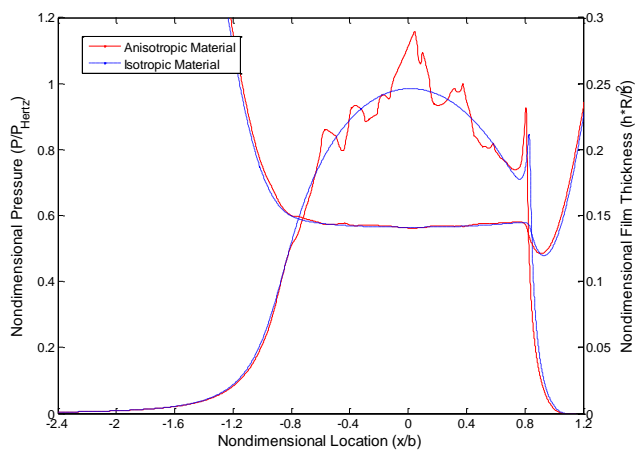
Figure 5.3: Comparison of EHL contact pressures and film thickness profiles for isotropic and anisotropic material models.
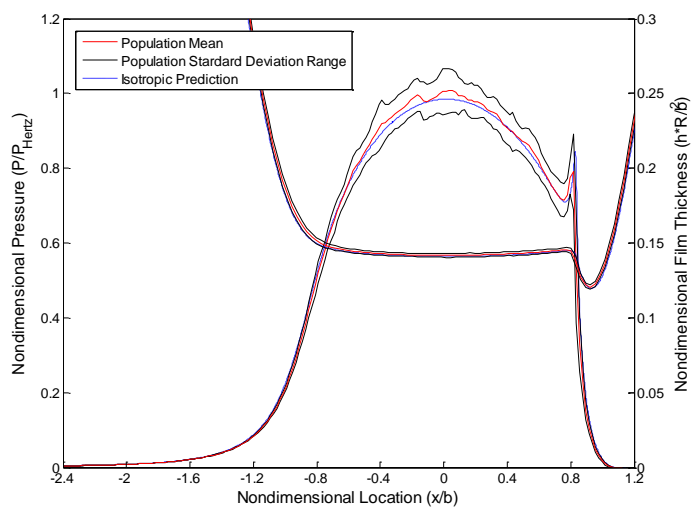
Figure 5.4: EHL contact pressure for mean and standard deviation of anisotropic material model population.
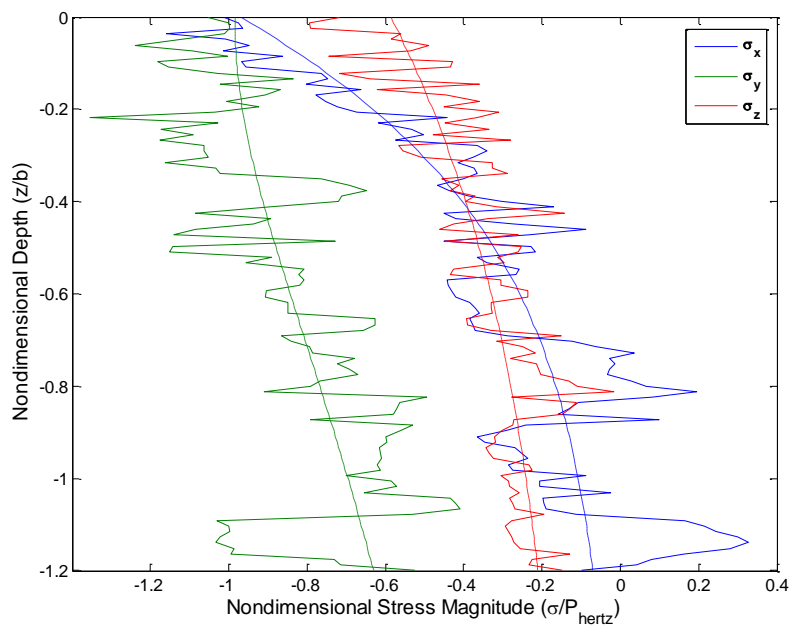
Figure 5.5: Centerline normal stresses, isotropic stresses are dashed and anisotropic stresses are solid lines.
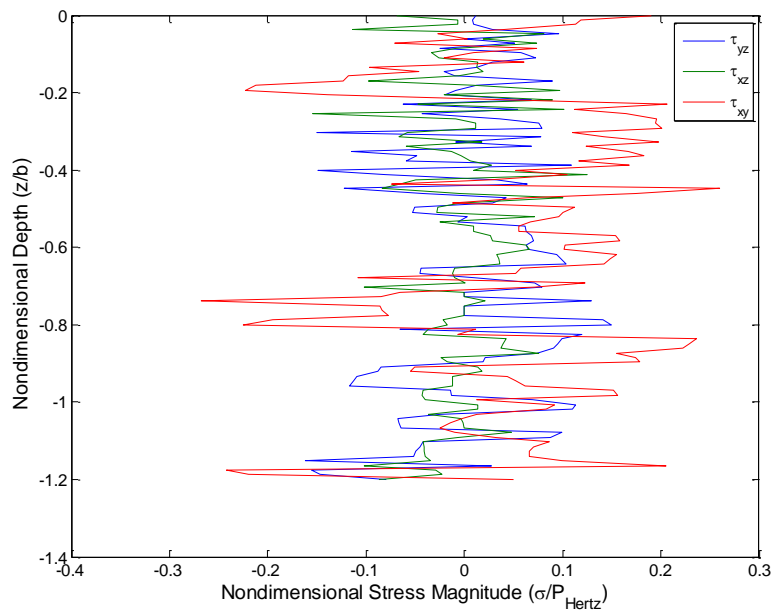
Figure 5.6: Centerline shear stresses observed for an anisotropic material definition.
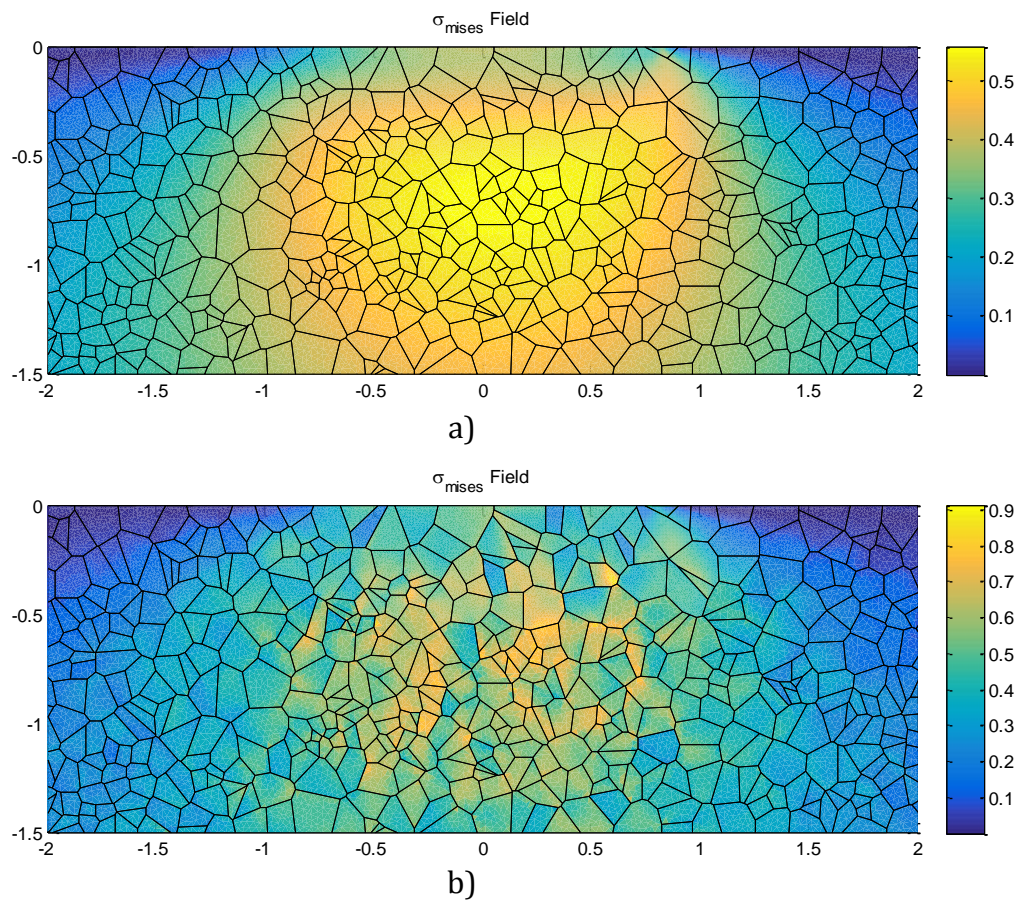
Figure 5.7: Von Mises equivalent stress observed in a) isotropic material model and b) anisotropic material model.
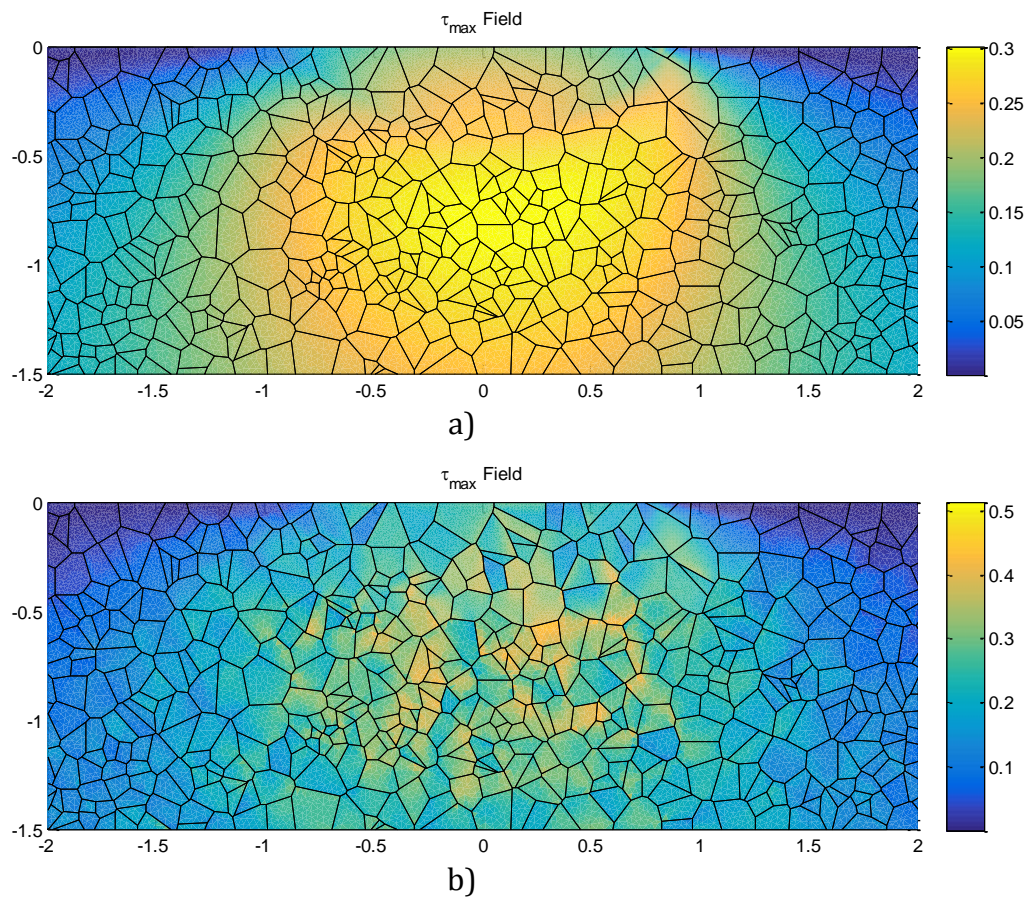
Figure 5.8: Comparison of Maximum Shear Stress Magnitudes for a) isotropic material model and b) anisotropic material model.
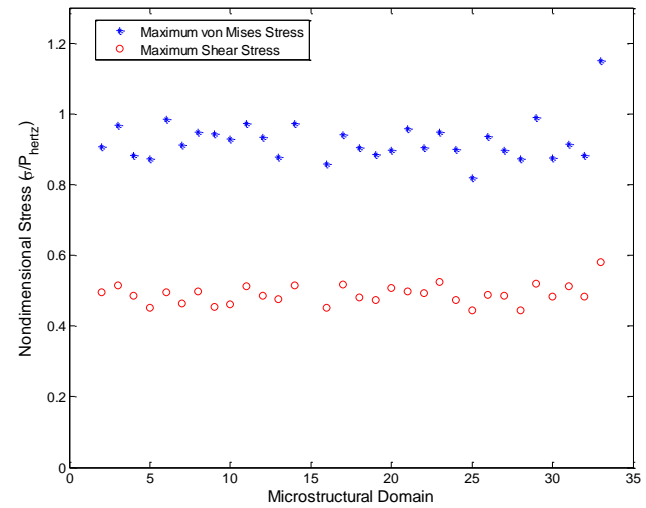
Figure 5.9: Maximum stress magnitude plotted for each microstructure domain. The von Mises and maximum shear stress criterion are shown illustrating the scatter observed in different microstructural domains.
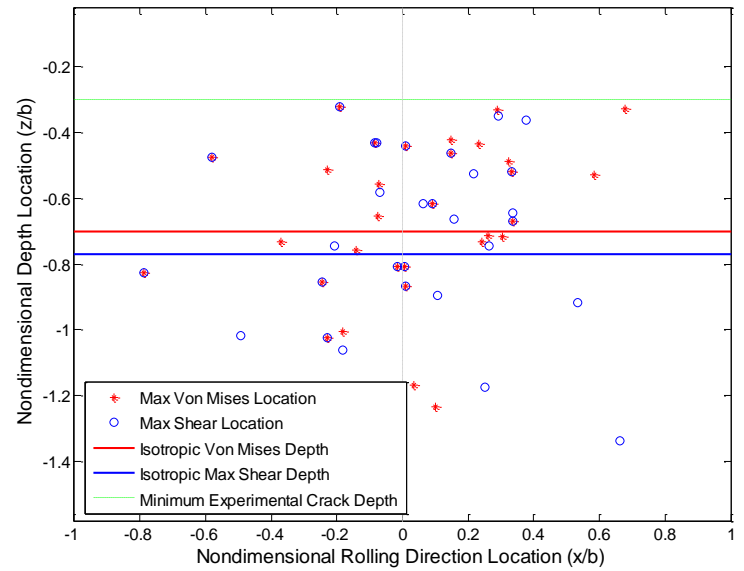
Figure 5.10: Maximum stress location distribution for 33 microstructure domains.
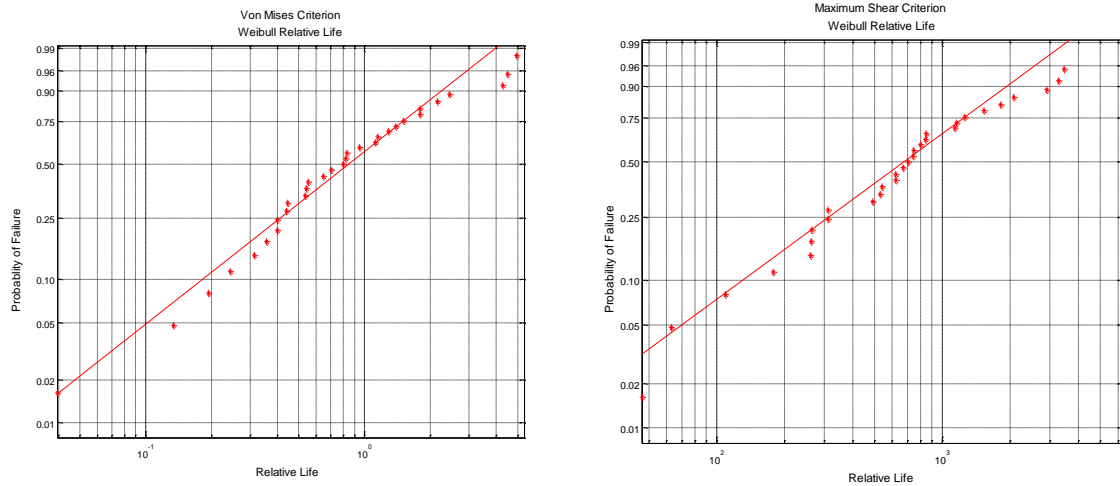
Figure 5.11: Weibull life distribution using a) von Mises stress criterion b)
maximum shear stress criterion.

6. SUMMARY AND FUTURE WORK

6.1   Summary

Chapter 1 introduced the phenomena of rolling contact fatigue. Some of the key concepts that differentiate rolling contact fatigue from classic fatigue were discussed and the difference between surface initiated and subsurface initiate fatigue was described. One of the key ideas proposed is the concept that rolling contact fatigue is a microstructurally sensitive phenomenon. The concept of modeling microstructural variations to capture the apparent randomness in rolling contact fatigue failures was introduced.

In chapter 2 a model was developed to study how refurbishing can extend the useful life of bearings. Using damage mechanics the model predicts the material degradation due to rolling contact passes in a simulated microstructure. The simulated microstructure is created using a Voronoi tessellation which produces are random microstructure similar to what is observed in bearing steels. In order to understand refurbished bearing lives the model divides the lives into two sections. First the original microstructure domain has a load passed over to simulate the original passes on the bearing; these are the passes that occur prior to bearing refurbishment. Once the initial passes are completed refurbishing can be simulated by removing a layer of the microstructural domain to create a new bearing surface which retains any previously damage material from the original simulation. The effect of the amount of material removed (0.125, 0.25, 0.5 and 0.75b) was a variable of interested in this study. To determine an estimate of the life of the refurbished microstructures the refurbished bearing model was again subjected to load passes until the critical damage reached the surface simulating rolling contact fatigue failure.

Results indicate increased depths of refurbishing add to the bearing life up to 0.75 of the half contact width. At 0.75b refurbishing depths the refurbished bearing life is nearly identical to the life predicted for pristine bearing microstructures suggesting fatigue damage is isolated to the region of material between bearing surface and 0.75b. The number of loading cycles prior to refurbishing is also an important factor in the life of

refurbished bearings. Comparing the life estimates of refurbished bearings with prior load passes of 50% vs. 90% of the L_{10} life indicated that refurbishing earlier in the bearing life will increase the life observed post-refurbishing. An alternative model based on experimental data, modified from the Lundberg-Palmgren bearing model, has been proposed for predicting refurbished bearings lives the current model compares well with the alternative model.

Where chapter 2 focused primarily on an application of a previously proposed model to a specific industrial problem, chapter 3 focusses on expanding the rolling contact fatigue model to more accurately account for material variation. A model is developed that explicitly accounts for the effects of grain topology and crystal orientation of a sample microstructure. The topological microstructure is simulated using Voronoi elements representing the material grains wherein individual grains are assigned a random crystallographic orientation and the appropriate cubic stiffness matrix. A Hertzian stress was passed across the domain to simulate rolling contact similar to the approach proposed in chapter 2. Using Lundberg-Palmgren rolling contact fatigue theory and the maximum shear stress reversal as the critical fatigue stress, a relative fatigue life for a given microstructure was calculated. By aggregating a population of simulated microstructures with different grain geometry and crystal orientations, the variation of the shear stress reversal and its location was quantified. Using this data a distribution of the fatigue lives was found and compared to experimental bearing tests.

The anisotropic model provides results previously observed when isotropic material models were assumed. Critical shear stresses where observed on the grain boundaries where mismatch between the crystal orientations create stress concentrations. This supports the idea that rolling contact fatigue initiates at grain boundaries. The critical shear stress depth variation also showed better agreement with the fatigue crack initiation locations observed in experimental literature. When the Lundberg-Palmgren theory was applied to the critical stresses and locations, the predicted dispersion of fatigue lives showed better agreement with experimental results than models that assume an isotropic material definition.

Chapter 4 proposes a coupled model featuring the damage mechanics model proposed in chapter 2 along with a fully coupled elastohydrodynamic model that calculates internal stresses and surface pressures in EHL contacts. By coupling the two models together effects of speed and lubricant properties on pressure and consequently RCF was examined. The DMEHL model was compared to the previous Hertzian pressure damage model similar to that described in chapter 2. Both initiation and final lives were found in increase by 3.7% and 7.1% respectively, when a constant EHL pressure was used instead of a Hertzian pressure. By incorporating the contact pressure dependence on damage accumulation an additional 7.0% increase in the final life was obtained over the fixed EHL pressure profile. From the results it is apparent that the constant Hertzian pressure previously used in RCF life models will under predict the RCF lives of components.

The effect of speed on the fatigue lives and damage accumulation was also investigated using the DMEHL model. Increased speed showed a positive effect on the fatigue lives with a 23% increase observed between the lowest and highest speeds. However, speed showed minimal effect on the size or shape of the fatigue damage. The value of critical damage was evaluated to determine the effect of this value on the coupled DMEHL fatigue lives. Pressure profiles were significantly affected by the value of critical damage. With the critical damage value below 0.5, accumulated damage showed a negligible effect on the pressure profiles throughout the simulation while higher critical damage values showed pressure profiles were highly dependent on the damage accumulation. Therefore the critical damage level is a critical factor for a given material when using the DMEHL model.

Chapter 5 describes a model which combines the conditions proposed in chapter 3 and chapter 4. An approach is proposed to determine the contact pressure, film thickness and subsurface stresses in a polycrystalline anisotropic aggregate material operating under elastohydrodynamic lubrication (EHL). Similar to chapter 4 the approach is based on a fully coupled finite element EHL model which uses a 1D finite elements to solve the Reynolds equation and 2D finite elements to resolve the deformations for a line contact EHL problem. The polycrystalline material is simulated using a Voronoi polygon discretization with each Voronoi polygon receiving a unique crystallographic orientation

similar to that proposed in chapter 3 with the identical cubic crystal stiffness matrix. Results from the FE Voronoi EHL model show that the contact pressures vary due to crystallographic orientation and stress concentrations occur at the polycrystalline grain boundaries. EHL film thickness profiles were not significantly affected by the addition of crystal anisotropy effects to the microstructural model. However, relative life predictions obtained from the model with the anisotropic stress profiles showed that significant life scatter is generated by the addition of crystal anisotropy into the microstructural model. Similar to what was observed with the anisotropic model proposed in chapter 3, the results obtained from the FE Voronoi EHL model show much closer agreement to experimental results than models that assume isotropic material models.

6.2   Future Work

The work presented in this thesis demonstrates models which allow the explicit calculation of factors that are generally ignored when modeling rolling contact fatigue. These factors such as crystal anisotropy and elastohydrodynamic lubrication have been shown to significantly affect the fatigue lives calculated from current RCF models. While the proposed models introduce some new approaches to RCF modeling, there are still many factors that are not addressed which can affect the fatigue lives of these contacts. A few of the extensions that would be useful to better understand rolling contact fatigue are discussed below.

6.2.1   Microstructural Model Improvements

The anisotropic material model presented in chapters 3 and 5 is an advancement in the modeling of microstructural models over isotropic material model assumptions. However, the polycrystalline anisotropy is far from the complete definition of steel microstructures. One effect that would help to develop a more realistic model would be to incorporate crystal plasticity into the material model. This addition would assist in modeling the realistic stress values at the grain boundaries; in the current model stress rises at the grain boundaries and is theoretically unbounded. This creates significant modeling challenges; finite element discretizations must be carefully chosen as

discretization size will affect the observed stress concentrations. By introducing crystal plasticity, the high stresses along the grain boundaries will yield effectively bounding the stresses.

A second assumption of the model that should be addressed in the future developments is the addition of a three dimensional aspect to the microstructural definition. While the two dimensional pressure distribution is a very accurate assumption due to the geometry of rolling contacts, microstructural effects are not completely captured by a two dimensional model. Work by Zeghadi et al. [96] has investigated the differences between two dimensional and three dimensional anisotropy models and shown that more scatter can be observed when all three dimensions are used in the microstructural model. The addition of a three dimensional material microstructure would be a significant advancement for future modeling of anisotropic rolling contact fatigue problems.

Finally, in the initial proposal of the polycrystalline material microstructure presented in chapter 3, a single material phase was considered; however, in reality bearing steels are an agglomeration of multiple material phases including martensite, austenite, and ferrite among others. Future developments of this microstructural model that include these different material phases as well as the various shapes and sizes of those phases would create a more realistic material model capable of differentiating between the microstructural compositions of different bearing steels.

6.2.2 Time Dependence

While the thesis models consider steady state lubrication behavior, whenever inhomogeneities are introduced into the domain there can be significant time dependent effect to the Reynolds equation. This is caused by stiffness changes as the contact passes across the domain. As the two contacting bodies roll past one another the material stiffness will change due to anisotropic effects. This causes the film thickness to never reach a steady state condition like that observed in the isotropic EHL solution. The time dependent Reynolds equation modified from Eq 4.7 is

$$\frac{\partial}{\partial X}\left(\epsilon \frac{\partial P}{\partial X}\right) - \frac{\partial(\bar{\rho}H)}{\partial X} - \frac{\partial(\bar{\rho}H)}{\partial T} - \xi \min(P, 0) = 0 \tag{6.1}$$

where T is the non-dimensional time. Reformulating the equation into the Galerkin weak form, and expanding the time derivative using a first order Newton approximation, the equation can be written as

$$\int_{\Omega_c} -\epsilon \frac{\partial P}{\partial X} \cdot \frac{\partial W_P}{\partial X} d\Omega + \int_{\Omega_c} \bar{\rho} H \frac{\partial W_P}{\partial X} + \int_{\Omega_c} \frac{\bar{\rho}H - \bar{\rho}^{i-1}H^{i-1}}{\Delta T} -$$
$$\int_{\Omega_c} \xi \cdot \min(P, 0) \, W_P d\Omega = 0 \tag{6.2}$$

where $\bar{\rho}^{i-1}$ and H^{i-1} are the nondimensional density and film thickness from the previous iteration, and ΔT is the nondimensional time step between the two iterations. By linearizing the above equation the Newton-Raphson form of the fully coupled system becomes:

$$\begin{bmatrix} J_{11} + \frac{H}{\Delta T}\frac{\partial \rho}{\partial P} & J_{12} + \frac{\bar{\rho}}{\Delta T}\frac{\partial H}{\partial U} & J_{13} + \frac{\bar{\rho}}{\Delta T}\frac{\partial H}{\partial H_0} \\ J_{21} & J_{22} & 0 \\ J_{31} & 0 & 0 \end{bmatrix} \begin{Bmatrix} \delta P \\ \delta U \\ \delta H_0 \end{Bmatrix} = \begin{bmatrix} -R - \left(\frac{\bar{\rho}H}{\Delta T} - \frac{\bar{\rho}^{i-1}H^{i-1}}{\Delta T}\right) \\ -J_{21}P - J_{22}U \\ \frac{\pi}{2} - J_{31}P \end{bmatrix} \tag{6.3}$$

By implementing these changes, the time dependent effects can be calculated in the system. The method is currently being tested to verify the time dependent effects by comparing to the research published by Osborn [97].

6.2.3 Surface Crack Growth

While this manuscript focuses primarily on the phenomena of subsurface initiated rolling contact fatigue, a secondary failure mode exists, where rolling contact fatigue initiates on the surface of a component. In surface initiated rolling contact fatigue the initiation location is significantly easier to find and understand since initiating is caused by increased surface traction at scratches or blemishes in the surface; however, the propagation of surface initiated cracks are complex due to the interaction of lubricant with the crack faces. As the crack begins to grow a gap can form which allows lubricant between the two crack faces. The lubricant has been shown to operate on the crack in three distinct modes as described by Olver [98]. The first mode is to reduce the friction between the crack faces increasing the shear on the crack faces and generating a mode II crack growth mechanism. Secondly, in an opened surface crack, pressure generated in the lubricant film by the contact will apply pressure to the sides of the crack stressing the opening and generating a mode I crack growth mechanism. The final method is caused

when the crack closes with fluid still entrapped between the crack faces. In this mechanism, the forces generated in the body are transferred through the entrapped fluid generating a mode II crack growth mechanism.

The proposed EHL model presented in chapter 4 is particularly suited to understanding the effect of the pressure generated on the crack faces as the load is rolled over the surface. Because contact pressures and subsurface stresses are calculated directly, the effects of crack depth and width can be studied directly as well as the topology evolution of the crack faces as the contact rolls over the cracked surface. Most research model assume a Hertzian pressure profile for the contact pressure profiles; however, as demonstrated in chapter 4, this assumption creates significant error when the compliance of the domain changes due to fatigue damage. Unlike a Hertzian pressure assumption the model proposed can change the compliance behavior to match a given geometry and crack profile allowing more accurate predictions of the stress intensity factors generated from over rolling contacts.

Any analytical modeling should be validated using experimental evidence and recent work by Vallone and Guagliano [99] have proposed an experimental set up using photo-elastic materials that could be used to validate analytically models of subsurface initiated fatigue stress profiles. The combination of the proposed EHL model and a photo-elastic experimental setup could be instrumental in understanding the propagation mechanisms of surface initiated rolling contact fatigue cracks.

REFERENCES

[1] P. E. Bold, M. W. Brown, and R. J. Allen, "Shear mode crack growth and rolling contact fatigue," *Wear*, vol. 144, no. 1–2, pp. 307–317, Apr. 1991.

[2] J. Goodman, "Roller and Ball Bearings," in *Institution of Civil Engineers*, 1912.

[3] A. Palmgren, "The Service Life of Ball Bearings," *Zeitschrift des Vereines Dtsch. Ingenieure*, vol. 68, no. 14, pp. 339–341, 1924.

[4] F. Sadeghi, B. Jalalahmadi, T. S. Slack, N. Raje, and N. K. Arakere, "A Review of Rolling Contact Fatigue," *J. Tribol.*, vol. 131, no. 4, p. 41403, 2009.

[5] G. Lundberg and A. Palmgren, "Dynamic Capacity of Rolling Bearings," *Acta Polytech. Mech. Eng. Ser.*, vol. 1, no. 3, pp. 1–52, 1947.

[6] ISO, "Rolling Bearing - Dynamic Load Ratings and Rating LIfe." ISO, Geneva, Switzerland, 1989.

[7] E. Ioannides and T. A. Harris, "A New Fatigue Life Model for Rolling Bearings," *J. Tribol.*, vol. 107, pp. 367–377, 1985.

[8] E. V. Zaretsky, "Design for Life, Plan for Death," *Mach. Des.*, vol. 66, no. 15, pp. 55–59.

[9] L. M. Keer and M. D. Bryant, "A Pitting Model for Rolling Contact Fatigue," vol. 105, no. April, pp. 198–205, 1983.

[10] M. Dallago, M. Benedetti, S. Ancellotti, and V. Fontanari, "The role of lubricating fluid pressurization and entrapment on the path of inclined edge cracks originated under rolling–sliding contact fatigue: Numerical analyses vs. experimental evidences," *Int. J. Fatigue*, Feb. 2016.

[11] W. Cheng, H. S. Cheng, T. Mura, and L. M. Keer, "Micromechanics Modeling of Crack Initiation Under Contact Fatigue," *J. Tribol.*, vol. 116, no. 3, 1994.

[12] A. Vincent, G. Lormand, P. Lamagnere, L. Gosset, D. Girodin, and R. F. I, "From Whilte Etching Areas Formed Around Inclusions to Crack Nucleation in Bearing Steels Under Rolling Contact Fatigue," in *Bearing Steels: Into the 21st Century*, ASTM STP 1., J. Hoo and W. B. Green, Eds. American Society for Testing and Materials, 1998, pp. 109–123.

[13] R. S. Zhou, H. S. Cheng, and T. Mura, "Micropitting in Rolling and Sliding Contact Under Mixed Lubrication," *J. Tribol.*, vol. 111, no. October, pp. 605–613, 1989.

[14] G. Lormand, A. Vincent, G. Baudry, D. Girodin, and G. Dudragne, "From Cleanliness to Rolling Fatigue Life of Bearings - A New Approach," in *Bearing Steels: Into the 21st Century*, ASTM STP 1., J. Hoo and W. Green, Eds. American Society for Testing and Materials, 1998, pp. 55–69.

[15] N. Raje, F. Sadeghi, R. G. Rateick, and M. R. Hoeprich, "A Numerical Model for Life Scatter in Rolling Element Bearings," *J. Tribol.*, vol. 130, pp. 1–10, 2008.

[16] N. Raje and F. Sadeghi, "Statistical numerical modelling of sub-surface initiated spalling in bearing contacts," *Proc. Inst. Mech. Eng. Part J J. Eng. Tribol.*, vol. 223, no. 6, pp. 849–858, Sep. 2009.

[17] B. Jalalahmadi and F. Sadeghi, "A Voronoi Finite Element Study of Fatigue Life Scatter in Rolling Contacts," *J. Tribol.*, vol. 131, no. 2, p. 22203, 2009.

[18] B. Jalalahmadi, F. Sadeghi, and V. Bakolas, "Material Inclusion Factors for Lundberg-Palmgren–Based RCF Life Equations," *Tribol. Trans.*, vol. 54, no. 3, pp. 457–469, Mar. 2011.

[19] A. Warhadpande, F. Sadeghi, M. N. Kotzalas, and G. Doll, "Effects of plasticity on subsurface initiated spalling in rolling contact fatigue," *Int. J. Fatigue*, vol. 36, no. 1, pp. 80–95, Mar. 2012.

[20] J. A. R. Bomidi and F. Sadeghi, "Three-Dimensional Finite Element Elastic–Plastic Model for Subsurface Initiated Spalling in Rolling Contacts," *J. Tribol.*, vol. 136, no. 1, p. 11402, Nov. 2013.

[21] N. Weinzapfel, F. Sadeghi, V. Bakolas, and A. Liebel, "A 3D Finite Element Study of Fatigue Life Dispersion in Rolling Line Contacts," *J. Tribol.*, vol. 133, no. 4, p. 42202, 2011.

[22] H. Sengstschmid, H. Kottritsch, and K. Wagner, "The Benefits of Remanufacturing Rolling Bearings," *Evolution - technology magazine from SKF*, SKF, pp. 21–26, 2012.

[23] J. J. Coy, E. V. Zaretsky, and G. R. Cowgill, "Life Analysis of Restored and Refurbished Bearings," *NASA Lewis Res. Cent.*, p. NASA TN D-8486, 1977.

[24] J. Alexander, "Bearing Repair Provides Valuable Alternative to Bearing Replacement for Heavy Industries," Canton, OH, 2011.

[25] R. E. Rush, "Bearing Repair and Reconditioning," *Lubrication Engineering*, pp. 10–14, 1991.

[26] E. V Zaretsky and E. V Branzai, "Model Specification for Rework of Aircraft Engine , Power Transmission , and Accessory / Auxiliary Ball and Roller Bearings," no. March, 2007.

[27] "Bearing Repair Services Offer a Cost-Effective Alternative to Expensive Replacement," *World Mining Equipment*, pp. 48–50, 2009.

[28] J. S. Cunningham, Jr. and M. A. Morgan, "Review of Aircraft Bearing Rejection Criteria and Causes," *Lubr. Eng.*, vol. 34, no. 2, pp. 435–441, 1979.

[29] M. N. Kotzalas and M. R. Eckels, "Repair as an Option to Extend Bearing Life and Performance," *SAE Tech. Pap.*, no. No. 2007-01-4234, 2007.

[30] E. V. Zaretsky and E. V. Branzai, "Effect of Rolling Bearing Refurbishment and Restoration on Bearing Life and Reliability," *Tribol. Trans.*, vol. 48, no. 1, pp. 32–44, Jan. 2005.

[31] J. A. R. Bomidi, N. Weinzapfel, F. Sadeghi, A. Liebel, and J. Weber, "An Improved Approach for 3D Rolling Contact Fatigue Simulations with Microstructure Topology," *Tribol. Trans.*, vol. 56, no. 3, pp. 385–399, May 2013.

[32] J. A. R. Bomidi *et al.*, "Experimental and Numerical Investigation of Torsion Fatigue of Bearing Steel," *J. Tribol.*, vol. 135, no. 3, p. 31103, Apr. 2013.

[33] T. Slack and F. Sadeghi, "Explicit finite element modeling of subsurface initiated spalling in rolling contacts," *Tribol. Int.*, vol. 43, no. 9, pp. 1693–1702, Sep. 2010.

[34] J. Lemaitre, *A Course on Damage Mechanics*. Berlin: Springer-Verlag, 1992.

[35] J. L. Chaboche, "Continuum Damage Mechanics : Part I — General Concepts," *J. Appl. Mech.*, 1988.

[36] A. Beheshti and M. M. Khonsari, "A Thermodynamic Approach for Prediction of Wear Coefficient Under Unlubricated Sliding Condition," *Tribol. Lett.*, vol. 38, no. 3, pp. 347–354, May 2010.

[37] V. V. Bolotin and I. L. Belousov, "Early fatigue crack growth as the damage accumulation process," *Probabilistic Eng. Mech.*, vol. 16, no. 4, pp. 279–287, Oct. 2001.

[38] V. V. Bolotin, *Mechanics of Fatigue*. Boca Raton: CRC Press, 1999.

[39] T. A. Harris and W. K. Yu, "Lundberg-Palmgren Fatigue Theory : Considerations of Failure Stress and Stressed Volume," *J. Tribol.*, vol. 121, no. 98, pp. 85–89, 1999.

[40] Y. Choi, "A study on the effects of machining-induced residual stress on rolling contact fatigue," *Int. J. Fatigue*, vol. 31, no. 10, pp. 1517–1523, Oct. 2009.

[41] A. Warhadpande, F. Sadeghi, R. D. Evans, and M. N. Kotzalas, "Influence of Plasticity-Induced Residual Stresses on Rolling Contact Fatigue," *Tribol. Trans.*, vol. 55, no. 4, pp. 422–437, Jul. 2012.

[42] X. Leng, Q. Chen, and E. Shao, "Initiation and Propagation of Case Crushing Cracks in Rolling Contact Fatigue," *Wear*, vol. 122, pp. 33–43, 1988.

[43] K. J. Miller, "the Short Crack Problem," *Fatigue Fract. Eng. Mater. Struct.*, vol. 5, no. 3, pp. 223–232, Jul. 1982.

[44] M. Sauzay and T. Jourdan, "Polycrystalline microstructure, cubic elasticity, and nucleation of high-cycle fatigue cracks," *Int. J. Fract.*, vol. 141, no. 3–4, pp. 431–446, Oct. 2006.

[45] A. A. M. Freudenthal and E. J. Gumbel, "On the Statistical Interpretation of Fatigue Tests," vol. 216, no. 1126, pp. 309–332, 1952.

[46] W. Weibull, "A Statistical Theory of the Strength of Materials.," in *Royal Swedish Academy of Engineering*, 1939, pp. 1–45.

[47] ASME Tribology Division Technical Committee, "Life Ratings for Modern Rolling Bearings: A Design Guide for the Application of International Standard ISO 281/2," 2003.

[48] N. Weinzapfel and F. Sadeghi, "Numerical modeling of sub-surface initiated spalling in rolling contacts," *Tribol. Int.*, vol. 59, pp. 210–221, Mar. 2013.

[49] T. Bohlke and A. Bertram, "Isotropic orientation distributions of cubic crystals," *J. Mech. Phys. Solids*, vol. 49, pp. 2459–2470, 2001.

[50]   M. Nygårds, "Number of grains necessary to homogenize elastic materials with cubic symmetry," *Mech. Mater.*, vol. 35, no. 11, pp. 1049–1057, Nov. 2003.

[51]   E. S. Alley and R. W. Neu, "Microstructure-sensitive modeling of rolling contact fatigue," *Int. J. Fatigue*, vol. 32, no. 5, pp. 841–850, May 2010.

[52]   N. Weinzapfel, F. Sadeghi, and V. Bakolas, "An Approach for Modeling Material Grain Structure in Investigations of Hertzian Subsurface Stresses and Rolling Contact Fatigue," *J. Tribol.*, vol. 132, no. 4, p. 41404, 2010.

[53]   S. Weyer and A. Fr, "Automatic finite element meshing of planar Voronoi tessellations," vol. 69, pp. 945–958, 2002.

[54]   R. Brenner, R. a. Lebensohn, and O. Castelnau, "Elastic anisotropy and yield surface estimates of polycrystals," *Int. J. Solids Struct.*, vol. 46, no. 16, pp. 3018–3026, Aug. 2009.

[55]   F. Barbe, L. Decker, D. Jeulin, and G. Cailletaud, "Intergranular and intragranular behavior of polycrystalline aggregates. Part 1: F.E. model," *Int. J. Plast.*, vol. 17, no. 4, pp. 513–536, Jan. 2001.

[56]   F. J. Franklin, a. Gahlot, D. I. Fletcher, J. E. Garnham, and C. Davis, "Three-dimensional modelling of rail steel microstructure and crack growth," *Wear*, vol. 271, no. 1–2, pp. 357–363, May 2011.

[57]   J. R. Shewchuk, "Triangle: Engineering a 2D Quality Mesh Generator and Delaunay Triangulator," in *Applied Computational Geometry: Towards Geometric Engineering*, M. C. L. and D. Manocha, Ed. Springer-Verlag, 1996, pp. 203–222.

[58]   L. Vitos, P. a Korzhavyi, and B. Johansson, "Stainless steel optimization from quantum mechanical calculations.," *Nat. Mater.*, vol. 2, no. 1, pp. 25–8, Jan. 2003.

[59]   J. M. J. Den Toonder, J. a W. Van Dommelen, and F. P. T. Baaijens, "The relation between single crystal elasticity and the effective elastic behaviour of polycrystalline materials: theory, measurement and computation," *Model. Simul. Mater. Sci. Eng.*, vol. 7, no. 6, pp. 909–928, Nov. 1999.

[60]   R. Mullen, R. Ballarini, Y. Yin, and A. H. Heuer, "Monte Carlo simulation of effective elastic constants of polycrystalline thin films," *Acta Mater.*, vol. 45, no. 6, pp. 2247–2255, Jun. 1997.

[61] R. Hearmon, "The elastic constants of anisotropic materials—II," *Adv. Phys.*, no. 19, pp. 323–382, 1956.

[62] Dassault Systemes, "Abaqus 6.9 Documentation." Simulia Corp, Providence, RI, 2010.

[63] T. Slack and F. Sadeghi, "Cohesive zone modeling of intergranular fatigue damage in rolling contacts," *Tribol. Int.*, vol. 44, no. 7–8, pp. 797–804, Jul. 2011.

[64] Q. Chen, E. Shao, D. Zhao, J. Guo, and Z. Fan, "Measurement of the critical size of inclusions initiating contact fatigue cracks and its application in bearing steel," *Wear*, vol. 147, pp. 285–294, 1991.

[65] T. A. Harris and N. M. Kotzalas, *Rolling Bearing Analysis, 5th ed. - Essential Concepts of Bearing Technology*. Boca Raton, FL: CRC Press.

[66] N. R. Paulson, J. a. R. Bomidi, F. Sadeghi, and R. D. Evans, "Effects of crystal elasticity on rolling contact fatigue," *Int. J. Fatigue*, vol. 61, pp. 67–75, Apr. 2014.

[67] P. Pan and B. J. Hamrock, "Simple Formulas for Performance Parameters Used in Elastohydrodynamically Lubricated Line Contacts," vol. 111, no. April, pp. 246–251, 1989.

[68] C. H. Venner and A. A. Lubrecht, "Numerical Simulation of the Overrolling of a Surface Feature in an EHL Line Contact," vol. 113, no. October, 1991.

[69] G. Xu, D. Nickel, F. Sadeghi, and X. Ai, "Thermoelastic Effects in Lubricated Roiling / Sliding Line Contacts," vol. 210, 1991.

[70] W. Habchi, D. Eyheramendy, P. Vergne, and G. Morales-Espejel, "A Full-System Approach of the Elastohydrodynamic Line/Point Contact Problem," *J. Tribol.*, vol. 130, no. 2, p. 21501, 2008.

[71] M. Cerullo, "Application of Dang Van criterion to rolling contact fatigue in wind turbine roller bearings under elastohydrodynamic lubrication conditions," *Proc. Inst. Mech. Eng. Part C J. Mech. Eng. Sci.*, vol. 228, no. 12, pp. 2079–2089, Dec. 2013.

[72] W. Habchi, "A Full-System Finite Element Approach to Elastohydrodynamic Lubrication Problems: Application to Ultra-Low-Viscosity Fluids," 2008.

[73] O. Reynolds, "On the Theory of Lubrication and Its Applications to Mr. Beauchamp Tower's Experiments, Including an Experimental Determination of the Viscosity of Olive Oil," *Proc. R. Soc. London*, vol. 40, pp. 191–203, 1886.

[74] B. D. Dowson and G. R. Higginson, "A Numerical Solution to the Elasto-Hydrodynamic Problem," *J. Mech. Eng. Sci.*, vol. 1, no. 1, 1959.

[75] C. J. A. Roelands, "Correlational Aspects of the Viscoity-Temperature-Pressure Relationship of Lubricating Oils," Technische Hogeschool Delft, 1966.

[76] N. Brooks and T. Hughes, "Streamline Upwind/Petrov-Galerkin Formulations for Convection Dominated Flows with Particular Emphasis on the Incompressible Navier-Stokes Equations," *Comput. Methods Appl. Mech. Eng.*, vol. 32, pp. 199–259, 1982.

[77] H. Styri, "Fatigue Strength of Ball Bearing Races and Heat-Treated 52100 Steel Specimens," *Proceeds-American Soc. Test. Mater.*, vol. 51, 1951.

[78] A. Warhadpande, B. Jalalahmadi, T. Slack, and F. Sadeghi, "A new finite element fatigue modeling approach for life scatter in tensile steel specimens," *Int. J. Fatigue*, vol. 32, no. 4, pp. 685–697, Apr. 2010.

[79] A. A. Walvekar, B. D. Leonard, F. Sadeghi, B. Jalalahmadi, and N. Bolander, "An experimental study and fatigue damage model for fretting fatigue," *Tribol. Int.*, vol. 79, pp. 183–196, Nov. 2014.

[80] P. D. Zavattieri and H. D. Espinosa, "Grain Level Analysis of Crack Initiation and Propagation in Brittle Materials," *Acta Mater.*, vol. 49, pp. 4291–4311, 2001.

[81] O. Ito and F. E. R., "Computer Modelling of Anisotropic Grain Microstructure in Two Dimensions," *Acta Metall. Mater.*, vol. 41, no. 1, pp. 191–198, 1993.

[82] A. Okabe, B. Boots, K. Sugihara, and S. N. Chiu, *Spatial Tessellations*, 2nd ed. Wiley, 2000.

[83] T. Sakai, N. Oguma, and A. Morikawa, "Microscopic and nanoscopic observations of metallurgical structures around inclusions at interior crack initiation site for a bearing steel in very high-cycle fatigue," *Fatigue Fract. Eng. Mater. Struct.*, vol. 38, no. 11, pp. 1305–1314, 2015.

[84]   K. Tsubota, T. Sato, Y. Kato, K. Hiraoka, and R. Hayashi, "Bearing Steels: Into the 21st Century," in *ASTM STP 1327*, J. J. C. Hoo and G. W. B., Eds. American Society for Testing and Materials, 1998, pp. 202–220.

[85]   J. Guan, L. Wang, C. Zhang, and X. Ma, "Effects of non-metallic inclusions on the crack propagation in bearing steel," *Tribol. Int.*, vol. 106, pp. 123–131, Oct. 2016.

[86]   J.-P. Noyel, F. Ville, P. Jacquet, a. Gravouil, and C. Changenet, "Development of a Granular Cohesive Model for Rolling Contact Fatigue Analysis: Crystal Anisotropy Modeling," *Tribol. Trans.*, vol. 59, no. 3, pp. 469–479, Apr. 2016.

[87]   B. J. Hamrock, S. R. Schmid, and B. O. Jacobson, *Fundamentals of Fluid Film Lubrication*. CRC press, 2004.

[88]   T. S. Slack, N. Raje, F. Sadeghi, G. Doll, and M. R. Hoeprich, "EHL Modeling for Nonhomogeneous Materials: The Effect of Material Inclusions," *J. Tribol.*, vol. 129, no. 2, p. 256, 2007.

[89]   Q. Dong, J. Yang, X. Wang, and L. M. Keer, "Heterogeneous structures with inhomogeneous inclusions under elastohydrodynamic lubrication contact with consideration of surface roughness," *J. Eng. Tribol.*, vol. 230, no. 5, pp. 571–582, 2016.

[90]   Z. Wang, D. Zhu, and Q. Wang, "Elastohydrodynamic Lubrication of Inhomogeneous Materials Using the Equivalent Inclusion Method," *J. Tribol.*, vol. 136, 2013.

[91]   M. Björling, W. Habchi, S. Bair, R. Larsson, and P. Marklund, "Towards the true prediction of EHL friction," *Tribol. Int.*, vol. 66, pp. 19–26, 2013.

[92]   S. R. Wu, "A Penalty Formulation and Numerical Approximation of the Reynolds-Hertz Problem of Elastohydrodynamic Lubrication," *Int. J. Eng. Sci.*, vol. 24, no. 6, pp. 1001–1013, 1986.

[93]   W. Habchi, D. Eyheramendy, P. Vergne, and G. Morales-Espejel, "Stabilized fully-coupled finite elements for elastohydrodynamic lubrication problems," *Adv. Eng. Softw.*, vol. 46, no. 1, pp. 4–18, Apr. 2012.

[94]   N. R. Paulson, F. Sadeghi, and W. Habchi, "A coupled finite element EHL and continuum damage mechanics model for rolling contact fatigue," *Tribol. Int.*, vol. 107, no. November 2016, pp. 173–183, Mar. 2017.

[95] J. R. Shewchuk, "Triangle: Engineering a 2D Quality Mesh Generator and Delaunay Triangulator," in *Applied Computational Geometry: Towards Geometric Engineering*, vol. 1148, M. C. Lin and D. Manocha, Eds. Springer-Verlag, 1996, pp. 203–222.

[96] A. Zeghadi, F. N'guyen, S. Forest, A.-F. Gourgues, and O. Bouaziz, "Ensemble averaging stress–strain fields in polycrystalline aggregates with a constrained surface microstructure – Part 1: anisotropic elastic behaviour," *Philos. Mag.*, vol. 87, no. 8–9, pp. 1401–1424, Mar. 2007.

[97] K. F. Osborn and F. Sadeghi, "Time Dependent Line EHD Lubrication Using the Multigrid / Multilevel Technique," vol. 114, no. January, 1992.

[98] A. V Olver, "The mechanism of rolling contact fatigue : an update," *J. Eng. Tribol.*, vol. 219, pp. 313–330, 2004.

[99] G. Vallone and M. Guagliano, "Photoelastic analysis of surface-cracked elements in presence of Hertzian contact and interposed fluid," *Procedia Eng.*, vol. 10, pp. 3575–3581, 2011.

VITA

Neil Paulson was born in Owatonna, Minnesota on March 26th, 1989. He attended Franklin W. Olin College of Engineering in Acton, Massachusetts where he received in Bachelor of Engineering in Mechanical Engineering in May 2011. Upon completion of his degree he joined the Mechanical Engineering Tribology Laboratory at Purdue University in June 2011. Under the direction of Professor Farshid Sadeghi, he earned his Masters of Science in Mechanical Engineering in 2013 and his Doctorate of Philosophy in May of 2017. Upon complete of his doctoral degree, he joined the Computational Assisted Engineering team at Polaris Industries in Wyoming, Minnesota. His research interests include finite element analysis, rolling contact fatigue, elastohydrodynamic lubrication and component testing.